DISSERTATION

SECONDARY EYEWALL FORMATION AND SHEARED CONVECTION IN MATURE HURRICANES

Submitted by

Wesley D. Terwey

Department of Atmospheric Science

In partial fulfillment of the requirements

for the degree of Doctor of Philosophy

Colorado State University

Fort Collins, Colorado

Fall 2007

COLORADO STATE UNIVERSITY

August 13, 2007

WE HEREBY RECOMMEND THAT THE DISSERTATION PREPARED UNDER OUR SUPERVISION BY WESLEY D. TERWEY ENTITLED SECONDARY EYEWALL FORMATION AND SHEARED CONVECTION IN MATURE HURRICANES BE ACCEPTED AS FULFILLING IN PART REQUIREMENTS FOR THE DEGREE OF DOCTOR OF PHILOSOPHY.

Committee on Graduate Work

Wayne Schubert

Wayne Schubert

David A. Randall

David Randall

Richard Eykholt

Richard E. Eykholt

Adviser, Michael T. Montgomery

Department Head, Richard Johnson

ABSTRACT OF DISSERTATION

SECONDARY EYEWALL FORMATION AND SHEARED CONVECTION IN MATURE HURRICANES

The problem regarding the formation of the secondary eyewall of the major tropical cyclone vortex is set up and examined. As an introductory step, the evolution of and structure of the mean flow changes by free convection in a horizontally and vertically sheared environment is studied using a suite of three-dimensional, high-resolution, full-physics model experiments. It is shown that horizontal shearing may be a strong influence on the lifetimes and structure of convective cells. Additionally, the mean flow changes by these shearing profiles show the importance of shear in determining the projection of the convection onto the mean vortex. Vertical shearing forces an antisymmetry in the mean potential vorticity change, while horizontal shear tends to symmetrize these changes. A combination shear appears to force an antisymmetric structure in the mean potential vorticity change that tilts with height.

After exploring this introductory work, prevailing hypotheses for secondary eyewall formation are examined using datasets from two high-resolution mesoscale numerical model simulations of the long-time evolution of an idealized hurricane vortex in a quiescent tropical environment with constant background rotation. The modeled hurricanes each undergo a secondary eyewall cycle, casting doubt on a number of these hypotheses for secondary eyewall formation due to the idealizations present in the model formulation.

A new hypothesis for secondary eyewall formation is proposed here and shown to be supported by these high-resolution numerical simulations. The hypothesis requires

the existence of a region with moderate horizontal strain deformation and a sufficient low-level radial potential vorticity gradient associated with the primary swirling flow, moist convective potential, and a wind-moisture feedback process at the air-sea interface to form the secondary eyewall. The crux of the formation process is the generation of a finite-amplitude lower-tropospheric cyclonic jet outside the primary eyewall with a jet width on the order of a local effective beta scale determined by the mean low-level radial potential vorticity gradient and the root-mean-square eddy velocity. This jet is generated by the anisotropic upscale cascade and axisymmetrization of convectively generated vorticity and kinetic energy anomalies through horizontal shear turbulence and sheared vortex Rossby waves as well as by the convergence of momentum by the induced low-level radial inflow associated with the increased convection. Possible application to the problem of forecasting secondary eyewall events is briefly considered.

Wesley D. Terwey
Department of Atmospheric Science
Colorado State University
Fort Collins, Colorado 80523
Fall 2007

ACKNOWLEDGEMENTS

This research was supported in part by the National Science Foundation under Grants ATM 0101781, ATM 0349980, ATM 0528816, and ATM 0530884, as well as Colorado State University.

Special thanks go out to my adviser, Dr. Michael T. Montgomery, whose discussions and insight have been invaluable in the formation of this hypothesis. Additional thanks go to my doctoral committee: Dr. David Randall, Dr. Wayne Schubert, and Dr. Richard Eykholt, whose patience and aid has been highly appreciated.

Numerous thanks go out to the members of the Montgomery and Schubert groups for all their help and support through the years, in particular, Michael Bell, Eric Hendricks, Dr. Phil Klotzbach, Kevin Mallen, Kate Musgrave, Dr. John Persing, Dr. Chris Rozoff, and Dr. Dave Schecter. Special thanks to Dr. Mel Nicholls for his aid in the setup and execution of the RAMS model. I would also like to thank Dr. Yongshen Chen and Dr. Peter Yau for helpful discussions, as well as many other knowledgable scientists in this field whom I have had terrific discussions on this topic with in the last three years.

Last, but certainly not least, I would like to thank all my family and friends who have offered support all these years.

CONTENTS

1 Introduction **1**

2 Sheared Convection **9**
2.1 Model Setup 9
2.2 Convection Effects on the Mean State 16

3 Hurricane Model and Basic Evolution **29**
3.1 Hurricane Simulation Specifics 29
3.2 Simulated Hurricane Evolution 31
3.2.1 Genesis Phase 35
3.2.2 Mature Phase 38
3.2.3 Secondary Eyewall Phase 43

4 Theory **53**
4.1 Prior Formation Hypotheses 53
4.2 Quasi Two-Dimensional Turbulence Theory 58
4.3 Hypothesis 60

5 Secondary Eyewall Formation **66**
5.1 Basic Analysis 66
5.2 Isentropic Momentum Budget 75

6 No-Ice Sensitivity Simulation Results **86**
6.1 Basics 86
6.2 Results 91

7 Discussion and Conclusions **96**

8 References **99**

A The RAMS **107**

LIST OF FIGURES

1.1 Three different views of the basic structure of the tropical cyclone. The top frame shows the winds in the hurricane. The middle frame highlights the winds and clouds near and in the eyewall region of the tropical cyclone, showing the inwardly-directed swirling surface flow as well as the upward motions in the eyewall. The bottom frame shows an idealized rainfall map of the hurricane rainbands outside the eyewall. This figure is courtesy of the NASA and the COMET program. 2

1.2 Frame (a) shows the best track sea-surface pressure trace from the National Hurricane Center for Hurricane Ivan (2004). Frame (b) shows a research aircraft radar composite of Ivan with two eyewalls. At this time, the central pressure is about to increase, indicating a temporary, but rapid, decrease in the intensity of the storm correlated with the secondary eyewall cycle. Kingston, Jamaica is approximately 600 km northwest of the storm center at this time. Frame (b) is courtesy of the National Hurricane Center. 5

2.1 Composite vertical profile of dew point (dotted; ^{o}C), temperature (solid; ^{o}C) and hypothetical, undilute, surface-based parcel path temperature (dashed; ^{o}C). 11

2.2 Total cloud condensate ($q_{\text{cond}} \geq 0.5$ g kg^{-1}) for experiments v00h2 (left column), v00h4 (middle column), and v00h6 (right column). Using q_{cond}, precipitation is seen beneath the cloud base. 15

2.3 Mean potential vorticity change from initial values for the no shear (control) case. Time is 1.0 hours (top left), 2.0 hours (top right), 3.0 hours (bottom left), and 4.0 hours (bottom right). Contouring begins with ± 0.025 PVU and doubles with each increasing contour. 17

2.4 Mean potential vorticity change from initial values for the four cases with no horizontal shear. Time is 3.5 hours. Vertical shear values for each plot are 0 m/s (control, top left), 5 m/s (top right), 10 m/s (bottom left), and 20 m/s (bottom right). Contours as in Figure 2.3. 18

2.5 Mean potential vorticity change from initial values for the four cases with no vertical shear. Time is 3.5 hours. Horizontal shear values for each plot are 0×10^{-4} s^{-1} (control, top left), -2×10^{-4} s^{-1} (top right), -4×10^{-4} s^{-1} (bottom left), and -6×10^{-4} s^{-1} (bottom right). Contours as in Figure 2.3. 21

2.6 Mean potential vorticity change from initial values for the four cases with 10 m/s vertical shear. Time is 3.5 hours. Horizontal shear values for each plot are 0 $\times$ 10^{-4} s^{-1} (control, top left), -2 $\times$ 10^{-4} s^{-1} (top right), -4 $\times$ 10^{-4} s^{-1} (bottom left), and -6 $\times$ 10^{-4} s^{-1} (bottom right). Contours as in Figure 2.3. 22
2.7 Potential vorticity for four heights with 10 m/s vertical shear and $v_x = -2 \times 10^{-4}$ s^{-1}. Time is 3.5 hours. 24
2.8 Change in the mean potential temperature after 3.5 hours for four different experiments. Experiments shown are v00h0 (top left), v00h4 (top right), v10h0 (bottom left), and v10h4 (bottom right). Contouring interval is 0.125 K. 26
2.9 Change in the mean meridional wind after 3.5 hours for four different experiments. Experiments shown are v00h0 (top left), v00h4 (top right), v10h0 (bottom left), and v10h4 (bottom right). Contouring interval is 0.125 m s^{-1}. 27

3.1 Representative soundings for the control experiment. Frame (a) depicts the sounding in the environment, while frame (b) depicts the sounding at the center of the MCV. Figure taken from Montgomery et al. (2006). 32
3.2 Evolution of the control simulation. The solid line is lowest pressure observed at the lowest model layer (approximately 150 m). The dotted line is the maximum azimuthal mean tangential velocity in the lowest model layer. The dashed line is the radius of the maximum mean tangential velocity at the lowest model layer in kilometers. 33
3.3 Early time potential vorticity cross-sections. Time, using Hour 0 as the origin, is denoted in the lower-right corner of each panel. 36
3.4 Azimuthal mean tangential wind for the control simulation at Hour -108. . . 37
3.5 Time-radius plot of the lowest level azimuthal mean tangential winds (left) and the mass-weighted, vertically-integrated azimuthal mean PV (right). Time is indexed with Hour 0 being the origin. 38
3.6 Low-level potential vorticity cross-sections between -66 and -57 Hours. 40
3.7 Low-level potential vorticity cross-sections between -48 and -12 Hours. 41
3.8 Azimuthal mean tangential wind (left) and mean relative vorticity (right) for the control simulation at Hour 12. 42
3.9 Vertical velocity (left) and potential vorticity (right) at 2.3 km height for the control simulation at Hour 12. 43
3.10 Composite radar imagery from Hurricane Rita (2005) between 1705 and 1742 UTC on 22 September from the Eldora aircraft radar. In this figure, we see the finer details of the convective elements in the outer core of the hurricane. Airplane icons trace the route of the aircraft during the flight. Figure courtesy of Michael Bell. 44
3.11 Vertical velocity (left) and potential vorticity (right) at 2.3 km height for the control simulation at Hour 15.5. 45

3.12 Vertical velocity (left column) and potential vorticity (right column) at 2.3 km height for the control simulation at Hour 16.5 (top row) and at Hour 18 (bottom row). 46
3.13 Vertical velocity at 2.3 km height for the control simulation at Hours 18 (top left), 19 (top right), 20 (bottom left), and 21 (bottom right). 47
3.14 Vertical velocity at 2.3 km height for the control simulation at Hours 22 (top left), 23 (top right), 24 (bottom left), and 25 (bottom right). 48
3.15 Azimuthal mean radial wind profiles at Hours 12 (left) and 22 (right). 49
3.16 Vertical velocity at 2.3 km height for the control simulation at Hours 27 (top left), 30 (top right), 33 (bottom left), and 36 (bottom right). 50
3.17 Composite radar data from aircraft reconnaisonce into Hurricane Ivan (2004) on 12 September. Two eyewalls are evident. The outer eyewall is elliptical in shape. 52

4.1 Azimuthal mean vertical velocity at Hour 10. 56
4.2 Proposed conceptual model of the nonlinear β-skirt axisymmetrization secondary eyewall formation mechanism. 61

5.1 Calculations of τ_{fil} and effective β in the control simulation. This calculation uses temporally averaged azimuthal mean quantities from Hours 8 to 12. Contour intervals are 10 minutes for τ_{fil} and 12.5×10^{-9} m^{-1} s^{-1} for β. Vorticity-dominated (for τ_{fil}) and negative β regions are shaded. Only the first ten contours of each sign for β are drawn. 67
5.2 Calculation of effective β in the control simulation prior to Hour 0. This calculation uses four-hour temporally averaged azimuthal mean quantities. The calculation from Hours -24 to -20.1 is plotted in the left panel, while the right panel displays the calculated quantity from Hours -12 to -8.1. . 68
5.3 Surface-based CAPE and CIN calculations using azimuthal mean thermodynamic quantities at Hour 10. 69
5.4 Mass-weighted low-level perturbation kinetic energy spectrum for three different times during the secondary eyewall formation period for the control experiment. Units for kinetic energy are m^2 s^{-2}. The integration is for the annulus surrounding the formation region: 60 to 150 km radius and 0 to 4 km height. 71
5.5 Change in the mean tangential wind (shaded, m s^{-1}) from Hour 0, along with the instantaneous mean w'^2 contour of 1 m^2 s^{-2} in thick black from the control experiment. Calculations for Hour 7 (top left), Hour 9 (top right), Hour 11 (bottom left) and Hour 13 (bottom right) show the intensification of a low-level jet. 72
5.6 Mean radial velocity ($\bar{u}$) at Hour 8 (left) and Hour 10 (right) showing the gradual increase in the inflow in the lowest levels outside 120 km radius. . 74
5.7 2-hour integrated tangential momentum budget from model data. Integration takes place over the two-hour interval from Hours 8 to 10. 79
5.8 Azimuthal mean potential temperature ($\bar{\theta}$) at Hour 9. 80

5.9 Partition of the FEP term into momentum and thermal flux mean tangential velocity changes. Contours are 1/2 of the contours in Figure 5.7. 82
5.10 Azimuthal mean sounding at 110 km radius at Hour 11. 84

6.1 Evolution of the no-ice simulation. The solid line is lowest pressure observed at the lowest model layer (approximately 150 m). The dotted line is the maximum azimuthal mean tangential velocity in the lowest model layer. The dashed line is the radius of that maximum tangential velocity in kilometers. 87
6.2 Time-radius plot of the azimuthal mean vertical velocity at 5 km height. . . . 89
6.3 Vertical velocity at 2.2 km height in the no-ice simulation. Times shown are Hours 7.5 (top left), 10.5 (top right), 13.5 (bottom left), and 16.5 (bottom right). During this time, the secondary eyewall forms. Both eyewalls are readily visible at Hour 16.5. 90
6.4 Calculations of τ_{fil} and β for the no-ice simulation. This calculation uses temporally averaged azimuthal mean quantities from Hours 5 to 9. Contours as in Figure 5.1. 92
6.5 Surface-based CAPE and CIN calculations using azimuthal mean quantities at Hour 6. 93
6.6 Change in the mean tangential wind (shaded, m s^{-1}) from Hour 0, along with the instantaneous mean w'^2 contour of 1 m^2 s^{-2} in thick black from the no-ice experiment. Calculations for Hour 6 (top left), Hour 8 (top right), Hour 10 (bottom left) and Hour 12 (bottom right) show the intensification of a low-level jet. 94
6.7 Mean radial velocity ($\bar{u}$) at Hour 8 (left) and Hour 10 (right) showing the gradual increase in the inflow in the lowest levels outside 120 km radius in the no-ice simulation. 95

Chapter 1

INTRODUCTION

The tropical cyclone (also refered to as a hurricane in the Northern Atlantic) is a strong tropical low-pressure storm system with cyclonic winds greater than 33 m s^{-1} and organized convection. The tropical cyclone includes two main circulations: the primary and secondary (Figure 1.1). The cyclonic winds swirling around the main center of the cyclone are refered to as the primary circulation. The majority of the kinetic energy in the tropical cyclone is found in this circulation. The secondary circulation is colloquially referred to as the "in, up, and out" circulation. Winds come into the hurricane in the lowest levels. Once the winds approach the eye, they rise, becoming the eyewall clouds that surround the cloud-free eye. At the top of the troposphere, this air moves outward, generating the distinctive anvil swirl that is seen on satellite pictures. The secondary circulation provides the hurricane the energy it needs to overcome the weakening effects of friction. As the air comes into the eyewall from the low levels, it flows over the warm surface waters of the tropical oceans, gathering water vapor and heat. The ample moisture in this warm air condenses in the eyewall, providing the heat needed to maintain the warm core of the tropical cyclones. This warm core, along with thermal and gradient wind balances, allows the vortex to remain coherent and strong.

Tropical cyclones are categorized by their primary circulation wind speeds. Once the wind speed reaches above 50 m s^{-1}, the cyclone is called "major". The impacts of a landfalling major tropical cyclone can be devastating and far-reaching. In the Atlantic basin, Hurricanes Andrew (1992), Katrina (2005), and Mitch (1998) have all

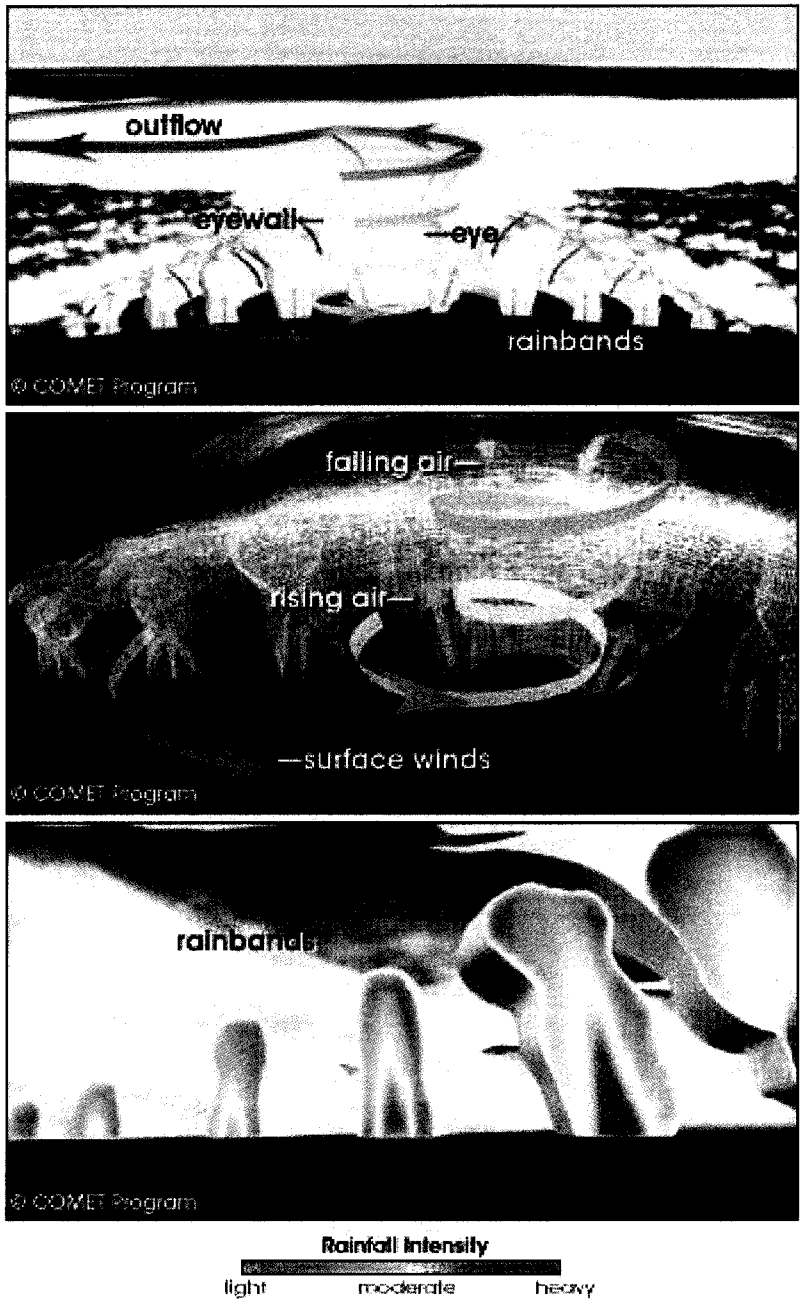

Figure 1.1: Three different views of the basic structure of the tropical cyclone. The top frame shows the winds in the hurricane. The middle frame highlights the winds and clouds near and in the eyewall region of the tropical cyclone, showing the inwardly-directed swirling surface flow as well as the upward motions in the eyewall. The bottom frame shows an idealized rainfall map of the hurricane rainbands outside the eyewall. This figure is courtesy of the NASA and the COMET program.

caused massive damage and loss of life as they made landfall. Each of these examples emphasizes a different aspect of the damage a tropical cyclone can produce. Hurricane Andrew (1992) swept over southern Florida, where its high winds were the primary source of damage to the homes in that region. Katrina (2005) featured a significant storm surge which flooded the city of New Orleans by exposing the weaknesses in the city's levy system. Mitch (1998) produced flooding rains in the mountainous regions of Honduras and Nicaragua as it stalled just north of these countries, leading to widespread and deadly floods and mudslides.

The major tropical cyclone or hurricane is, therefore, a primary focal point for hurricane forecasters. Accurately predicting the intensity and track of these significant weather events is one of the most important duties of the hurricane forecaster. While the National Hurricane Center has shown improved skill in the forecasting of the track of tropical cyclones in the Atlantic and Eastern Pacific basins, their skill in the forecast of the intensity of these storms has not improved nearly as much (National Hurricane Center, 2007).

While the major hurricane's main structure (the primary and secondary circulations) are well understood, there are still significant unanswered questions about some of the other features of the tropical cyclone. As noted in Figure 1.1, most hurricanes have rainbands outside the main eyewall. How these rainbands form, evolve, and modify the tropical cyclone's circulations are active areas of research. Normally, these rainbands do not completley encircle the main eyewall. However, in major hurricanes, it has been observed that occasionally a completely new ring of convection can form outside the main eyewall of the storm. These new rings of convection are referred to as secondary (or concentric) eyewalls.

Secondary eyewalls are perhaps one of the more enigmatic features of fully developed tropical cyclones. Once regarded as an infrequent occurrence during a tropical cyclone's lifecycle, climatologies of this phenomenon using both aircraft reconnaissance radar data

and high-resolution microwave satellite data have shown that approximately 50% of all major tropical cyclones undergo at least one eyewall replacement cycle in their lifetimes (Willoughby, 1990; Hawkins and Helveston, 2004).

Observations of secondary eyewall cycles gathered during the last three decades (e.g. Willoughby et al., 1982; Black and Willoughby, 1992; Willoughby and Black, 1996; Houze et al., 2006 and 2007) and theoretical dynamics (e.g. Shapiro and Willoughby, 1982) have suggested that the effects of the secondary eyewall phenomenon on the intensity of a storm can be significant, particularly in the short-term.

An illustrative example is Hurricane Ivan (2004) in the Atlantic Ocean, as seen in Figure 1.2. Ivan entered the Caribbean Sea on 8 September 2004 as a major hurricane. As Ivan approached the island of Jamaica, a secondary eyewall formed, as seen in aircraft radar data from near Jamaica (Figure 1b). As the secondary eyewall matured, the minimum central pressure (Figure 1a) rose 15 mb in approximately 18 hours. According to aircraft reconnaissance data, the reported wind speed of Ivan also dropped 10 to 15 knots during this time period, a substantial intensity decrease from the maximum of 140 knots prior to the secondary eyewall cycle (not shown). While there was likely some influence on the strength of Ivan's outer circulation by the Jamaican landmass, the inner core region (comprised of the eye and primary eyewall) of the storm was far enough from the island (approximately 200-600 km through the cycle) to support the hypothesis that the secondary eyewall was the dominant influence on the observed short-term intensity fluctuation (cf. Willoughby et al., 1982; Willoughby et al., 1985).

In the past, the primary theoretical focus has been directed at the evolution of the secondary eyewall and its interaction with the primary eyewall (Willoughby et al., 1982; Shapiro and Willoughby, 1982). In these theories, the secondary circulation associated with the secondary eyewall forces a gradual spindown of the strong tangential winds near the primary eyewall by inducing a weakly divergent radial wind field there. Additionally, this circulation forces subsidence in the region surrounding the primary eyewall,

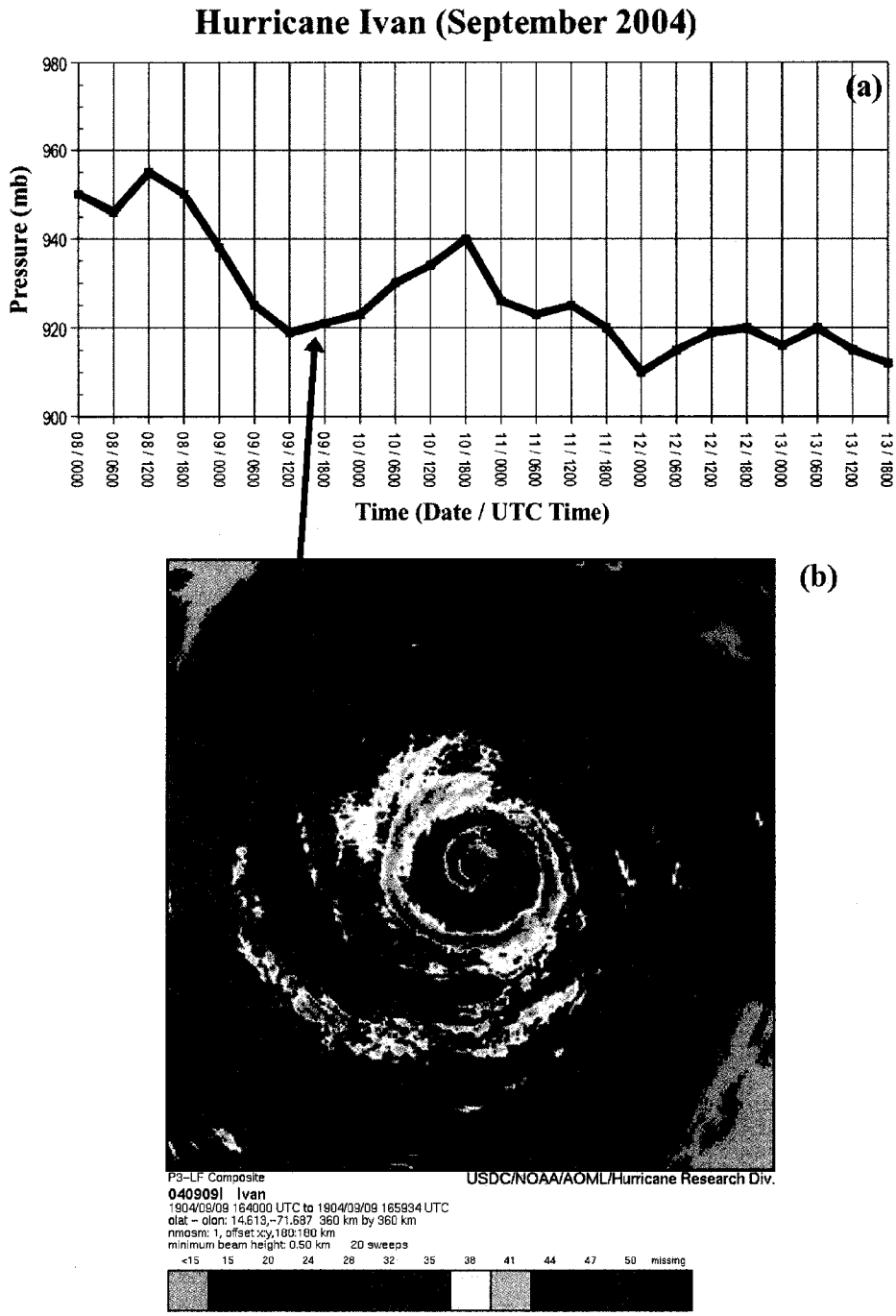

Figure 1.2: Frame (a) shows the best track sea-surface pressure trace from the National Hurricane Center for Hurricane Ivan (2004). Frame (b) shows a research aircraft radar composite of Ivan with two eyewalls. At this time, the central pressure is about to increase, indicating a temporary, but rapid, decrease in the intensity of the storm correlated with the secondary eyewall cycle. Kingston, Jamaica is approximately 600 km northwest of the storm center at this time. Frame (b) is courtesy of the National Hurricane Center.

inhibiting its convection. As these processes temper the winds and convection associated with the original eyewall, the secondary eyewall strengthens and assumes the role of the primary eyewall of the cyclone. The combined changes associated with the strengthening secondary eyewall and the weakening primary eyewall generally decrease the magnitude of the maximum mean tangential winds of the system and increase the minimum surface pressure (e.g. Willoughby et al., 1985). After this occurs, the new eyewall typically contracts, reconsolidating the swirling winds of the storm toward the center.

This eyewall evolution theory has proven qualitatively useful in describing intensity changes in mature hurricanes due to eyewall cycles (e.g. Willoughby et al., 1984; Willoughby and Black, 1996; Houze et al., 2007). One of the challenges still facing hurricane forecasters, however, is that a secondary eyewall cycle may happen multiple times through the lifetime of long-lived mature tropical cyclones, or it may never occur. The mechanisms that determine whether or not a secondary eyewall cycle occurs in a given hurricane are still unknown. This highlights the primary weakness of the cycle theory: the processes that cause the formation of the secondary eyewall in the first place.

During the past three decades, a number of hypotheses have been proposed to describe the formation of the secondary eyewall. Willoughby et al. (1982), extending the tropical squall line work of Zipser (1977), suggested that downdrafts from the primary eyewall's convection may force a ring of updrafts outside of it. Hawkins (1983) proposed that topographic effects might form a secondary eyewall. Other results (Molinari and Skubis, 1985; Molinari and Vallaro, 1989) have suggested that large-scale environmental forcings, such as low-level wind surges or upper-level angular momentum fluxes from intruding potential vorticity anomalies, may be causes of general eyewall formation. Willoughby (1979) hypothesized the existence of an internal resonance between the local inertia period and asymmetric friction due to the storm's motion could form a new eyewall. Additionally, ice microphysics has been suggested as an enhancement mechanism in secondary eyewall formation (Willoughby et al., 1984).

More recently, simple numerical modeling experiments have been used to investigate the secondary eyewall formation process. Using axisymmetric hurricane models developed by Emanuel (1989, 1995) and Rotunno and Emanuel (1987), Nong and Emanuel (2003) carried out a number of idealized simulations and concluded that sustained eddy angular momentum fluxes arising from interactions between a mature storm and its synoptic environment can form secondary eyewall features, provided a surface-wind/water vapor feedback operates in the same region. This wind-induced surface heat exchange process is called WISHE (Yano and Emanuel, 1991). From the perspective of barotropic non-divergent vorticity dynamics, Kuo et al. (2004, 2007) suggested that secondary eyewall formation arises essentially from the axisymmetrization of cyclonic vorticity perturbations around a strong primary vortex core.

It has not been until very recently, however, that three-dimensional full-physics numerical models have shown the ability to simulate a secondary eyewall cycle. In the current work we examine a pair of idealized long-time hurricane simulations using a full-physics three-dimensional mesoscale model. These simulations are shown to produce realistic tropical cyclones, including a complete secondary eyewall cycle, under both full (ice and water) and water-only moist physical representations. Using the model datasets generated by the simulations, we analyze the basic physics of secondary eyewall initiation, testing and drawing ideas from previous hypotheses for this complex process. Prior formation hypotheses are summarized, and most are rejected as adequate exexplanations for our particular cases, generally because of the specific idealizations assumed by the model setup. A new hypothesis along with supporting evidence is presented here for an intrinsic secondary eyewall formation mechanism that involves a turbulent, horizontally anisotropic, upscale energy cascade of convectively generated small-scale eddies in an anticyclonic shear zone outside the main core of the hurricane. While the axisymmetrization ideas of numerous previous works (e.g. Melander et al., 1987; Montgomery and Kallenbach, 1997; Kuo et al., 2004; Kuo et al., 2007) lay a fundamental foundation

for the problem, our hypothesis extends these ideas to account for the sustained and stochastic potential vorticity and cumulus convection interactions that occur within the hurricane.

In Chapter 2, we examine the effects of both horizontal and vertical shears on numerically-modelled free convective cells, focusing on the changes these cells have on their surrounding mean flow. Chapter 3 describes the hurricane model setup, including the initial conditions and the simplifications used, and also summarizes the evolution of the control hurricane simulation that spontaneously generates a secondary eyewall. Previous secondary eyewall formation hypotheses are then assessed in Chapter 4 with regard to the control simulation, and a new formation paradigm is proposed. Chapter 5 focuses on the pertinent dynamical diagnostics and theories used to offer supporting evidence for the hypothesized formation mechanism. A summary of the no-ice (water-only) microphysical species sensitivity experiment is presented in Chapter 6. This "reduced physics" experiment also produces a secondary eyewall cycle, and we briefly show the similarity of the results between these two experiments. Lastly, in Chapter 7, we summarize our findings and discuss future planned work for these numerical experiments as well as potential future numerical experiments.

Chapter 2

SHEARED CONVECTION

Since we anticipate that the secondary eyewall formation process and convection in the outer core of the hurricane vortex are non-trivially related and interconnected, we look for studies of convection in hurricane-like environments. It is well known that convection is modulated and organized by vertical shear (e.g. Wilhelmson and Wicker, 2001; Rotunno and Weisman, 2004). However, the shear in the mature hurricane outer core environment generally has both vertical and horizontal components (e.g. Rozoff et al., 2006; Mallen et al., 2005).

Currently, it is unknown what effects horizontal shearing may have on convection. To better understand the morphology of convection in this unique environment, we perform a simple, idealistic modeling experiment. In this chapter, we will focus on the fundamental changes that differing combinations and varieties of shears may have on the projection of the convection onto the azimuthal mean hurricane vortex. Further work on this project including a detailed analysis of the dynamics of sheared convection will be completed in due course.

2.1 Model Setup

For this idealized convection study, we will use the Regional Atmospheric Modeling System (RAMS) version 4.3 (Cotton et al. 2003). Unless noted below, some of the details of these RAMS simulations are described in Appendix A.

In these experiments, one grid is used to avoid the errors inherent to nesting. The horizontal grid measures 125 km per side with 500 m grid spacing. Since the domain

is small, the Coriolis parameter is fixed (f-plane approximation). In the vertical, a stretched Cartesian coordinate is employed over a depth of 25 km. A grid spacing of 160 m is used beginning at the surface, and the vertical grid spacing is progressively stretched by a factor of 1.065 between overlying gridpoints until a vertical grid spacing of 500 m is achieved and used thereafter. The time step is 2 s. All simulations use the seven-species, one-moment microphysics scheme as described in Appendix A (Walko et al., 1995). For maximum simplicity, we neglect radiation and assume a free slip surface boundary condition. A Rayleigh friction layer is used for the top five levels of the model domain to limit reflection of gravity waves off the rigid model lid. Lateral boundaries use the Klemp-Wilhelmson condition, which specifies the normal velocity component at the lateral boundary. Each simulation in this chapter is run out for 4 hours of simulation time.

The initial thermodynamic profile is composited from four dropsondes and one rawindsode obtained outside the core of the Category 5 Hurricane Isabel (2003) on 13 September. The dropsonde data are relegated to altitudes below 700 hPa and distances between 150 and 250 km from the storm center. To complete the sounding, a proximity sounding from San Juan, Puerto Rico from approximately the same time as the dropsondes is added to the dropsonde composite.

The resulting vertical profile of temperature, dew point, and a hypothetical, undilute surface-based parcel path temperature is provided in Figure 2.1. To measure the amount of convective instability, we examine the aggregate measure of the amount of energy that moist convection can utilize, known as the convective available potential energy (e.g. Emanuel, 1994). In this sounding, the surface-based convective available potential energy (CAPE) is 2067 J kg^{-1} while the convective inhibition (CIN), or convective barrier, is only 1 J kg^{-1}. Dry, unstable air aloft and nearly moist-neutral low-levels characterize the composite sounding. There is some debate to be made as to the representativeness

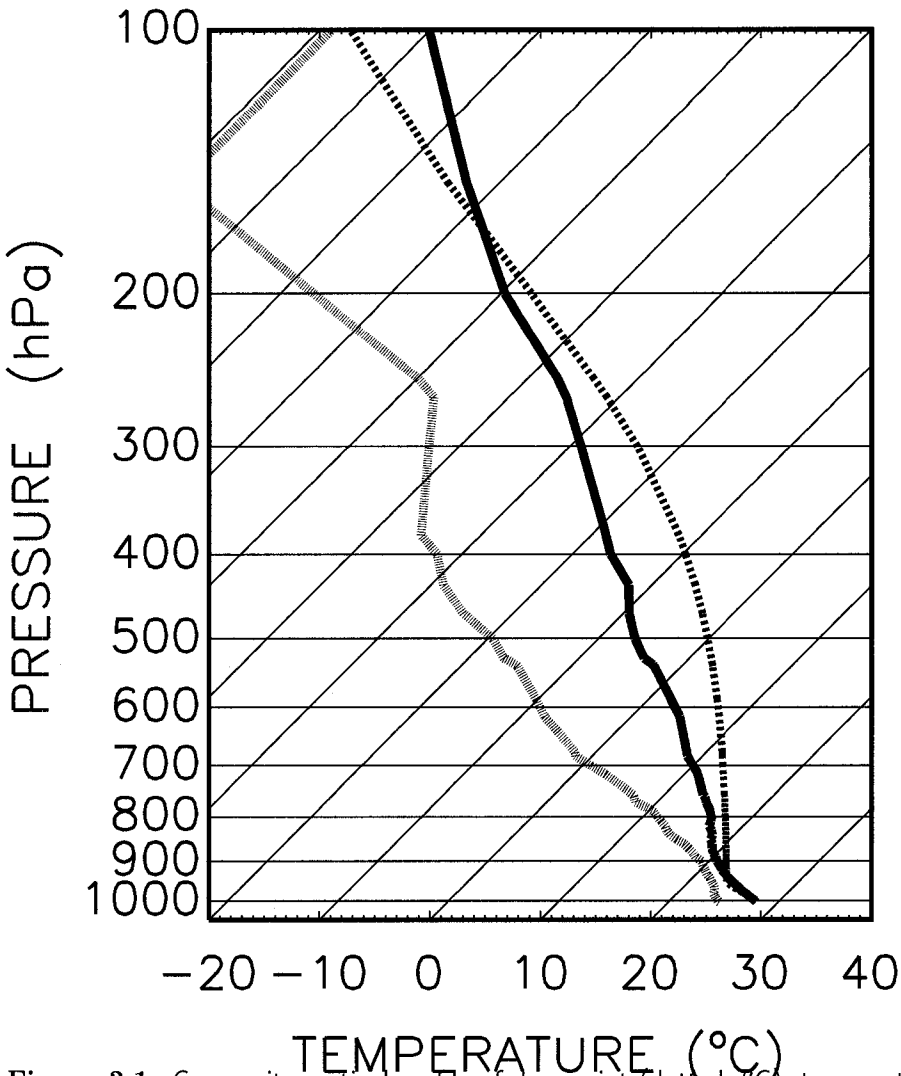

Figure 2.1: Composite vertical profile of dew point (dotted; °C), temperature (solid; °C) and hypothetical, undilute, surface-based parcel path temperature (dashed; °C).

of this thermodynamic sounding compared to the outer core of a strong tropical cyclone, especially in middle and upper levels, but we expect the general morphology of sheared convection to be characteristically analogous in other, similar thermodynamic environments.

To force the convection, we initialize the model runs with a warm bubble. For the first 200 s of each experiment,

$$H(x,y,z) = \begin{cases} \alpha \cos^4\left(\frac{\pi r}{2r_o}\right) \sin\left(\frac{\pi z}{z_o}\right) & \text{if } r \le r_o \text{ and } z \le z_o \\ 0 & \text{if } r > r_o \text{ or } z > z_o \end{cases}$$

is added to the ice-liquid potential temperature (θ_{il}) tendency, where $r = \sqrt{x^2 + y^2}$ is the horizontal radius from the center of the warm bubble, z is the physical height above the surface, $r_o = 27.5$ km, $z_o \approx 1.2$ km, and $\alpha = 0.01$ K s^{-1}. These parameters yield a 2 K net θ_{il} anomaly.

To gauge the overall effects of differing shear profiles on the convection created in this thermodynamic initial condition, we carry out 16 numerical experiments with varying vertical and horizontal tropical cyclone-like meridional wind shear profiles. These shears may be interpreted as approximate shears of the tangential wind due to a mean tropical cyclone vortex structure or shear owing to subsystem activity such as rainbands. The initial meridional component of the wind is parameterized as

$$v(x,y,z) = v_z z + v_x x + v_{\text{ref}}, \tag{2.1}$$

where v_z is the vertical wind shear, which remains constant up to 15 km and vanishes at higher altitudes, v_x is the constant horizontal wind shear, and v_{ref} is a constant wind that minimizes storm motion from the domain center. Our 16 experiments vary v_z over the values of 0, 5, 10, and 20 m s^{-1} per 15 km and v_x over the values 0, -2, -4, and -6 $\times$ 10^{-4} s^{-1}. For notational convenience, these experiments are hereafter labeled as vXXhY, where XX $\in \{00, 05, 10, 20\}$ denotes the different values of v_z normalized by (15 km)$^{-1}$ m s^{-1}, and Y $\in \{0, 2, 4, 6\}$ represents the magnitudes of v_x normalized by -1×10^{-4} s^{-1}.

All experiments are initialized in geostrophic and hydrostatic balance. We force the tendency of the zonal wind at the east and west boundaries to zero in order to eliminate spurious inflow that occurs with zonal gradients in the basic state flow. Despite diffusion, the initial horizontal gradients are fairly well maintained throughout the simulations.

As a dynamically symplifying assumption, the background absolute vorticity $\zeta_a = v_x + \bar{\zeta} + f$ is set equal to the constant 1×10^{-4} s^{-1}, where v_x is the parameter described in (2.1), $\bar{\zeta}$ is the constant, local background tropical cyclone vorticity, and $f = 5 \times 10^{-5}$ s^{-1}. This assumption is made to ensure inertial stability and to ensure that the convection experiences the same background vorticity in each experiment. The assumption of constant background absolute vorticity requires setting the model's constant Coriolis parameter to $\bar{\zeta} + f$ when horizontal shear is added to the initial condition.

The basic statistical morphology of the sixteen experiments is collected in the following table. Table 2.1 summarizes the following statistics of the convection through its lifetime: τ_{conv} (convective lifetime), h_{conv} (maximum convective height), w_{max} (maximum upward vertical velocity), and w_{min} (maximum downward vertical velocity). Each statistic has importance in the morphology of the convective cell. The convective lifetime (τ_{conv}) is calculated as the time when the model includes at least one point in the domain with upward motion greater than 0.5 m s^{-1} and represents the amount of time there is active convection occuring. The maximum convective height h_{conv} gives the maximum height of the convection at any point in the simulation. w_{max} and w_{min} are the maximum and minimum vertical velocities at any time during the simulation and give information about the maximum strength of the convective processes.

Rozoff et al. (2006) conjectured that convection may be strongly mitigated by strong horizontal shear found most frequently in the "moat," a region just outside the primary eyewall of a mature hurricane where convection is infrequent. Generally in agreement with Rozoff et al. (2006), we see that there is a threshold where the horizontal shear

	τ_{conv}	h_{conv}	w_{max}	w_{min}
v00h0	1.8	14.9	37.8	-9.2
v05h0	1.0	14.4	37.3	-13.8
v10h0	0.9	14.4	34.8	-13.6
v20h0	0.9	14.4	32.9	-11.3
v00h2	0.9	12.9	30.8	-9.1
v05h2	1.0	13.4	31.6	-8.9
v10h2	0.9	13.4	33.4	-9.5
v20h2	1.1	13.4	31.4	-10.4
v00h4	1.0	10.9	22.6	-6.2
v05h4	1.0	10.9	26.4	-7.5
v10h4	1.0	11.9	26.2	-9.3
v20h4	0.9	12.4	24.3	-7.6
v00h6	0.2	8.4	12.3	-4.0
v05h6	0.2	9.4	13.3	-3.7
v10h6	0.4	9.9	13.3	-3.9
v20h6	0.5	9.4	15.2	-3.9

Table 2.1: Convective lifetimes, τ_{conv} (hr), maximum height of convection, h_{conv} (km), maximum vertical speed, w_{max} (m s^{-1}), and minimum vertical speed, w_{min} (m s^{-1}) for all experiments.

becomes too strong to allow unforced convective elements to organize, even in a supportive thermodynamic environment. From this suite of experiments, we can conclude that, in the mature hurricane vortex, horizontal shearing may play as significant a role in determining the strength and lifespan of convection as the thermodynamics.

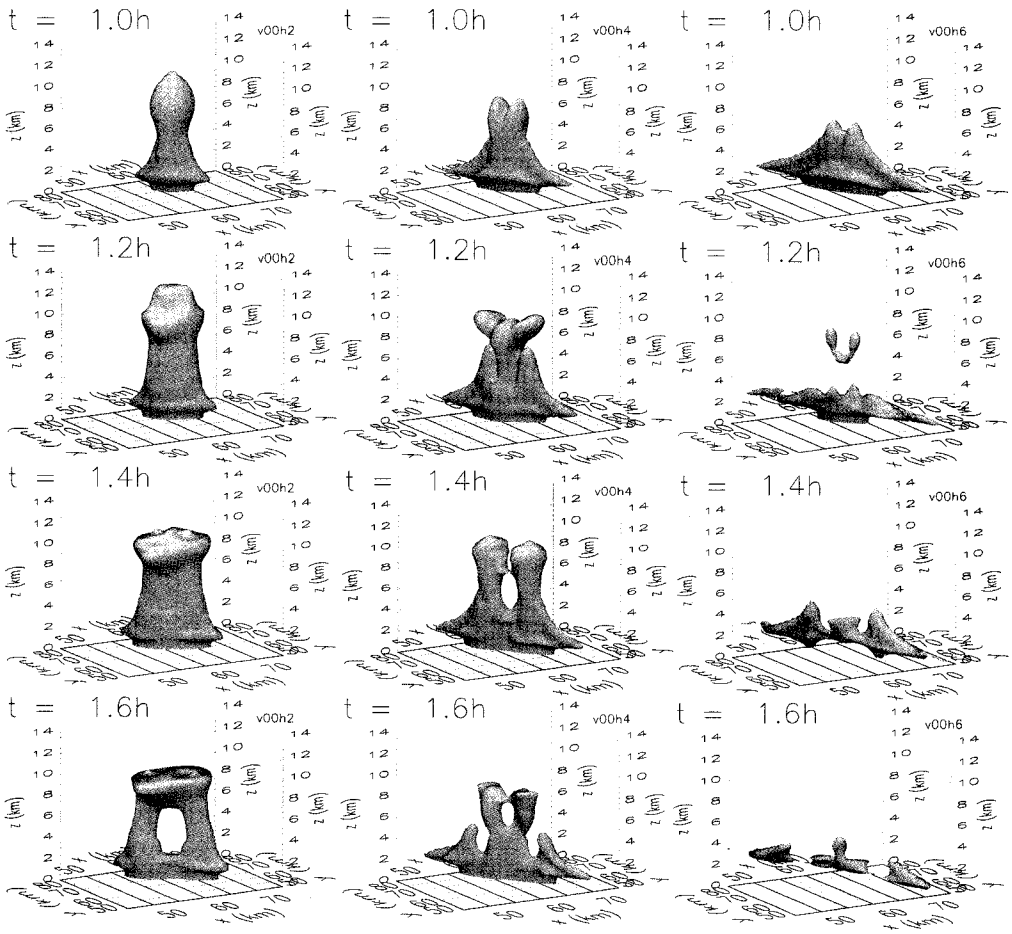

Figure 2.2: Total cloud condensate ($q_{\text{cond}} \geq 0.5$ g kg^{-1}) for experiments v00h2 (left column), v00h4 (middle column), and v00h6 (right column). Using q_{cond}, precipitation is seen beneath the cloud base.

In the nonzero horizontal shear cases, the initial bubble tends to get pulled into two separate updrafts (Figure 2.2). Part of the reduced lifetimes and strengths of the horizontally-sheared convection compared to the unsheared case may be due to this

partitioning of the convective energy. We do believe, though, that this is only a small part of the overall picture.

More discussion on the dynamics involved in these specific cases is deferred to an upcoming paper.

2.2 Convection Effects on the Mean State

Even though it is asymmetric, convection will generally have a projection onto the mean flow of the tropical cyclone. Despite the simplistic nature of our simulations, we can deduce some aspects of mean flow changes in the outer core of hurricanes due to these convective processes.

In this section, we will be examining changes to the mean flow in the meridional direction. Since the basic-state winds are parallel along this direction, this is the conceptual analogue to the azimuthal mean flow in a strong tropical cyclone vortex. However, since we are approximating the azimuthal mean of a hurricane with the meridional mean of a local region, the differences in the averaging length imply that the quantitative numbers from the model are not representative of quantitative changes that may occur in the tropical cyclone vortex. Thus, what are important in the following figures are not the magnitudes of the changes, but the qualitative pictures the figures show regarding the structure of the changes and their relative magnitudes.

We start with the basic temporal evolution of the mean potential vorticity (PV) field in the no shear (v00h0) case. Potential vorticity is defined as Ertel's potential vorticity: $Q = \rho^{-1}\left(\vec{\zeta_a} \cdot \nabla\theta\right)$, where $\vec{\zeta_a} = \nabla \times \vec{u} + \vec{\Omega}$ is the absolute vorticity vector, ρ is the density, and θ is the potential temperature.

Figure 2.3 shows the hourly mean PV plots for this case. During the convective period (first two hours), the mean PV changes remain strongly symmetric, due to the symmetric nature of the initial bubble and the symmetry of the forced convection. After this time, however, the mean PV field becomes more convoluted. Much of this can be

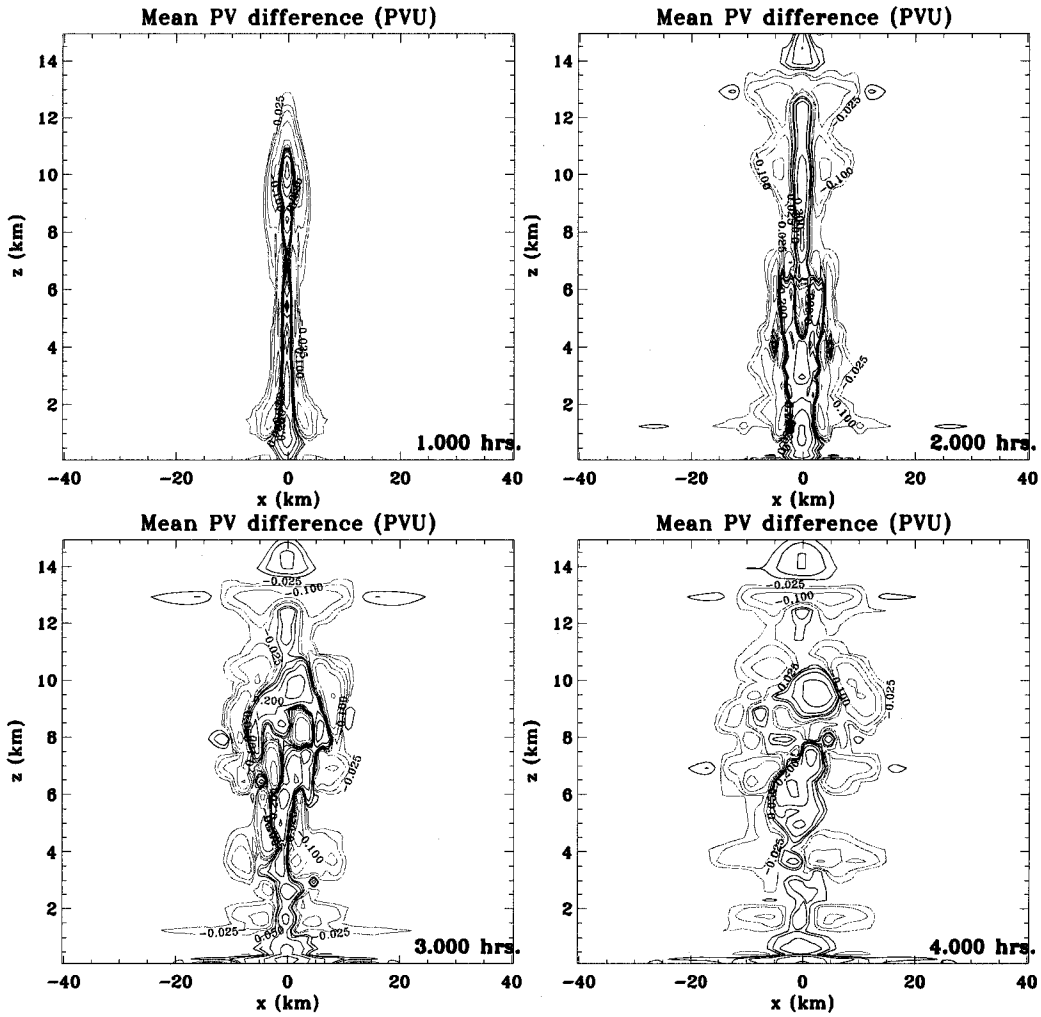

Figure 2.3: Mean potential vorticity change from initial values for the no shear (control) case. Time is 1.0 hours (top left), 2.0 hours (top right), 3.0 hours (bottom left), and 4.0 hours (bottom right). Contouring begins with ± 0.025 PVU and doubles with each increasing contour.

explained by basic, unforced PV dynamics as the PV generated by the now-complete convective processes interacts with itself in a nonlinear fashion. We also note that there is a strong positive PV change in the lowest levels. This can be attributed, as we note later, to a term in the PV generation equation that is analogous to the "stretching" of vorticity by the accelerating updraft.

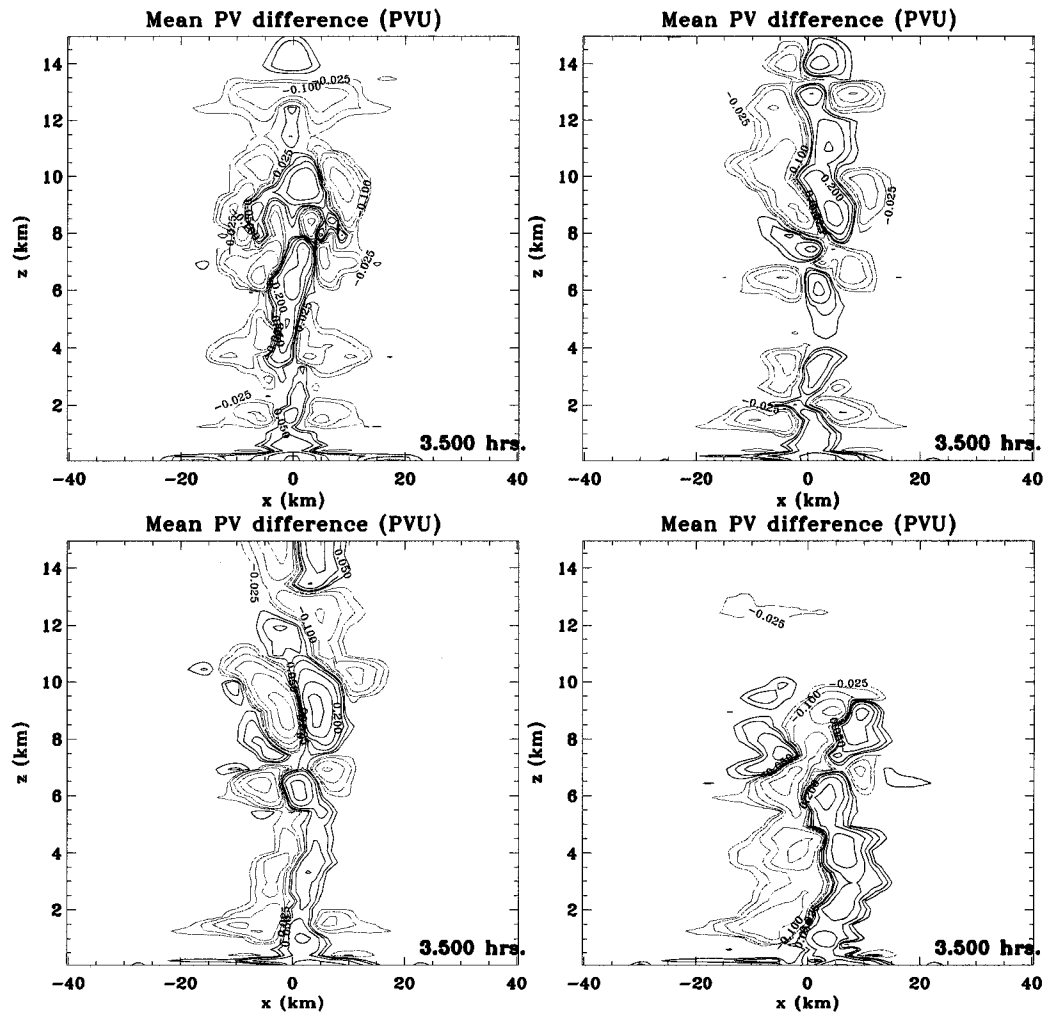

Figure 2.4: Mean potential vorticity change from initial values for the four cases with no horizontal shear. Time is 3.5 hours. Vertical shear values for each plot are 0 m/s (control, top left), 5 m/s (top right), 10 m/s (bottom left), and 20 m/s (bottom right). Contours as in Figure 2.3.

This term is encapsulated in the equation including diabatic change of potential vorticity from Haynes and McIntyre (1987):

$$\frac{\partial(\rho Q)}{\partial t} + \nabla \cdot \left(\rho Q \vec{u} - \dot{\theta}\vec{\zeta_a} - \vec{F} \times \nabla\theta\right) = 0, \tag{2.2}$$

where Q is Ertel's potential vorticity (defined previously) and $\vec{F}$ is the frictional force. Simplifying this to examine only the first-order effects of the diabatic heating associated with the convection, we get

$$\frac{\partial(\rho Q)}{\partial t} = \nabla \cdot (\dot{\theta}\vec{\zeta_a}). \tag{2.3}$$

The right-hand side of (2.3) can be rewritten as $\frac{\partial(\dot{\theta}\zeta_x)}{\partial x} + \frac{\partial(\dot{\theta}\zeta_y)}{\partial y} + \frac{\partial(\dot{\theta}\zeta_z)}{\partial z}$, where ζ_n is the magnitude of the $\vec{\zeta_a}$ vector in the n-direction. Given that the initial mean flow has a vorticity vector $\vec{\zeta_a} = v_z\hat{\mathbf{i}} + \zeta_a\hat{\mathbf{k}}$, we note that the change in potential vorticity by the diabatic effects is governed by two terms:

$$\frac{\partial\dot{\theta}}{\partial x}v_z + \frac{\partial\dot{\theta}}{\partial z}\zeta_a. \tag{2.4}$$

The latter is analogous to the "stretching-like" term in regular vorticity dynamics. The former term, however, is analogous to the "tilting-like" term. On the east and west edges of an updraft, a dipole of potential vorticity changes will be forced by the heating in the updraft and the vertical shear.

We now examine the role that vertical shearing has on mean PV generation by the convection. Figure 2.4 shows the change in the mean PV field after 3.5 hours of simulation for the four cases with no horizontal shear. Despite the convection's shorter lifetime and slightly weaker strength (Table 2.1), we note that the magnitudes of the mean PV changes are significantly higher in the vertically sheared cases than in the no shear control case. Additionally, compared to the no shear run, the vertically sheared cases have a different structure in their mean PV changes. Vertical shearing forces an axial antisymmetry in this field above the boundary layer, which demonstrates the importance of the "tilting-like" term in the generation of potential vorticity (i.e. (2.4)).

Furthermore, the stronger the vertical shearing, the stronger the magnitude of the PV change. Again, from a basic potential vorticity standpoint (e.g. (2.4)), this is not surprising, since the change in vertical vorticity generation by the "tilting-like" term is proportional to the magnitude of the horizontal vorticity which is being "tilted". Since the vertical shear cases all approximately mimic each other in lifetime and updraft velocity, we suggest that much of the change in the potential vorticity generation in these cases can be explained almost exclusively by the magnitude of the vertical shear itself.

In the boundary layer, we see the same strongly positive mean PV change that we saw in the previous unsheared case.

Turning our attention to the influence horizontal shearing has on the mean potential vorticity structure, we examine mean PV difference field at 3.5 hours for the four cases with no vertical shear, but differing horizontal shear (Figure 2.5).

At a first glance, it appears as though horizontal shearing has two main effects on the mean potential vorticity field: symmetrization and weakening. However, careful study of these particular cases shows that the weakening of the mean PV field is most likely related to the shortened lifetimes of the only horizontally-sheared cases (Table 2.1).

The symmetrization of the PV field around the central axis, though, is something consistent between the cases and bares some note. This symmetrization is likely a consequence of dominance of the "stretching-like" term, as "tilting" would be a purely nonlinear term since there is no environmental horizontal vorticity to tilt (e.g. (2.4)).

The most interesting feature, though, is the structure of the pattern, which shows a core of positive PV changes surrounded by flanks of negative changes. This mimics the structure of a basic thunderstorm updraft (e.g. Figure 2.3), which helps reinforce the "stretching" dominance hypothesis.

To best understand the effects of combinations of horizontal and vertical shear on the mean potential vorticity dynamics, we look for experiments with similar convective

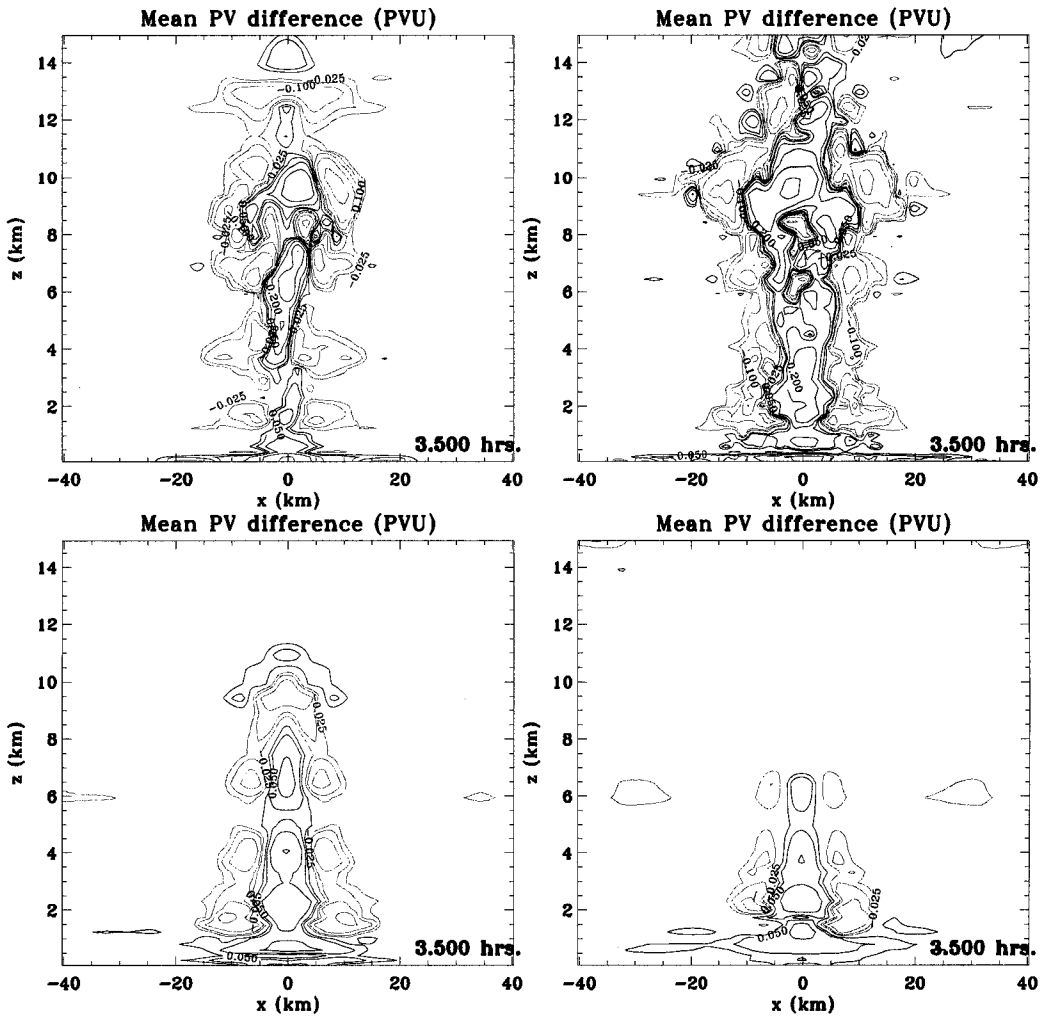

Figure 2.5: Mean potential vorticity change from initial values for the four cases with no vertical shear. Time is 3.5 hours. Horizontal shear values for each plot are 0 $\times$ 10^{-4} s^{-1} (control, top left), -2 $\times$ 10^{-4} s^{-1} (top right), -4 $\times$ 10^{-4} s^{-1} (bottom left), and -6 $\times$ 10^{-4} s^{-1} (bottom right). Contours as in Figure 2.3.

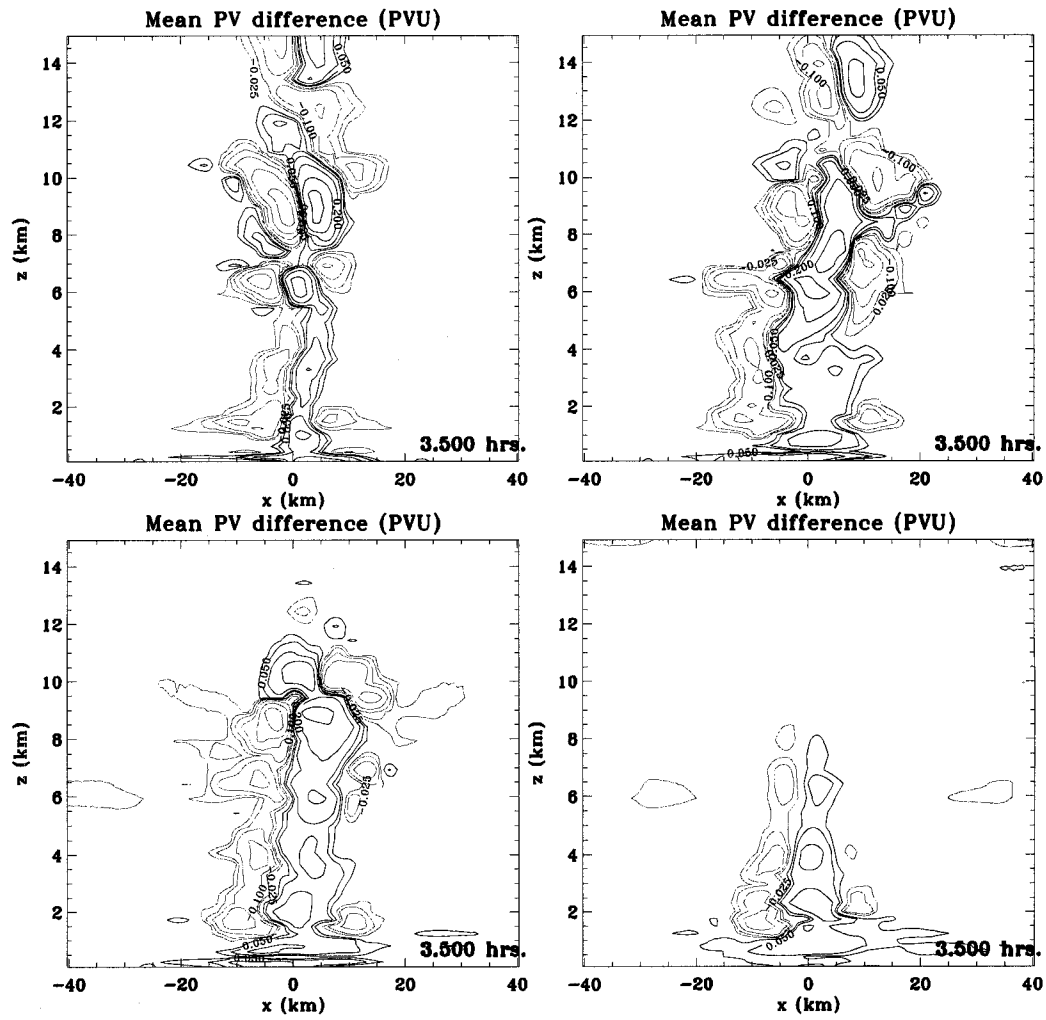

Figure 2.6: Mean potential vorticity change from initial values for the four cases with 10 m/s vertical shear. Time is 3.5 hours. Horizontal shear values for each plot are 0 $\times$ 10^{-4} s^{-1} (control, top left), -2 $\times$ 10^{-4} s^{-1} (top right), -4 $\times$ 10^{-4} s^{-1} (bottom left), and -6 $\times$ 10^{-4} s^{-1} (bottom right). Contours as in Figure 2.3.

statistics to contrast and compare results from those experiments. From this criterion, we focus on the 10 m/s vertical shear cases.

Figure 2.6 shows the four horizontal shear cases from the 10 m/s vertical shear experiments. The three weakest horizontal shear cases are similar in their statistical morphology, so we examine the trends from these three experiments while touching on the strongest case. The basic structure from the horizontal shearing of a positive PV change core with negative PV changes on its flanks is still present, but is now tilted to the east with height. This pattern, though, is not clean. There is a lot of additional noise which cannot be explained by the mean plots alone. To better understand how the mean PV patterns changes are manifest in three-dimensional space, we examine specific horizontal cross-sections through the space at this time.

Figure 2.7 are four horizontal cross-sections of the potential vorticity field at different heights for the 10 m/s and $v_x = -2\times10^{-4}$ s^{-1} case. At the lowest level, we note that much of the small potential vorticity changes have advected away from the center of the domain. However, as we have seen with the previous cases, the sign of this change is positive. Going up in height, though, the patterns become more complex. At both 2 km and 4 km, we note that the positive PV has been strained while the negative PV is generally more consolidated. Given that the shearing flow is anticyclonic, this observation is not surprising. Additionally, the pattern in the lower layers of the corresponding plot from Figure 2.6 is easily explained by the structure seen here, with the stronger updraft on the west side dominating the mean PV change, leaving a filament of positive PV and a core of negative PV to its northwest. That produces the apparent asymmetry in the mean PV change diagram in those levels. Since our simulations are run out to only 4 hours, we cannot describe the exact final state of this shearing and straining process. However, this short-time evolution points to a reasonably extrapolated end-state.

At 6 km, though, the basic structure has changed to a generally positive core of PV with a moat of negative PV around it. This gives a mean profile that is more

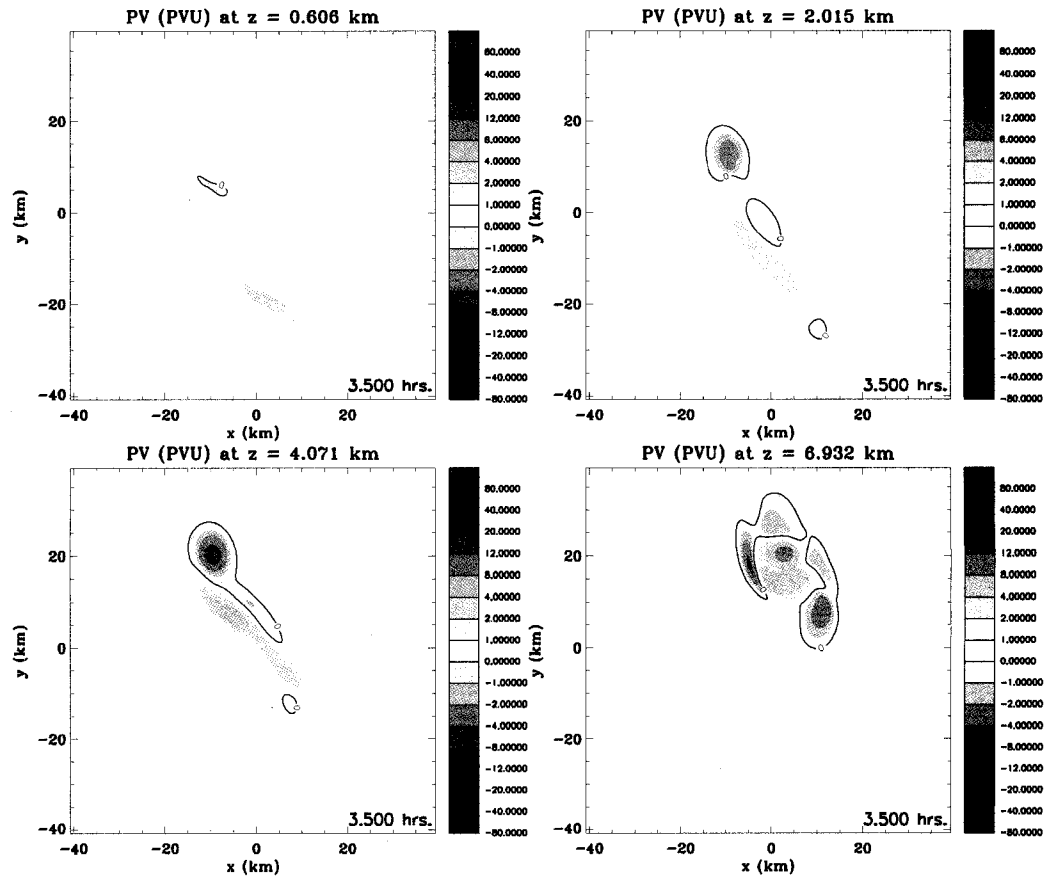

Figure 2.7: Potential vorticity for four heights with 10 m/s vertical shear and $v_x = -2 \times 10^{-4}$ s^{-1}. Time is 3.5 hours.

symmetric-looking, although this is merely a snapshot of what is a complex nonlinear evolution.

Examination of the mean potential vorticity changes after the end of the active convection period shows some interesting results. First, horizontal shearing alone tends to have a symmetrizing effect on the mean PV changes. Vertical shear alone, however, leaves an axial antisymmetric mean PV change pattern around the central axis, due to the strong tilting of the environmental horizontal vorticity into the vertical where the isentropic gradients are stronger. The combination of horizontal and vertical shears tends to force a mean PV change that is generally axially antisymmetric where the axis tilted in height. The exact reasons for the emergence of this pattern are still under investigation, but are nonetheless intriguing.

Other mean fields show expected results. The mean potential temperature change (Figure 2.8) shows a slight warming near the mid-layers and cold pool near the surface, indicating the immediate stabilization of this region of the mean vortex to additional convection.

Kinematic fields (Figure 2.9) show the signature of a slight spin-up of vorticity in the mean, particularly at the lowest model layers. The change in the mean meridional wind is generally small in all cases, but are reduced in the horizontally-sheared cases. In the boundary layer (below 1 km height), the meridional wind shows evidence of a strong positive vorticial spin-up, while right above the boundary layer (above 1 km height) there is a weak anticyclonic spin-down in the mean. We see this in the previous potential vorticity figures.

Understanding exactly how these kinematic fields are changed by these basic convective elements is a strong step toward predicting changes to the kinematics of the tropical cyclone vortex outside its core region. Using the knowledge gathered by this study, we conclude that unforced convective processes will tend to stretch the ambient vorticity in the boundary layer, generally forcing a spin-up of vorticity in the sub-cloud layers.

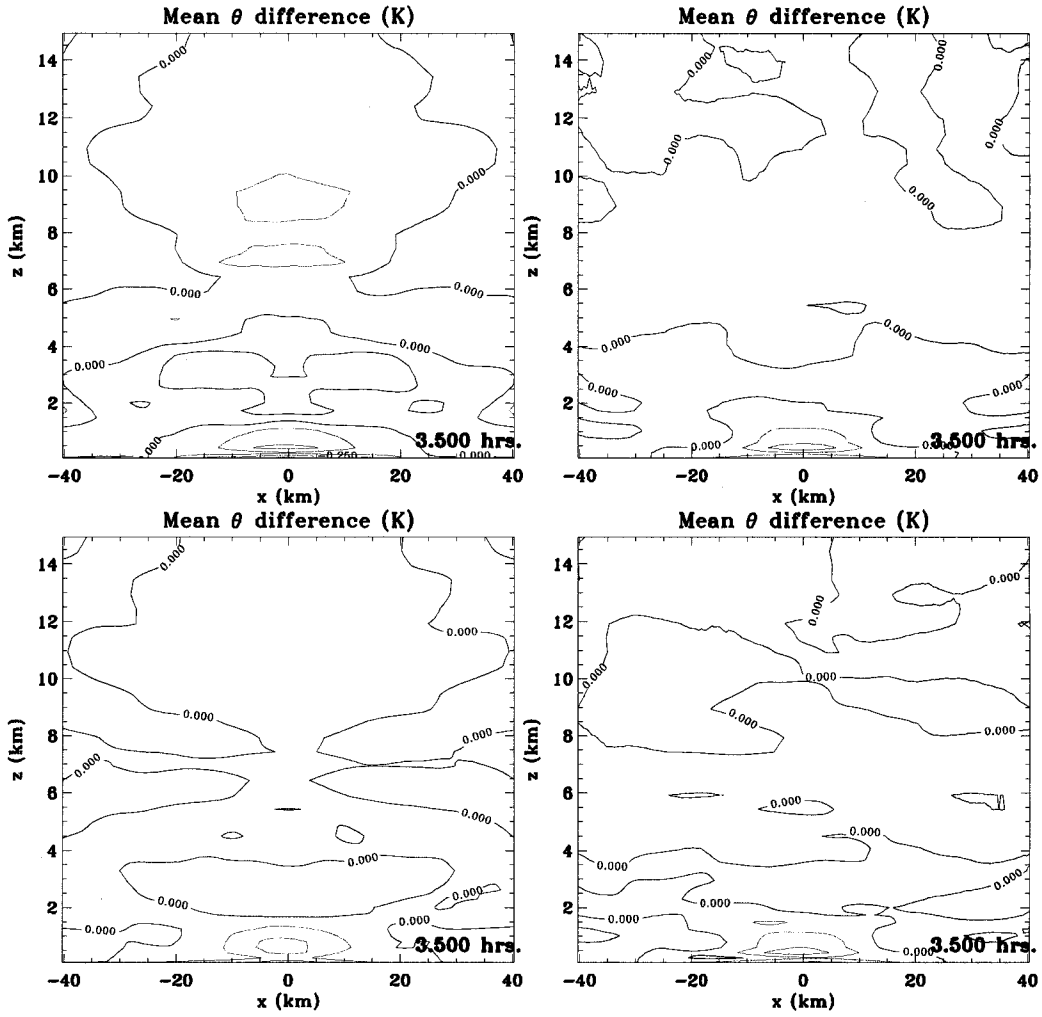

Figure 2.8: Change in the mean potential temperature after 3.5 hours for four different experiments. Experiments shown are v00h0 (top left), v00h4 (top right), v10h0 (bottom left), and v10h4 (bottom right). Contouring interval is 0.125 K.

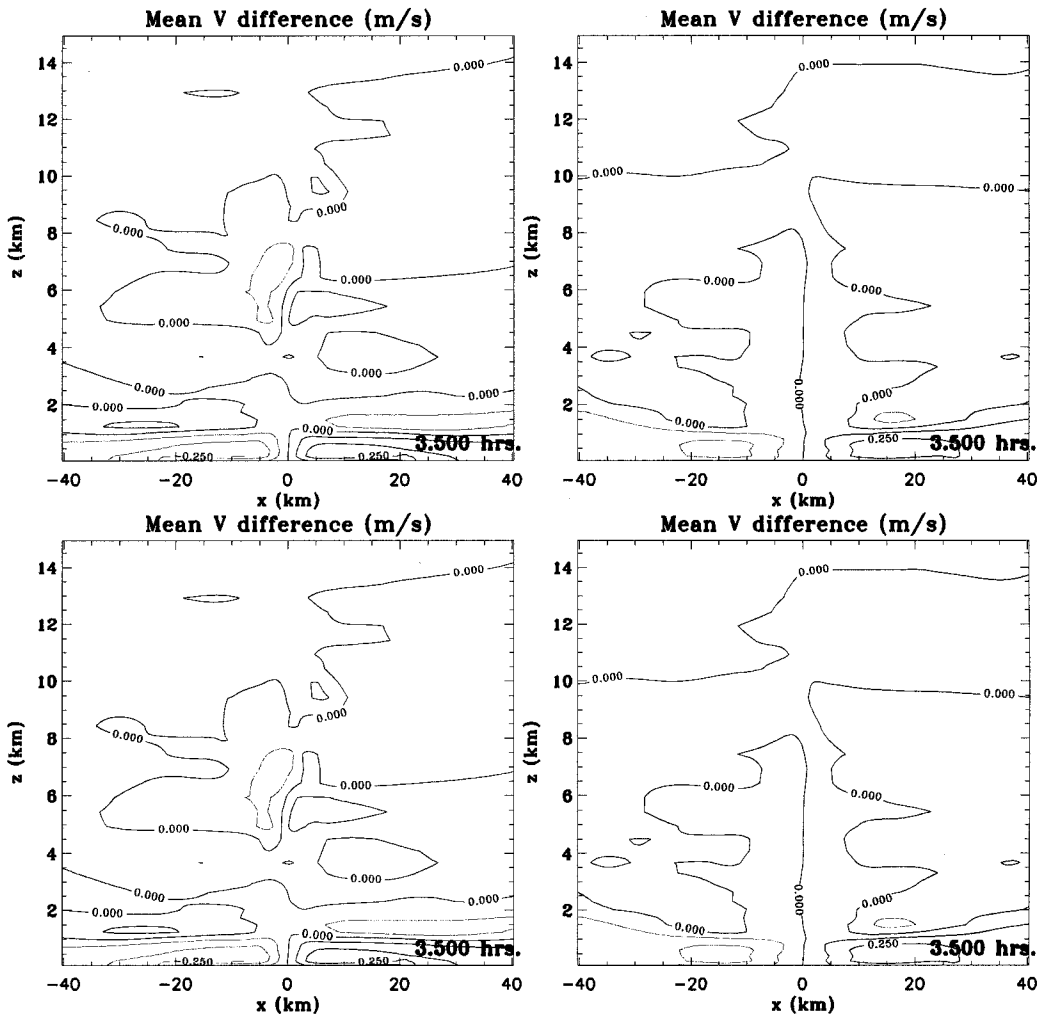

Figure 2.9: Change in the mean meridional wind after 3.5 hours for four different experiments. Experiments shown are v00h0 (top left), v00h4 (top right), v10h0 (bottom left), and v10h4 (bottom right). Contouring interval is 0.125 m s^{-1}.

Above the boundary layer, the "tilting-like" term will be dominant as the heating "tilts" the potential vorticity into dipolar structures. Because of this, the mean flow projection of vertically-sheared convection is generally antisymmetric about an axis. Horizontal shear tends to tilt this axis eastward (radially outward, if using the hurricane analogy) with height. Additionally, increasing horizontal shearing appears to reduce the lifetime and spatial coverage of unforced convective processes once it exceeds a critical threshold which, in this set of experiments, is between 4 and 6 $\times$ 10^{-4} s^{-1}. These values may be significantly different in other thermodynamic environments, but highlight the potential role of horizontal shearing on the lifetime and frequency of convection.

Chapter 3

HURRICANE MODEL AND BASIC EVOLUTION

3.1 Hurricane Simulation Specifics

To examine the dynamics involved in the formation of the secondary eyewall, we chose to model the phenomenon instead of attempting to observe it. The main reason for this was that there were a large number of potential processes that could be in play during secondary eyewall formation and current observational techniques for hurricanes rarely observe the vortex with fine enough temporal resolution to test potential formation hypotheses. Thus, experimental setup is essential to the success of this study.

Since each full-physics model is slightly different in its physical representations, it is best to let the model spin up its own hurricane vortex, rather than starting the model with an observed tropical cyclone. This allows the model to evolve a hurricane vortex in an internally consistent manner. This also gives us the ability to gauge the realism of the modelled storm from a holistic perspective. Thus, we run the model for the lifetime of a mature hurricane from its genesis through any eyewall cycles that it may undergo.

For this study, we employ the Regional Atmospheric Modeling System (RAMS) (Pielke et al., 1992; Cotton et al., 2003). Further information on the RAMS can be found in Appendix A.

To simulate a hurricane vortex through a long period of its life, the simulation domain is made sufficiently large to ensure that the storm dynamics are not influenced by the outer boundary conditions. Three nested grids are therefore used with uniform horizontal grid spacing of 24, 6, and 2 km and 168, 170, and 251 grid points on each

grid, respectively. This translates to respective horizontal grid domain lengths of 4032, 1020, and 502 km. Each inner grid is centered on the center of the outermost grid. To help ensure that the simulated storm remains near the center of the domain, we initialize the environment to be at rest (excluding the weak mesoscale convective vortex at the center). Additionally, we run the model on an f-plane centered at 15°N; this neglects the meridional gradient of planetary vorticity that induces a northwestward vortex motion (e.g. McWilliams and Flierl, 1979; Shapiro, 1992). The f-plane configuration guarantees that the bulk of the convective-scale dynamics are represented on the 2 km grid through the simulation.

The outermost grid is made cyclic in the horizontal directions to help ensure that mass and wind fields remain continuous in the domain. Given that the typical hurricane vortex comprises an area that is a small fraction of the approximately 16,000,000 km^2 outer grid, it is believed that the cyclic boundary condition coupled with the large domain size should be sufficient to prevent the simulated storm from interacting strongly with itself.

The simulated domain has 30 vertical levels stretching non-uniformly from the surface to approximately 26 km in height. The vertical grid spacing starts at 300 m near the surface and increases to 1800 m at the top of the domain, utilizing a stretch factor of 1.065. We use a rigid bottom boundary with latent and sensible heat fluxes most appropriate to represent a flat sea surface. The sea surface temperature is fixed throughout all domains at 28°C. The upper boundary is closed, but includes a Rayleigh "sponge" layer exclusively in the stratosphere (uppermost six levels) to strongly damp upward propagating gravity waves and artificial gravity wave reflection off the model top.

The model's initial condition is similar to the initial vortex used in Montgomery et al. (2006, hereafter referred to as M06). In M06, the control simulation was initialized with a mesoscale convective vortex (MCV) in gradient and hydrostatic balance with radius of maximum winds (RMW) at 75 km from the center of circulation and 4 km

altitude above the sea surface, quantitatively similar to observations (e.g. Raymond et al., 1998; Reasor et al., 2005). The maximum tangential wind speed of the initial MCV in the M06 control simulation is approximately 6.5 m s^{-1}. Because of the large computational and data storage demands required to carry out these extended tropical cyclone lifecycle experiments, the initial wind speed maximum of the MCV is increased to approximately 10 m s^{-1} so as to generate a tropical storm surface vortex somewhat sooner than the M06 control experiment. Convection is stimulated with a warm bubble near the RMW at the start of the simulation. The initial vertical sounding is based off the Jordan (1958) climatological hurricane season sounding as described in M06 and depicted in Figure 3.1. Outside the MCV, the environment is initialized with this basic sounding. Near the center of the initial MCV, though, the lower and middle layers of the sounding are moistened somewhat to account for increased sea-to-air moisture fluxes in the vicinity of the vortex. The moistening anomaly results in an increase in the water vapor mixing ratio by 1.3 g kg^{-1} near the surface in the center of the MCV.

Two temporal views of the simulated control storm are summarized here. The first is the complete 204-hour simulation at three-hour output intervals, giving an overview of the entire simulated evolution. The second view begins at 156 hours, running for 24 hours with a six-minute output interval.

3.2 Simulated Hurricane Evolution

Since the purpose of this work was to produce a realistic long-time hurricane simulation, it is important to verify that the simulated tropical cyclone evolves in a realistic manner.

For the purposes of definition, we will be referring to the "inner core" and "outer core" portions of the simulated hurricane. The "inner core" of a hurricane vortex includes the eye, the eyewall, and the region just outside the eyewall. The "outer core" refers

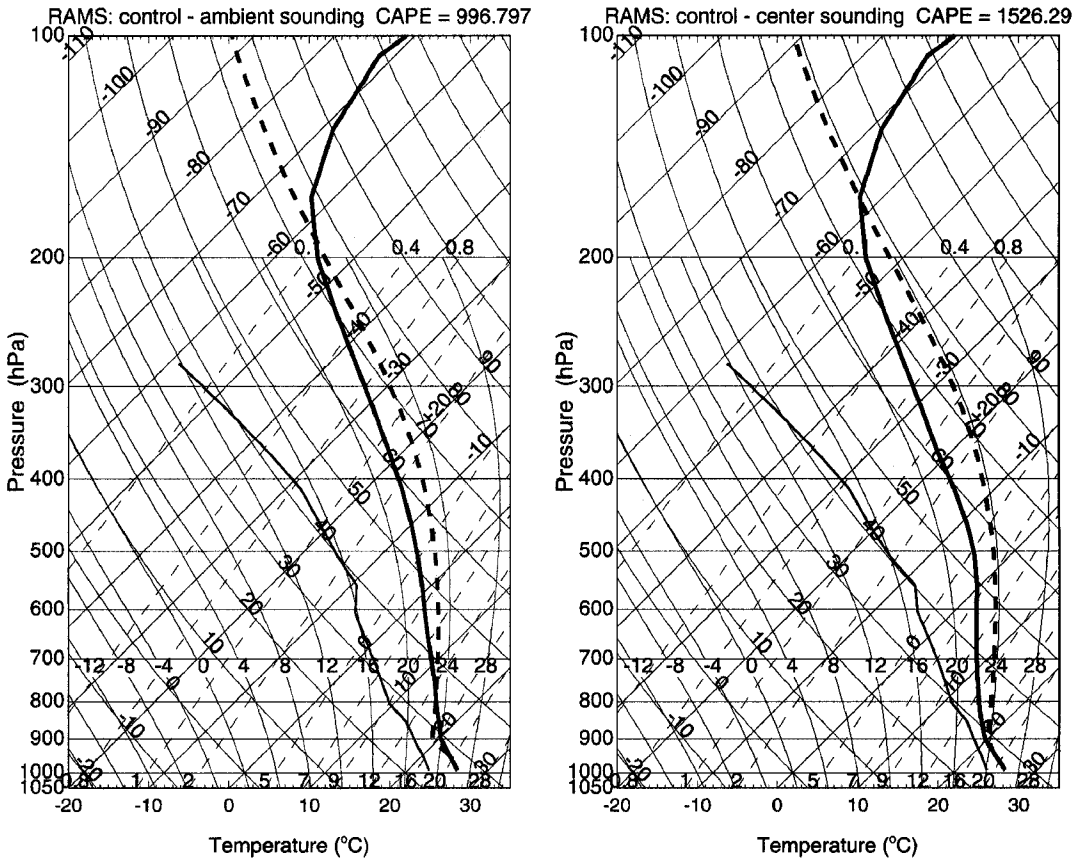

Figure 3.1: Representative soundings for the control experiment. Frame (a) depicts the sounding in the environment, while frame (b) depicts the sounding at the center of the MCV. Figure taken from Montgomery et al. (2006).

to the region outside this where rainbands frequently occur. The definitions are somewhat vague, but aid in the explanation and identification of features in differently-sized vortices.

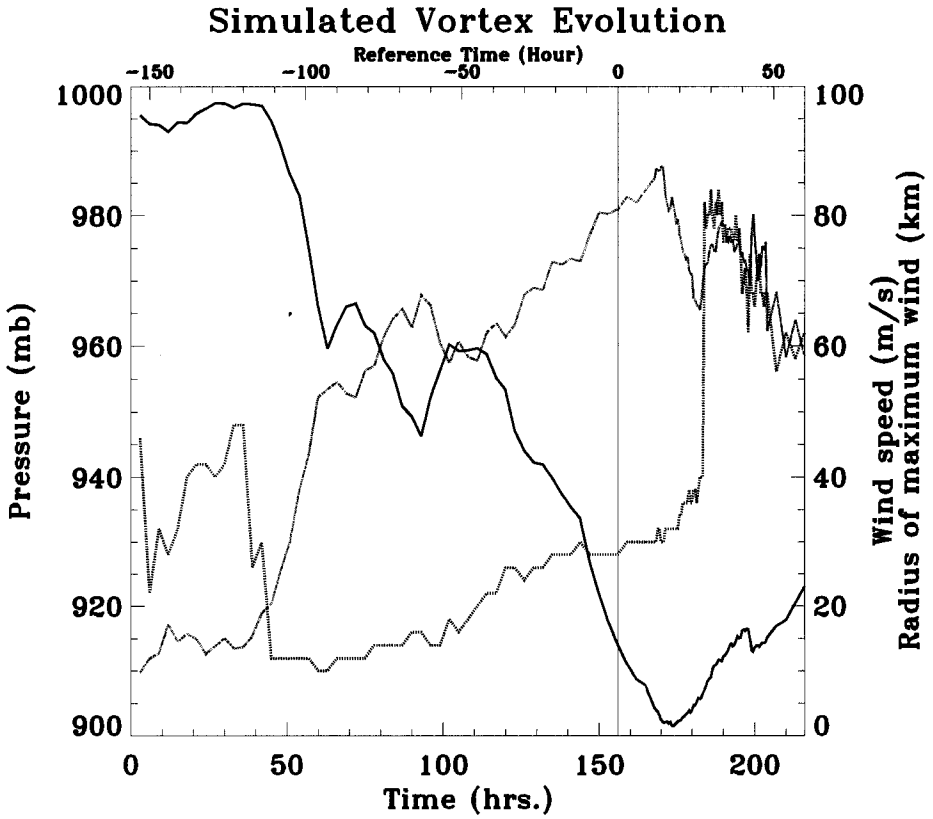

Figure 3.2: Evolution of the control simulation. The solid line is lowest pressure observed at the lowest model layer (approximately 150 m). The dotted line is the maximum azimuthal mean tangential velocity in the lowest model layer. The dashed line is the radius of the maximum mean tangential velocity at the lowest model layer in kilometers.

Figure 3.2 shows the evolution of the storm utilizing three commonly used hurricane metrics: minimum pressure, maximum azimuthal mean tangential winds, and the radius of maximum mean tangential winds (RMW). In our case, we calculate these storm metrics from the lowest model layer above the surface (approximately 150 m), except for the maximum mean tangential winds, which are calculated from the entire mean profile and are typically found just above the 1 km level.

The model storm takes approximately 48 hours to undergo the transition from a weak MCV to a hurricane-strength vortex, nearly 12 to 18 hours faster than the control case in M06. After attaining tropical storm strength, the storm continues intensifying rapidly into a small hurricane vortex, as evidenced by its 10 km RMW and 40 to 50 m s^{-1} mean tangential winds.

After 60 hours, the storm begins a phase of intensity fluctuations that lasts for nearly 60 hours. During this period, it is noteworthy that the RMW gradually increases from approximately 10 to 25 km while the maximum mean tangential winds waver around 60 m s^{-1}. The spatial expansion of a maturing hurricane vortex is not anticipated from simple theoretical considerations using axisymmetric balanced dynamics, which forecasts that slowly evolving hurricane eyewalls contract, not expand (Shapiro and Willoughby 1982). This period of expansion in the numerical simulation does not include any secondary eyewall cycles. Further analysis of this phenomenon is deferred to future research in due course.

After 110 hours, the storm enters a period of rapid intensification. The maximum mean winds increase from approximately 60 m s^{-1} to over 80 m s^{-1} through the next 60 hours, while the near-surface minimum pressure drops another 50 mb. At 156 hours into the simulation, we denote a new time coordinate corresponding to our focused interest in this time period. We call this point in time Hour 0.

From Hour 0 on, the control simulation undergoes significant intensity changes. The maximum mean winds continue to increase until about Hour 16-18, when they begin to decrease rapidly. During this time frame, the storm continues its central pressure decrease. The near-surface pressure falls until approximately Hour 22-24, when it reaches a minimum around 903 mb. Using the height of this level (147 m), an assumed density appropriate to the boundary layer, and the hydrostatic assumption, we approximate the sea-level pressure of this storm to 921 mb. Using a basic pressure-wind relationship for hurricanes in the Atlantic basin (Dvorak 1995), we see that statistically, this central

pressure is in line with an Atlantic storm with sustained winds of 140 kts or 72 m s^{-1}, which is somewhat under our modeled values of 80-85 m s^{-1}. Since Figure 3.2 shows the maximum mean winds and the Dvorak intensity uses surface winds, we use the near-surface mean tangential wind maximum of approximately 75 m s^{-1} from the model. This agrees well with the Atlantic-basin Dvorak pressure-wind relationship deduced from observational data.

Between Hours 24 and 30, though, the secondary eyewall becomes evident as it begins to envelop and replace the inner eyewall. This can be seen in the abrupt jump in the RMW from approximately 30 km to 80 km. At this point, the control simulation's new eyewall begins to shrink in size again, consistent with eyewall replacement theory (Shapiro and Willoughby, 1982). Maximum mean winds decrease, then fluctuate, while near-surface pressures begin to rise as the control simulation adjusts to a new balanced state.

While a summary view like this is useful, it is more instructive to look carefully at each of the phases described above.

3.2.1 Genesis Phase

The genesis phase of this storm is, unsurprisingly, well-described by M06. During the first two days of the simulation, sporadic vortical convection (referred to as vortical hot towers in M06) accumulates potential vorticity around the center of circulation. As can be insinuated from Figure 3.3, the convection is well-scattered through the MCV during the early period. Periods of mergers of vortical hot towers and their associated vorticity begin to consolidate positive PV into a small core. By the end of this two day period, the convection, organizing into banded structures, appear to force a strong change in the core, forcing an order of magnitude change in the central potential vorticity over the span of 18 hours. As pointed out in M06, this rapid intensification phase is consistent with WISHE amplification theory (Rotunno and Emanuel, 1987).

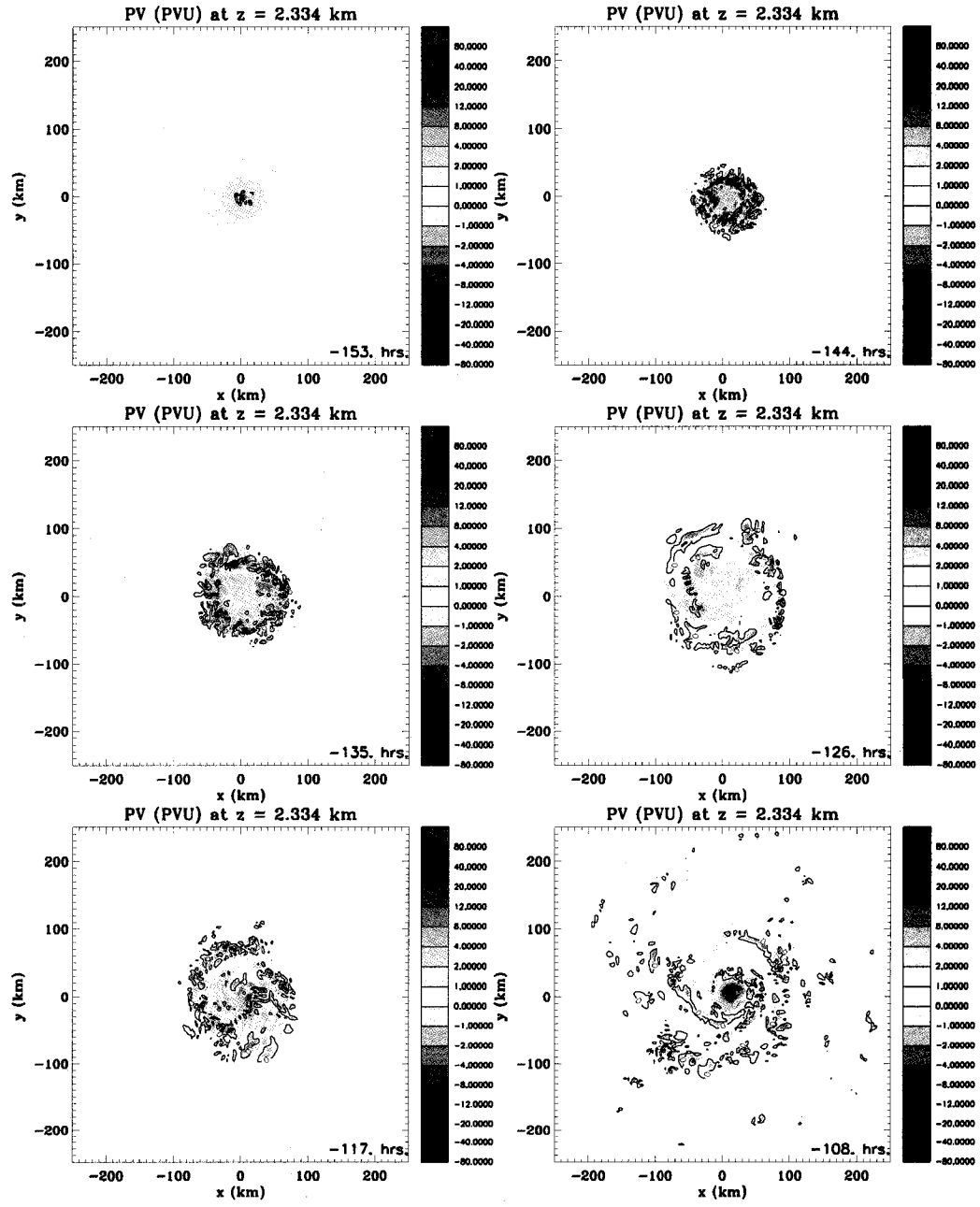

Figure 3.3: Early time potential vorticity cross-sections. Time, using Hour 0 as the origin, is denoted in the lower-right corner of each panel.

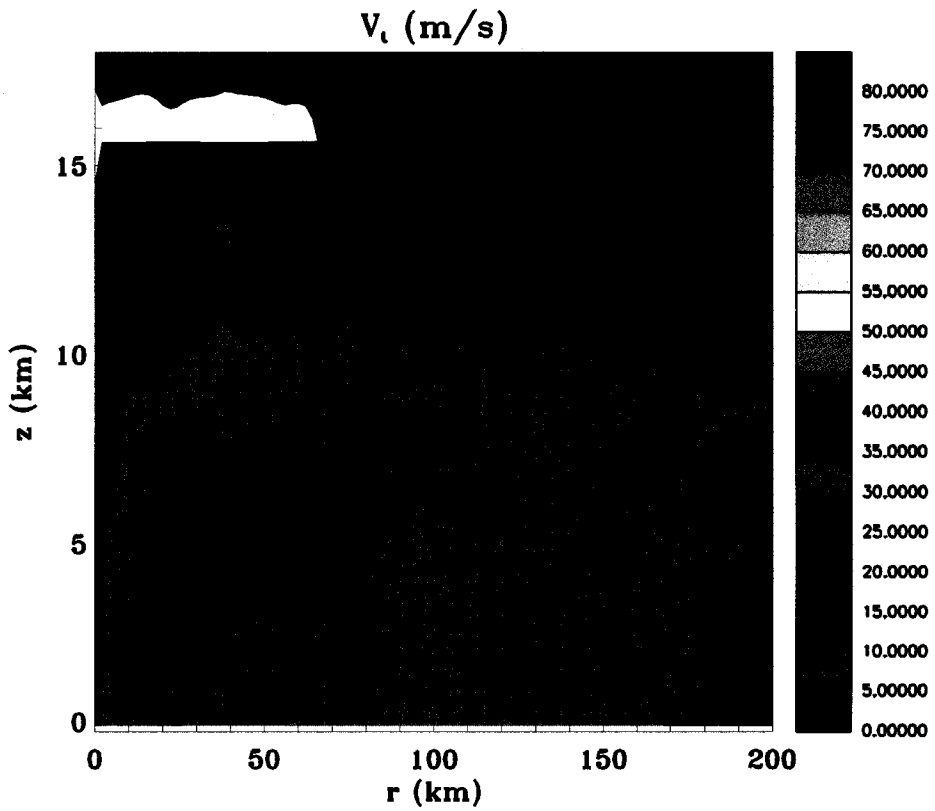

Figure 3.4: Azimuthal mean tangential wind for the control simulation at Hour -108.

The modeled storm begins small, with a eyewall radius of approximately 8 to 12 km, when it attains hurricane strength. Figure 3.4 shows the radius/height azimuthal mean tangential wind profile of the storm at Hour -108. The storm is still relatively shallow in depth, stretching up to approximately 10 km height. Similar evolution is seen in the control run of M06 (cf. Fig. 4 a, c, e).

3.2.2 Mature Phase

After the control simulation strengthens rapidly into a hurricane, it undergoes a couple periods of intensity and structural change. In addition to the basic evolutionary parameters displayed in Figure 3.2, we examine time-radius plots of azimuthal mean quantities to quantify the changes in the control simulation during this maturing phase.

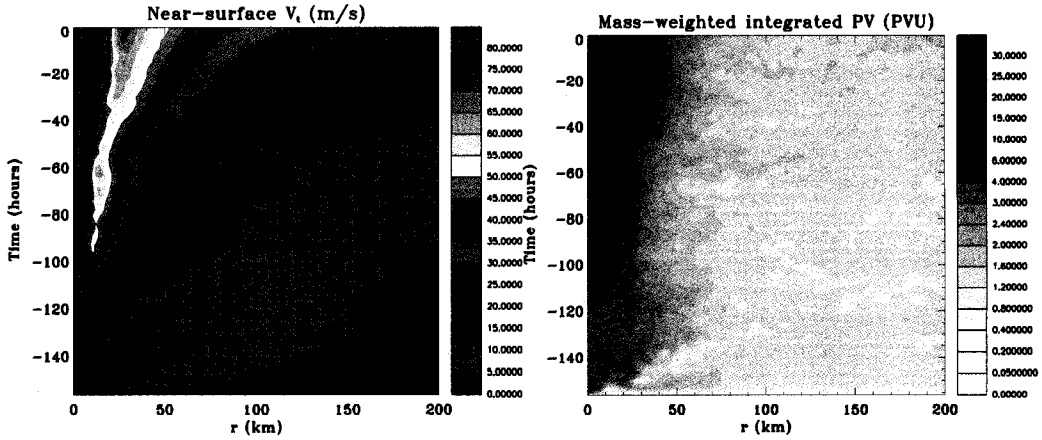

Figure 3.5: Time-radius plot of the lowest level azimuthal mean tangential winds (left) and the mass-weighted, vertically-integrated azimuthal mean PV (right). Time is indexed with Hour 0 being the origin.

Figure 3.5 displays the azimuthal mean tangential winds at the lowest model layer as well as the mass-weighted, vertically-integrated azimuthal mean potential vorticity through the evolution of the control simulation. Examining the period between Hours -100 and 0, we see two distinct periods. First, from Hour -100 to approximately Hour -55, the radial size of the control simulation's RMW barely changes. However, the hurricane

strengthens its maximum tangential winds by approximately 10 m s^{-1} during this time frame.

This time period is potentially contradictory to the basic axisymmetric theory of Shapiro and Willoughby (1982). In their study, they found that the primary feedback by the secondary circulation in the intensifying hurricane vortex is to decrease the RMW. This was due to the fact that the maximum change in tangential velocity due to a convective heating profile tends to be on the inside of the ring of convection. Since the RMW and the eyewall's convection are very closely overlapped, this implies that the two concurrent phenomena should both tend to shrink in size, barring frictional or diffusive effects. In the control simulation's case, though, the storm intensifies during this period while the storm's RMW remains approximately the same. We leave this as an open question.

After this time period, there is a period (approximately 24-30 hours) where the only change in the storm is the gentle increase in its radius of maximum winds. This is an interesting evolutionary time since this is one of the first periods where there appear to be significant spiral bands outside the core of the control simulation (Figure 3.6). The evolutionary dynamics that control the changes in the hurricane from the end of genesis to major are still unknown. There is some question as the reality of this simulation with regard to this particular period, as observations are somewhat inconclusive as to whether or not a tropical cyclone's RMW can grow without undergoing a secondary eyewall cycle.

From the end of this period on, the control simulation undergoes a steady intensification period that we see in Figure 3.7. We note that the storm is gaining additional strong bands of convection during this time. These bands may aid in forcing the increase in the RMW. The radius of maximum winds increases gradually during this period, as well as the storm's size of gale-force winds (Figure 3.5). The maximum near-surface mean winds of the storm increase from approximately 50 m s^{-1} to 75 m s^{-1} by Hour 12. The minimum near-surface pressure occurs shortly after this time.

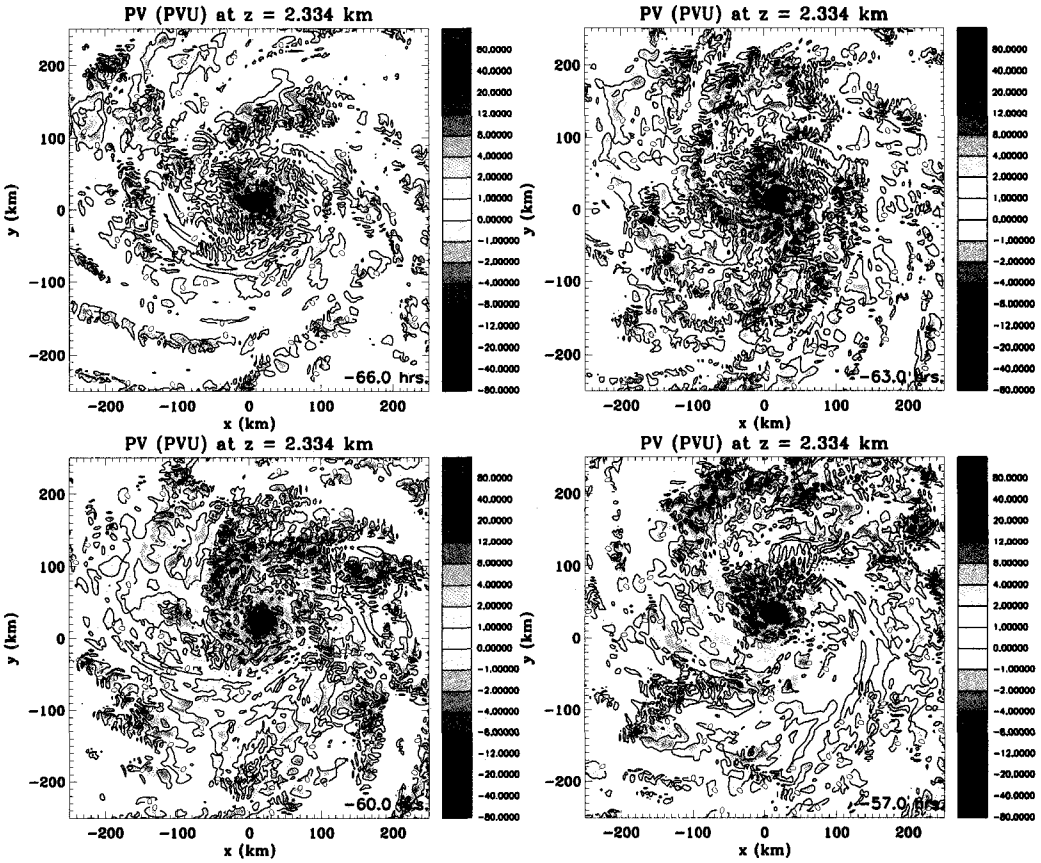

Figure 3.6: Low-level potential vorticity cross-sections between -66 and -57 Hours.

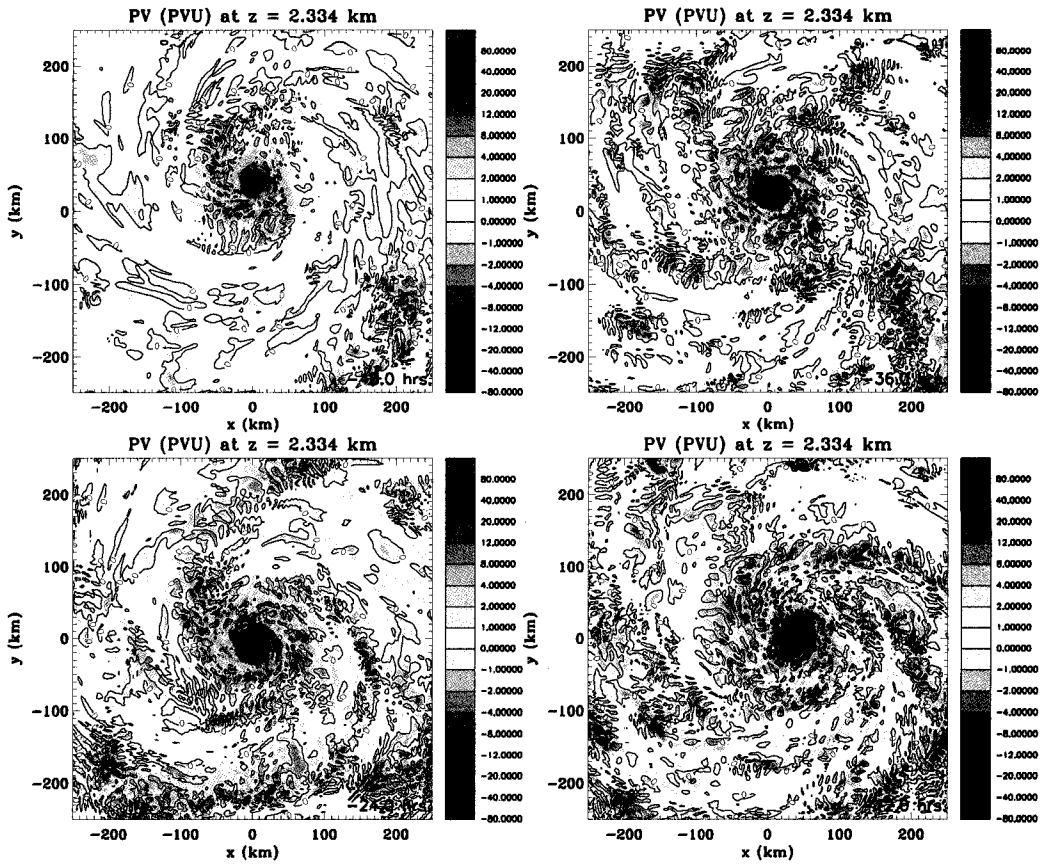

Figure 3.7: Low-level potential vorticity cross-sections between -48 and -12 Hours.

Figure 3.8 shows the mean tangential velocity profile and mean relative vorticity profile for the control simulation at Hour 12. At the top of the boundary layer are winds in excess of 80 m s^{-1}. Inside the radius of maximum winds is a ring of elevated vorticity. The low and middle-level environment is dominated by positive relative vorticity with magnitude larger, but comparable, to the Coriolis parameter at this latitude ($\sim 5 \times 10^{-5}$ s^{-1}). At large radius in the upper levels, there is anticyclonic outflow.

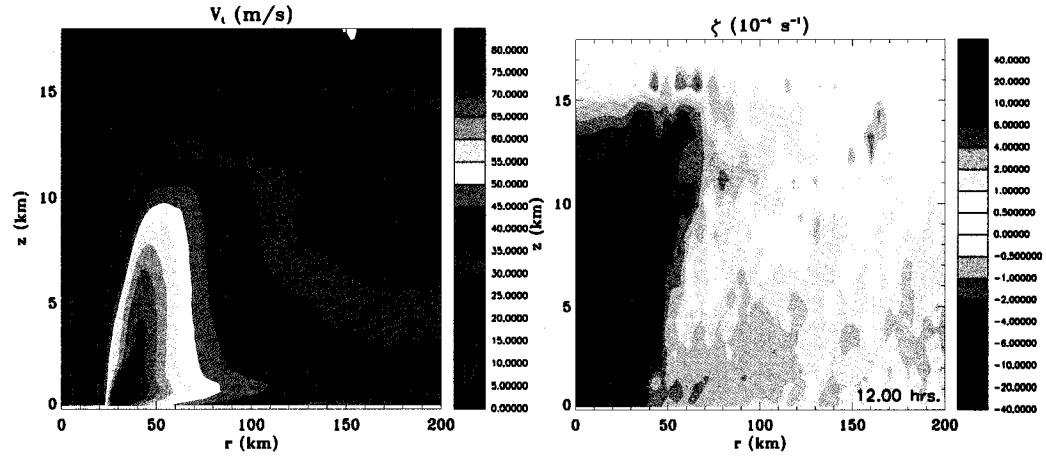

Figure 3.8: Azimuthal mean tangential wind (left) and mean relative vorticity (right) for the control simulation at Hour 12.

At Hour 12, the storm is strong and highly axisymmetric. What started out as a small hurricane with a RMW of approximately 10 km with little spiral banding has turned into a significant hurricane with a RMW of nearly 30 km with large spiral bands.

Through the maturing and intensification phases of this simulated hurricane's lifetime, we have observed different periods of growth and intensification, starting with a period of weak spatial growth but intensification of the mean winds, followed by a period of gradual spatial growth with little intensification of the winds, and most recently, a period of both gradual spatial growth and gradual intensification.

This upscale expansion even without secondary eyewall cycles may not be uncommon in real hurricanes. Bell and Montgomery (2007) have also shown, using aircraft

datasets, that Hurricane Isabel (2003) underwent a growth in its RMW that does not appear to include a secondary eyewall cycle. Maclay et al. (2007) have shown, using aircraft wind datasets for storms in the Atlantic basin, that some number of steady and intensifying hurricanes in that basin increase their integrated storm-scale kinetic energy. As previously mentioned, the actual energetics and dynamics involved in the upscale expansion of the vortex is an interesting question that we pose, but will not attempt to explain in this work.

3.2.3 Secondary Eyewall Phase

At Hour 12, the control simulation has the appearance of a strong, well-organized hurricane (Figure 3.9). It possesses a nearly circular 60 to 70 km diameter eye and several significant rainbands. These rainbands have a very complex structure at this time with many fragmented areas of convection. Figure 3.9 shows that five to eight distinct bands of convection exist outside the inner core of the simulated hurricane.

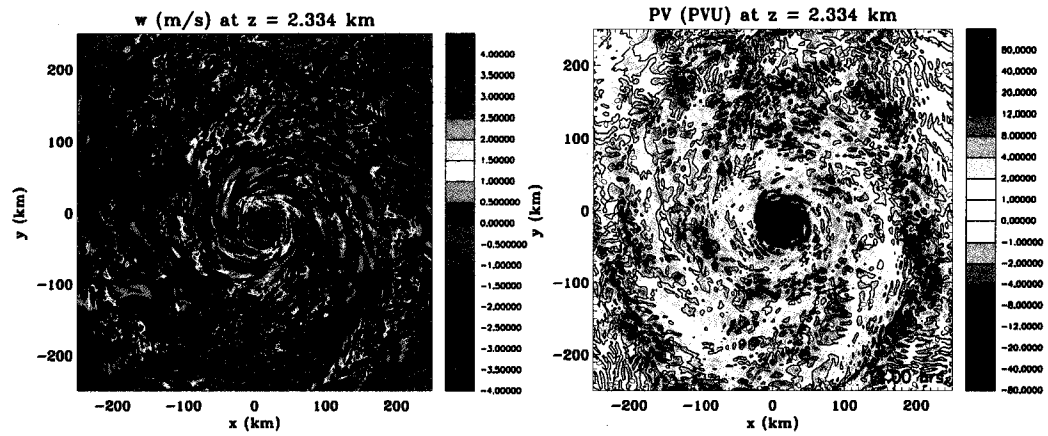

Figure 3.9: Vertical velocity (left) and potential vorticity (right) at 2.3 km height for the control simulation at Hour 12.

One important thing to note about the potential vorticity structure of these banded structures is that these convective bands are dominated by large values of PV, both positive and negative. Much of this is due to convective tilting of horizontal vorticity into

vertical vorticity dipoles (e.g. Klemp, 1987; M06). This agrees well with the results from Chapter 2, which showed that the tilting term would dominate the potential vorticity and produce dipolar structures in environments with vertical shear.

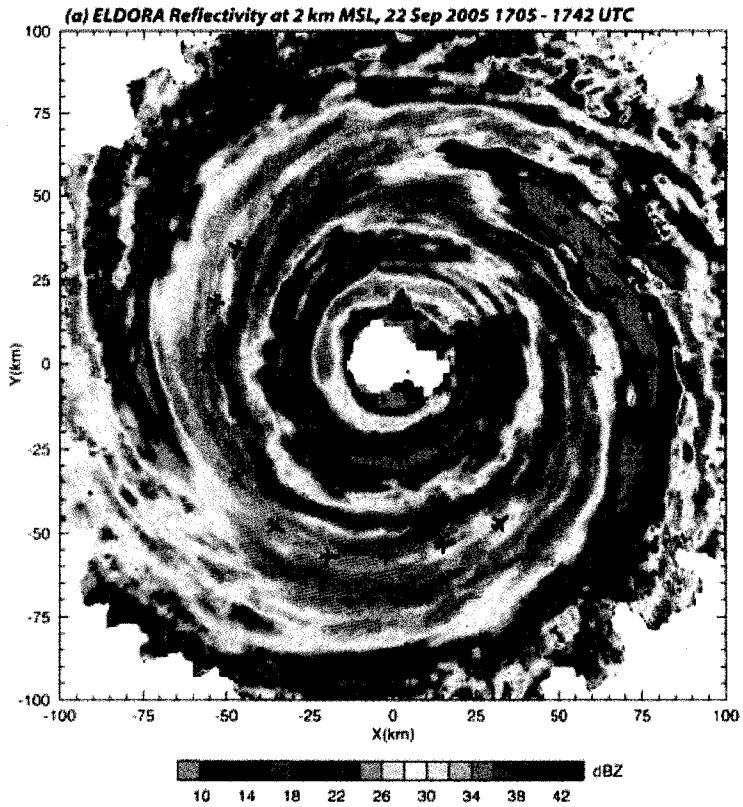

Figure 3.10: Composite radar imagery from Hurricane Rita (2005) between 1705 and 1742 UTC on 22 September from the Eldora aircraft radar. In this figure, we see the finer details of the convective elements in the outer core of the hurricane. Airplane icons trace the route of the aircraft during the flight. Figure courtesy of Michael Bell.

These dipoles have horizontal scales on the order of 10-20 km. These scales are not out of line with current observational data, which shows that updrafts in the outer core regions of the hurricane are small in scale. As evidence of this, Figure 3.10 shows a composite radar image from Hurricane Rita (2005) on 22 September, toward the end of its secondary eyewall cycle. Around the secondary eyewall, there is a lot of fine details in the reflectivity data. The horizontal scales of some of the local maxima are on the order

of 5-10 km. Thus, we feel confident that our model simulation convection has realistic scales and strength.

As time progresses, though, the shorter bands begin to merge into two coherent spiral bands (Figure 3.11). At Hour 15.5, there is a evidence of a contiguous spiral band from 30 to 40 km north of the eye spiralling out one and a half revolutions around the core to a distance of 200 km from the southeastern eyewall. A smaller band stretching from 160 to 200 km from the eyewall in an arc from southwest to northwest accompanies the longer band.

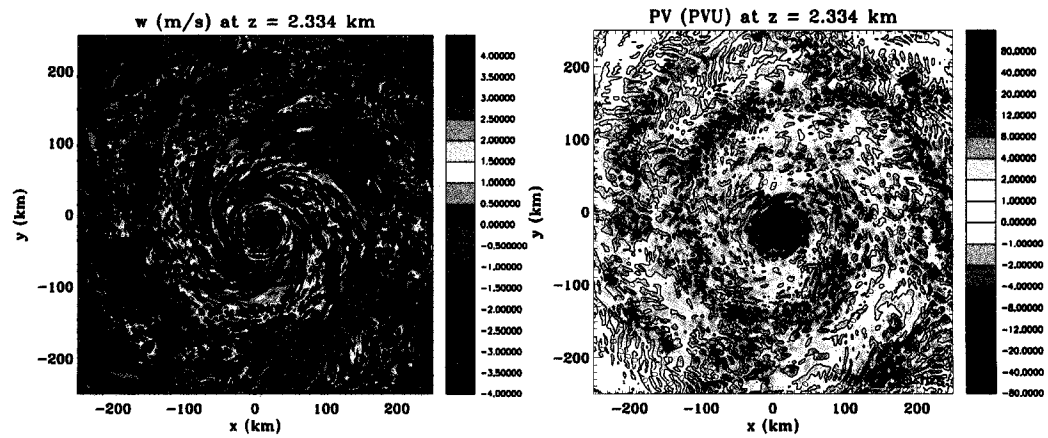

Figure 3.11: Vertical velocity (left) and potential vorticity (right) at 2.3 km height for the control simulation at Hour 15.5.

These banding features continue to interact with each other, though rarely remaining as distinct as they were at Hour 15.5 (Figure 3.12).

By Hour 18, there are nearly consecutive bands of convection outside the primary eyewall from the western side at 120 km radius to the southern side at around 80 km radius with an adjacent band of convection from the southeastern side at 140 km radius to the northern side at 80 km radius. Over the next couple hours, these two main bands remain coherent and rotate around the main eyewall (Figure 3.13). Following the band that starts to the northeast of the eyewall around to the southwest between Hours 18 and 21, we calculate that its angular phase speed during this time is approximately

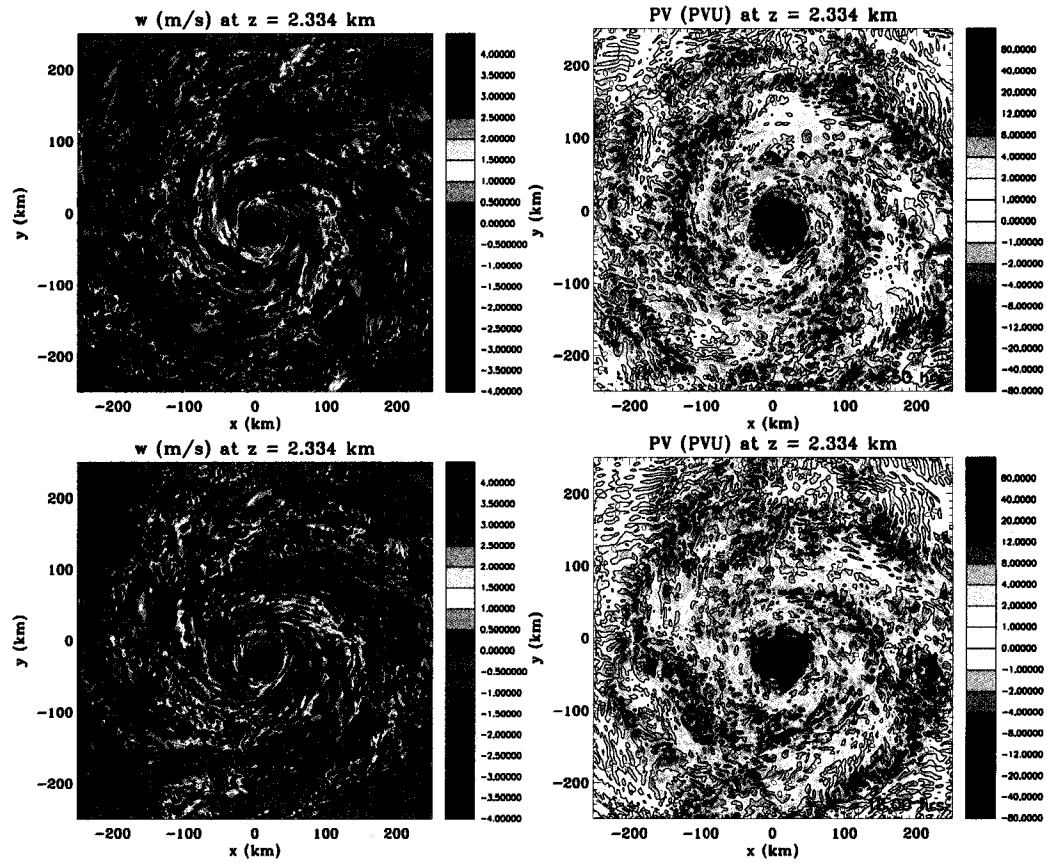

Figure 3.12: Vertical velocity (left column) and potential vorticity (right column) at 2.3 km height for the control simulation at Hour 16.5 (top row) and at Hour 18 (bottom row).

2.85×10^{-4} s^{-1}, which is about 70% of the local rotation rate of the mean wind at that level and radius.

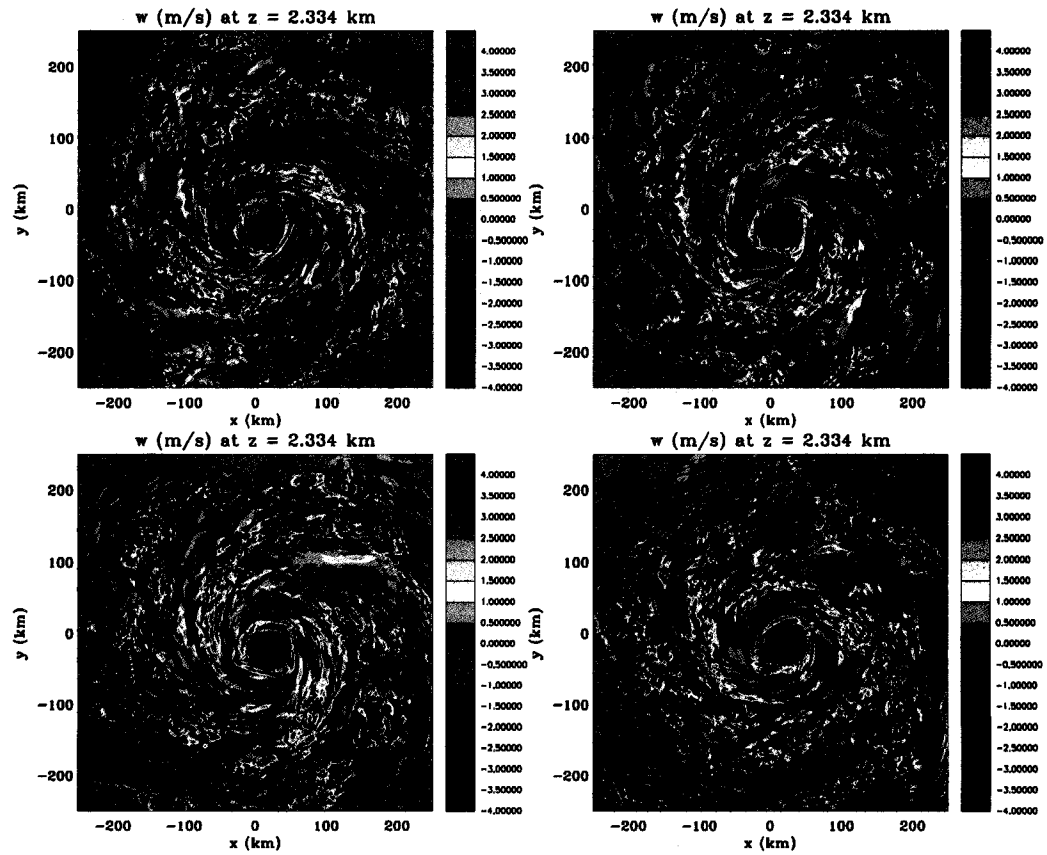

Figure 3.13: Vertical velocity at 2.3 km height for the control simulation at Hours 18 (top left), 19 (top right), 20 (bottom left), and 21 (bottom right).

This reduced angular velocity with respect to the mean wind is indicative of vortex Rossby waves (e.g. Montgomery and Kallenbach, 1997). However, this is noted merely as circumstantial evidence that the band may be dominated by the vortex Rossby wave phenomena, not as proof. Further examination of this idea is defered to future work, although previous authors (e.g. Chen and Yau, 2001; Franklin et al., 2006) have shown that these convective banding features frequently behave like vortex Rossby waves.

During Hours 18 to 21 (Figure 3.13), though, we note that the two bands not only rotate around the primary eyewall, but begin to elongate. This process looks similar to

the process of axisymmetrization of vorticity elements around a strong central vortex (e.g. Montgomery and Kallenbach, 1997; Kuo et al., 2004). By Hour 21, the tails of each band have begun to overlap the leading edge of the other band, forming what appears to be a nearly complete secondary eyewall with two gaps (northwest and southeast).

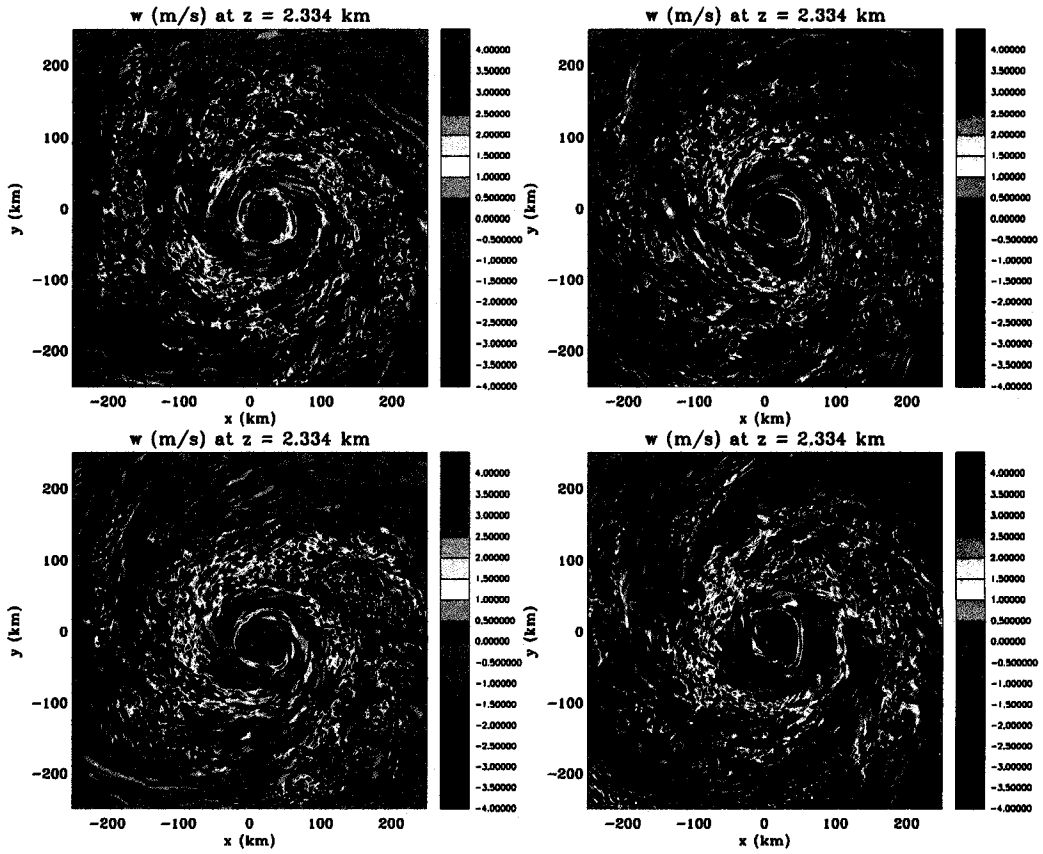

Figure 3.14: Vertical velocity at 2.3 km height for the control simulation at Hours 22 (top left), 23 (top right), 24 (bottom left), and 25 (bottom right).

This convective feature fills its gaps over the next couple hours (Figure 3.14). Vigorous convection forms in the gaps, creating the classical ring of convection that is the secondary eyewall around the inner eyewall. By Hours 24 to 25, the secondary eyewall appears to be complete and mature. These two vigorously convecting eyewalls are readily evident at this time, even though comparison of the magnitudes of the vertical velocity

in the inner eyewall at this level at Hours 12 and 24 (cf. Figures 3.9 and 3.14) clearly shows that the inner eyewall convection is not rising as strongly as it had been.

This observation agrees with the secondary eyewall replacement theory of Shapiro and Willoughby (1982). In this theory, one of the implications of the maturation of the outer eyewall is that it preempts the warm, moist inflow destined for the primary eyewall to feed its own convection. Without its source of energy (the warm, moist low-level air) and with the secondary circulation of the outer eyewall forcing subsidence in its vicinity, the primary eyewall begins to decay. We can see evidence of this process in the azimuthal mean radial wind profiles in Figure 3.15.

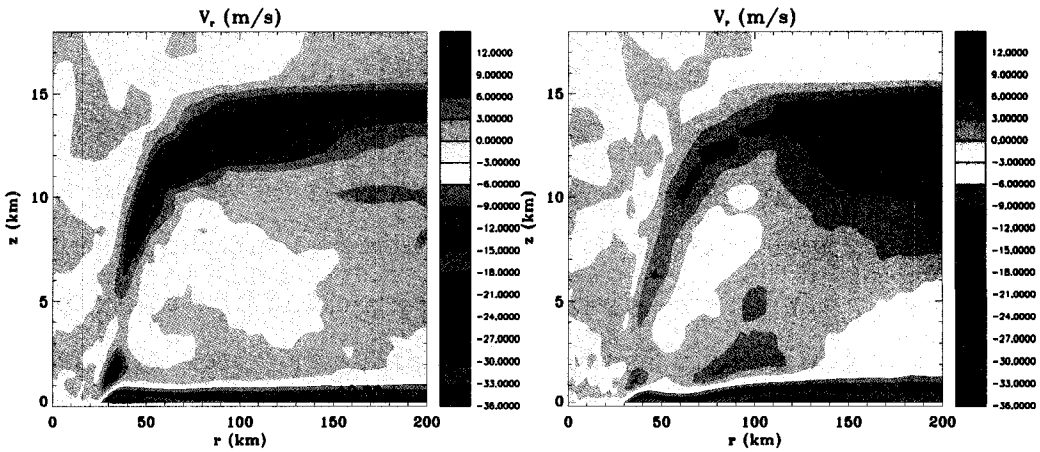

Figure 3.15: Azimuthal mean radial wind profiles at Hours 12 (left) and 22 (right).

The change in the radial inflow in the boundary layer is clearly evident in Figure 3.15. At Hour 12, the mean radial inflow was 12 m s^{-1} or higher through the boundary layer (below 1 km height), maximizing to 25 to 30 m s^{-1} right outside the eyewall at 35 km radius. By Hour 22, though, much of the inflow is concentrated outside of the inner eyewall. A small tongue of strong inflow (> 10 m s^{-1}) still exists under the inner eyewall updraft, but its depth and magnitude is significantly less than what it had been ten hours previous. Thus, it appears that the outer eyewall formation is starving the inner eyewall of its vital inflow.

From this point on, the inner eyewall collapses slowly. Figure 3.16 shows the vertical velocity at the same level as the previous plots and clearly demonstrates that the inner eyewall convection almost completely disappears in six to nine hours. By Hour 30, there are a few small remnants of convection in the inner eyewall while the outer eyewall convection is vigorous and encircles the inner completely. By Hour 36, there is little indication that the inner eyewall convectively exists.

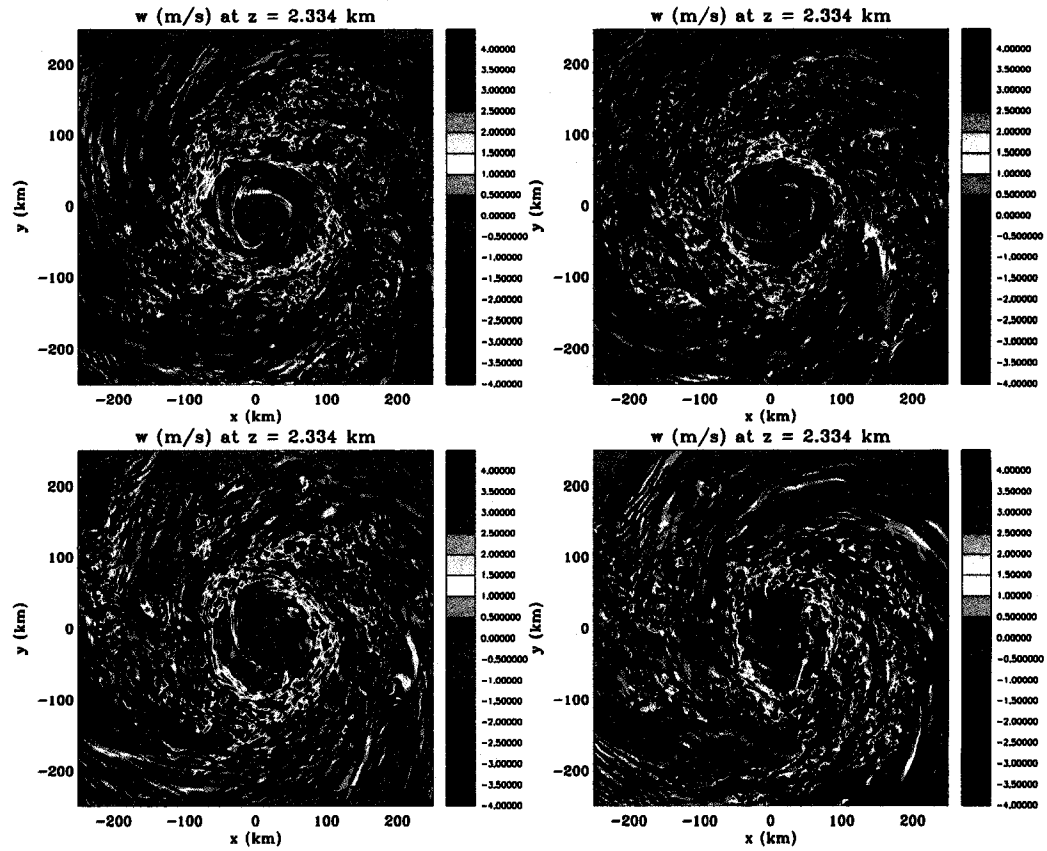

Figure 3.16: Vertical velocity at 2.3 km height for the control simulation at Hours 27 (top left), 30 (top right), 33 (bottom left), and 36 (bottom right).

From first detection near Hours 15-18 to the loss of convection associated with the inner eyewall near Hour 33-36, the entire cycle appears to take approximately 18 hours. This value is in strong agreement with observations of secondary eyewall cycles

completing in 12 to 36 hours (Willoughby, 1990), which leads us to believe that the processes that form and dissipate concentric eyewalls in real hurricanes may be well-simulated by the RAMS. With this excellent model dataset, then, we feel confident in isolating and describing the secondary eyewall formation process.

Some concern may be generated by the elliptical nature of the secondary eyewall. However, elliptical secondary eyewalls are not uncommon. Figure 3.17 shows an example of this phenomenon from radar composite data from a flight into Hurricane Ivan (2004) in the Atlantic. This feature has also been observed in Hurricane Gilbert (1988) in the Atlantic by Dodge et al. (1999). We believe that other major tropical cyclones have produced elliptical secondary eyewalls and that they are just part of the natural variability of the phenomenon.

Figure 3.17: Composite radar data from aircraft reconnaisonce into Hurricane Ivan (2004) on 12 September. Two eyewalls are evident. The outer eyewall is elliptical in shape.

Chapter 4

THEORY

4.1 Prior Formation Hypotheses

In the introduction, previous hypotheses on the formation of secondary eyewalls were briefly summarized. Using the datasets for our two numerical hurricane experiments, we now more thoroughly describe and examine these prior hypotheses. In particular we focus on those ideas that may explain the secondary eyewall formations that happen in the current simulations.

Table 4.1 summarizes the prevailing published hypotheses for secondary eyewall formation and gives a short description as to the relevance of the hypothesis with respect to our modeled storms. Some of these works do not focus on secondary eyewall formation as their primary topic. Additionally, other works have suggested other authors' ideas as potential formation processes, most notably Willoughby et al. (1982) and Willoughby (1990). As we apply these hypotheses to our simulated hurricanes, we quickly dismiss a number of them as unnecessary for the formation of the secondary eyewall.

Hawkins (1983), for example, speculated that secondary eyewalls might form due to topographic influences on the vortex circulation. However, since our simulations include no topography, we conclude that topography is not required for secondary eyewall formation.

Furthermore, note that Willoughby's (1979) hypothesized resonance between the local inertia period and asymmetric friction due to storm motion is not a requirement for secondary eyewall formation. Neither of the simulated storms drifts more than 60

km from the center of the model domain until well after the secondary eyewall cycle has completed.

The two Molinari conjectures (Molinari and Skubis, 1985; Molinari and Vallaro, 1989), and to a lesser extent the Nong and Emanuel (2003) conjecture, argued for the importance of synoptic-scale influences on eyewall formation. Molinari and Skubis (1985) studied the formation of the primary eyewall and the rapid intensification of a tropical cyclone due to the interaction between the main vortex and a low-level wind surge. Molinari and Vallaro (1989) examined the intensification of a tropical cyclone vortex by its interaction with an upper-level potential vorticity anomaly. Both of these studies focus on the formation of the primary eyewall in a developing hurricane, not of a secondary eyewall in a mature tropical cyclone. In spite of this, we believe that these eyewall formation ideas have the potential to be illustrative and important in the secondary eyewall formation problem. Additionally, Nong and Emanuel (2003) hypothesize that sustained momentum fluxes coupled with a positive feedback mechanism can produce secondary eyewalls in their axisymmetric hurricane model. In their case, wind-induced surface heat exchange, or WISHE, is the feedback mechanism invoked. The momentum fluxes were imagined to be synoptic-scale intrusions onto the primary hurricane vortex (e.g. Molinari and Skubis, 1985; Molinari and Vallaro, 1989).

However, these synoptic-scale influence hypotheses are not necessary conditions for secondary eyewall formation in our simulations. We do not specify any synoptic-scale forcings in the simulation, nor do we find evidence that any form in the environment of the modeled hurricane during the simulation. However, this does not negate the potential influence of positive feedbacks like WISHE (e.g. Nong and Emanuel, 2003) on secondary eyewall formation.

The simulations presented here have been purposely formulated to omit some of these previously conjectured processes. The simulations suggest intrinsic processes operating within the hurricane act to form secondary eyewalls without processes conjectured

by the discarded hypotheses in Table 4.1. We cannot reject the possibility, however, that these ideas may have relevance in specific cases. Instead, we now focus our attention on the hypothesized intrinsic mechanisms for secondary eyewall formation.

The Zipser (1977) paper examined the structure of squall lines in the tropical Atlantic and discovered the mesohigh and mesolow features that are commonly found in mid-latitude squall lines. Later papers, including Barnes et al. (1983), expanded on these ideas, suggesting that hurricane rainbands may have similar features. These mesoscale downdraft features could force additional convection by disrupting the low-level inflow into the primary eyewall and forcing a new eyewall. This particular idea was proposed in Willougby et al. (1982) as a potential formation mechanism for secondary eyewalls. However, since the Willoughby et al. (1982) work includes a review of a number of potential formation hypotheses, we will refer to this hypothesis as the downdraft hypothesis.

To test this hypothesis, we examine Figure 4.1, which shows the azimuthal mean vertical velocity at Hour 10, prior to the secondary eyewall formation. We note that there are gentle downdrafts on the order of 25 to 50 cm s^{-1} in the azimuthal mean and 2 to 4 m s^{-1} locally outside the core of the storm. While there does appear to be some evidence that a small number of simulated updrafts are forced by previous downdrafts, these are in the minority of the updrafts diagnosed in the formation region and period (not shown). Given the lack of sufficient evidence supporting the downdraft hypothesis, we hereafter neglect it in our model-based examinations of secondary eyewall formation.

Kuo et al. studied the two-dimensional, non-divergent vortex dynamic interactions between two or more vorticity patches of varying sizes, separations, and intensities (Kuo et al., 2004; Kuo et al., 2007). These works have shown that concentric vorticity features can be formed by the axisymmetrization of weaker patches of vorticity around a strong core of vorticity, usually with the requirement that the weaker patches be suitably distant from the core and with vorticity amplitudes at least four to six times less intense than the core vorticity. Their numerous numerical experiments highlight the robustness of this

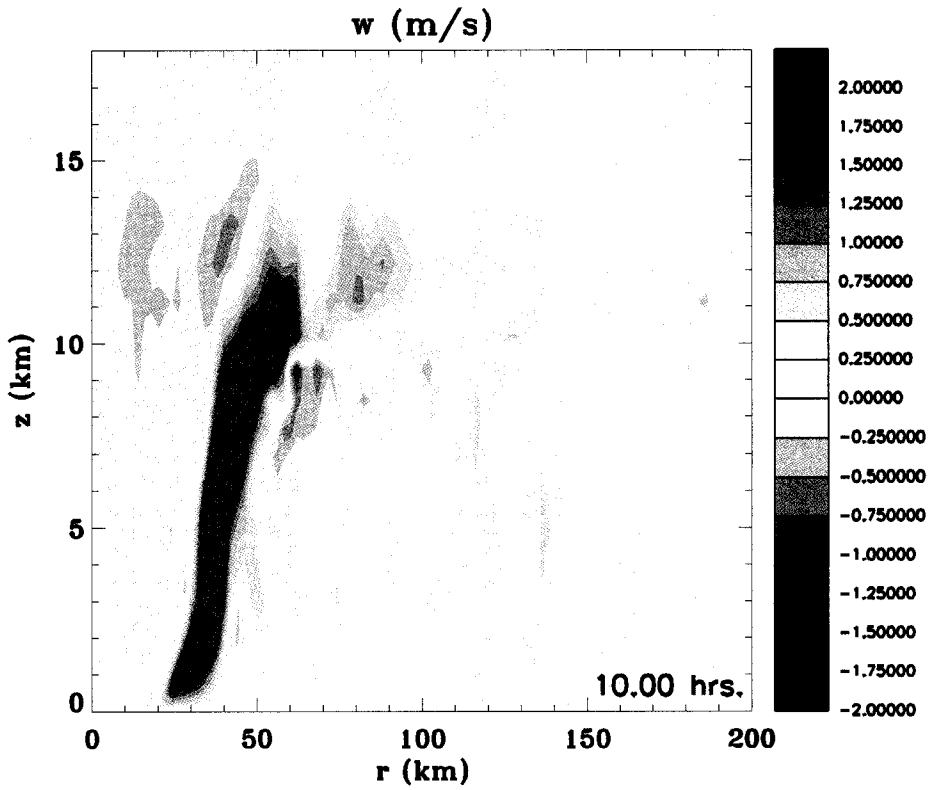

Figure 4.1: Azimuthal mean vertical velocity at Hour 10.

result. Other works have proposed variants of the axisymmetrization mechanism to explain secondary eyewall formation. In addition to the axisymmetrization of convectively generated vorticity, dynamical regions like stagnation radii or critical radii have been hypothesized as focal points for the absorption of vortex Rossby wave activity within the vortex (e.g. Montgomery and Kallenbach, 1997; Camp and Montgomery, 2001; Terwey and Montgomery, 2003). The question as to whether sheared vortex Rossby waves or inertia-gravity waves dominate the advective dynamics outside the hurricane core has been recently answered using an objective method of identification of the principal asymmetric wave structures (Brunet, 1994; Chen et al., 2003). This calculation, termed the Empirical Normal Mode Method, has been utilized in high-resolution hurricane simula-

tions to show that the sheared spiral bands outside the primary eyewall are composed primarily of sheared vortex Rossby waves (Chen and Yau, 2001; Chen et al., 2003).

Whereas the above dynamical works have contributed fundamental understanding of vorticity axisymmetrization in hurricane-like vortices, these studies have not yet addressed two aspects of realistic hurricane flows that can arrest vortex axisymmetrization processes. In full-physics numerical simulations like ours, for example, convectively generated vorticity anomalies outside the primary eyewall are of comparable magnitude to the mean vorticity of the eyewall region. These large vorticity amplitudes are not unexpected since convective updrafts tilt the ample horizontal vorticity of the mean hurricane wind field into the vertical, leading to strong dipolar vorticity structures (e.g. M06; Franklin et al., 2006). Such localized vorticity anomalies possess small horizontal scales in comparison to the characteristic diameter of the hurricane eyewall region. The large amplitudes and small scales of the convectively generated vorticity anomalies can act to resist axisymmetrization by the larger-scale hurricane vortex in many cases (e.g. Dritschel and Waugh, 1992; Enagonio and Montgomery, 2001).

In a complimentary study, Rozoff et al. (2006, hereafter R06) suggested that the non-convective region between the primary and secondary eyewalls (often called the moat) might be strongly influenced by the large vorticity of the hurricane core. R06 derived the timescale associated with the straining portion of the flow, denoted here as τ_{fil}, and, for a variety of candidate mean vortex profiles, compared this kinematic timescale to a suitable convective lifetime. R06 hypothesized that the moat might not just be dominated by subsidence, which tends to produce a "cap" to convective processes, but that this strong filamentation process will tend to shear apart nascent convective cells before they can mature and organize.

The moat and secondary eyewalls are related in that one cannot be collocated with the other. The moat is defined by the lack of deep convection, while the secondary eyewall is defined by the presence of deep convection. We therefore suspect a relationship between

the filamentation timescale and secondary eyewall formation in which a secondary eyewall may only form where τ_{fil} is large enough to allow nascent convection to mature and organize.

4.2 Quasi Two-Dimensional Turbulence Theory

Because of the implied role of convection in the secondary eyewall formation process, we now focus on the individual convective cells in the environment of the modeled hurricane. Inspection of the model datasets indicates that these cells have a substantially smaller horizontal spatial scale than the inner core of the hurricane. Considering the potential role of small-scale processes in a rapidly rotating vortex like a hurricane, little inspiration is needed to hypothesize that the convection may be feeding energy into the larger-scale vortex system in a turbulent manner (cf. Montgomery and Enagonio, 1998; McWilliams, 2006). The crux of this turbulent characterization of the convection is then determining the fate of this turbulent energy forced by the convective motions, determining where in the hurricane vortex this convective energy is input, and explaining the factors influencing the frequency and strength of this convection.

Since turbulent flows are influenced strongly by their dimensionality and intrinsic parameters, it is natural to inquire as to which turbulence theory is most appropriate to build upon for the secondary eyewall problem. Initially, we might expect that a three-dimensional framework would be most appropriate. However, due to their rapidly rotating core and small aspect ratio on the system scale, mature hurricanes evolve largely in a quasi two-dimensional manner (Shapiro and Montgomery, 1993; Montgomery and Shapiro, 1995; Montgomery and Kallenbach, 1997; Braun et al., 2006; Schecter and Montgomery, 2007). Charney (1971) demonstrated that, in quasi two-dimensional systems, idealized two-dimensional turbulence theories hold sufficiently well to describe the physics of turbulent flows. On the basis of these aforementioned works, we henceforth assume that the mesoscale circulations generated by the convection in the mature hurricane

are constrained by quasi two-dimensional balanced dynamics and that two-dimensional turbulence theories are the most appropriate framework in which to investigate the fate of the convective energy.

A cursory examination of two-dimensional turbulence theories (e.g. Kraichnan, 1967; Frisch, 1996; McWilliams, 2006) suggests that energy generated by the convection will tend to cascade upscale while the enstrophy will tend to cascade downscale. The exact nature of this cascade, though, is subject to other intrinsic parameters of the background state.

On an f-plane or other constant vorticity background flow, McWilliams (1984) demonstrated that idealized two-dimensional turbulence will self-organize into a single cyclone-anticyclone pair. The major process involved in this result is the merger of like-signed vorticity perturbations, a feature fundamental to two-dimensional flows.

Once the dynamics are constrained by the background of a β-plane or sphere, the end state of two-dimensional turbulence changes. Rhines (1975) investigated two-dimensional turbulence on a β-plane and concluded that the existence of a background vorticity gradient changes a few significant aspects of the turbulent cascade. First, the flow field, at large scales, "feels" the background vorticity gradient, called the β effect, and forces the turbulence to become anisotropic in nature with a preference for zonally elongated eddies over meridionally elongated ones. This change in the flow's character is summarized by the Rhines scale, an eddy length scale above which the turbulent energy cascade is halted. The Rhines scale is denoted, in standard length scales, as $L_\beta \propto \sqrt{u_{rms}/\beta}$. The root-mean-squared velocity, u_{rms}, is the characteristic velocity associated with the eddies. Additionally, Rhines showed that the zonal flow is stabilized in two-dimensional turbulence on a β-plane. The implication of this is that, for flows with strong background rotation, turbulence would force the fluid toward zonal flow patterns.

Based on this theory, other works have verified this implication, showing that zonal jets are the natural ending state for two-dimensional turbulence on the β-plane and

sphere (e.g. Williams, 1978; Vallis and Maltrud, 1993; Huang and Robinson, 1998). While the exact nature of the dynamics involved in the energy and enstrophy cascades has been a subject of debate, the final result has been shown to be robust. The existence of a persistent background vorticity gradient forces eddies into zonal jets with widths on the order of the Rhines length.

Thinking about the azimuthal mean hurricane as the background state, we can envision the convection as the perturbation energy input into the system. We have established that a strong hurricane vortex is governed by quasi two-dimensional dynamics. Thus, the overriding dynamical framework in which the turbulent convective energy and vorticity depends strongly on the vorticity structure of the mean hurricane profile. By compositing observations from many mature hurricanes, Mallen et al. (2005) showed that fully developed hurricanes typically have a "skirt" of vorticity outside the main core in the low levels. This "skirt" is where a relatively weak but persistently nonzero radial gradient exists in the azimuthal mean vorticity.

The skirt region of a hurricane vortex therefore has an effective β: the spatial change of the background vorticity of a system. In the hurricane, β generally refers to the radial derivative of the mean vorticity. The existence of this skirt with β implies that convectively generated perturbations are expected to form azimuthal mean jets in this region, if these two-dimensional turbulence theories are valid in the rapidly rotating hurricane vortex. It is from this extension of theory that we propose the following secondary eyewall formation hypothesis.

4.3 Hypothesis

Figure 4.2 is a conceptual drawing of our secondary eyewall formation theory. To begin with, we envision that the storm includes a large skirt of azimuthal mean vertical vorticity with a persistently negative radial gradient in the lower troposphere spanning the inflow layer. This is a general structural feature of mature tropical cyclones, as

Mallen et al. (2005) have shown in their composite study of hurricane wind profiles. This skirt of vorticity gently decays to near-zero values as one moves outward toward the far-field environment. Within the skirt region, there is a non-trivial effective β, prompting the nomenclature of "β-skirt" for this area.

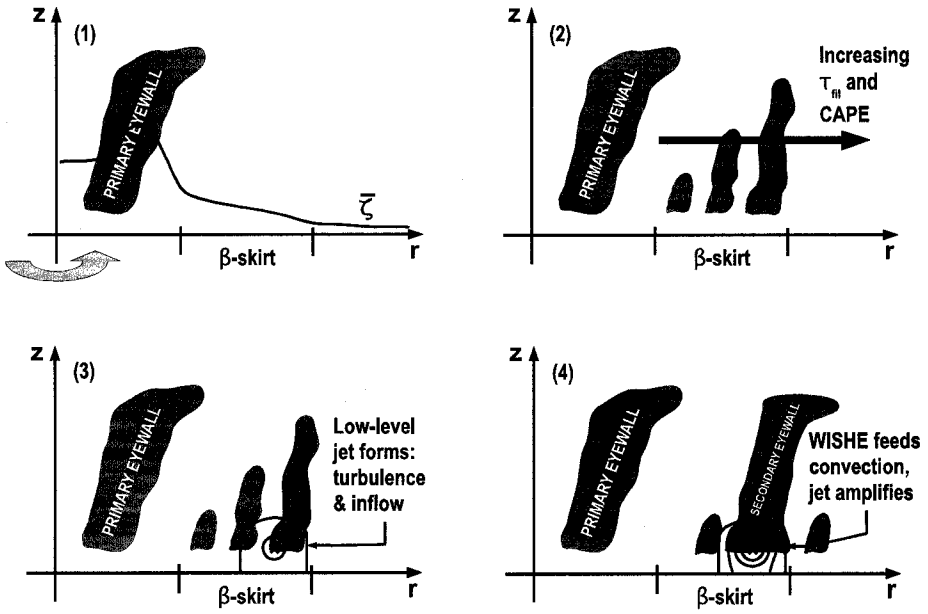

Figure 4.2: Proposed conceptual model of the nonlinear β-skirt axisymmetrization secondary eyewall formation mechanism.

Within the β-skirt, sporadic convection will form. However, this convection is constrained by many factors.

It is readily verified that for realistic hurricane-like wind profiles the mean filamentation timescale, τ_{fil}, increases radially outward away from the eyewall. If we assume that, outside the eyewall, the mean tangential winds decay like $\bar{v}_t = \bar{v}_0(r/r_0)^\alpha$ where α is between 0 and -1 and subscript 0 denotes the values at the RMW, we can calculate the mean $\tau_{fil} = (\sqrt{-(\bar{v}_t/r)(\partial\bar{v}_t/\partial r)})^{-1}$. This reduces to $\tau_{fil} = \frac{r_0^\alpha}{v_0\sqrt{-\alpha}} \cdot r^{1-\alpha}$. Since $1-\alpha > 1$, τ_{fil} increases radially outward.

Additionally, observations have shown that, in major hurricanes, convective available potential energy (CAPE) increases radially outward from the core, often reaching an equilibrium value just outside the primary eyewall (e.g. Gray and Shea, 1973; Frank, 1977). These factors together help dictate where deep convection could readily occur. If an area of convective potential exists within the β-skirt (e.g. $\tau_{fil} > 30$ minutes, sufficient CAPE, low convective inhibition), deep convection should be able to occur regularly, given that this environment has sufficient forcing mechanisms. (Outside the core of a mature hurricane, this is rarely an obstacle for convection since many forcing mechanisms exist in this region, including cold pools from previous convection, gravity-inertia waves, and vortex Rossby waves.)

This convection then acts as a source of perturbation kinetic energy and vorticity in the β-skirt. Given that the horizontal scale of these individual convective cells (typically on the order of 10 km) is small compared to the radial extent of the β-skirt (typically 50 to 100 km radius), the eddy kinetic energy will tend to be fed into the system-scale vortex at small scales.

As we might anticipate from two-dimensional β-plane turbulence theory (Vallis and Maltrud 1993), the energy from these perturbations will be directed upscale in an anisotropic manner as quasi-zonal jets ("axisymmetrized" into the sheared mean flow) whose widths scale as the beta length scale: $\sqrt{u_{rms}/\beta}$, where u_{rms} is the root-mean-squared velocity perturbation and β is the radial derivative of the potential vorticity of the mean hurricane vortex.

These turbulence theories alone, though, do not ensure that the axisymmetrization process will ensue. As previously discussed, the vorticity perturbations forced by the convection are typically as strong as the mean vorticity in the core of the hurricane. Nonlinear numerical experiments of strong vorticity rings around a core of similar strength vorticity have shown the tendency of these intense rings to "roll up" into "vortex

crystals", or coherent vorticies in a polygonal pattern (Kossin et al. 2000). Other studies have shown that when the vorticity gradient becomes sufficiently strong compared to the local shear, the linear axisymmetrization dynamics remain uniformly valid and are effectively stabilized against the nonlinear tendency to arrest this upscale cascade (e.g. Brunet and Montgomery 2002, Montgomery and Brunet 2002). Such considerations suggest that the role of the β-skirt is to constrain the asymmetric flow within the β-skirt region to evolve approximately as quasi-linear axisymmetrization dynamics would predict, converting perturbation vorticity and kinetic energy from sporadic deep convection into the azimuthal mean flow. After sufficient time is given for these processes to transfer perturbation vorticity and energy into the mean swirling winds, sporadic deep convection will tend to form a substantial low-level jet in the β-skirt.

The approximate limit where linear axisymmetrization theory remains a useful first approximation is dependent on the vortex beta Rossby number (e.g. Möller and Montgomery, 2000; Montgomery and Brunet, 2002). The vortex beta Rossby number is defined as $[u_{rms} \ / \ (\mathrm{L}^2\beta)]$, where L is the eddy length scale. When this number is less than unity, linear dynamics generally serves as a valid first approximation. Since our eddy velocity scale is essentially linked with the horizontal velocity scale associated with the convection, we see that when the beta scale-length is on the same order of magnitude as the convective scale-length, linear axisymmetrization dynamics will tend to prevail within the β-skirt. Thus, for our hypothesis to remain valid, we require sufficient effective β so that the convective disturbances will tend to be axisymmetrized.

This hypothesis is similar to the other internal dynamical formation hypotheses in that perturbations are dynamically forced into the azimuthal mean profile of the hurricane. However, in this idea, the convection is modeled not as an initial value of vorticity or energy, but instead as a continual and stochastic forcing into the system. The hypothesis also highlights the importance of the β-skirt in helping stabilize the

axisymmetrization tendency of the convective forcing, which in turn induces localized jets in the lower troposphere.

Additionally, in this region, the increased convective activity forces additional mean inflow from the environment of the hurricane. This inflow feeds warm, moist air at low levels that fuels the convection. This increased inflow and convection will show up as a new branch of the secondary circulation. This inflow will converge angular momentum and vorticity, particularly the increased mean vorticity in the β-skirt, and help spin up a mean low-level jet.

The combined effects of the axisymmetrization by the β-skirt of the turbulent kinetic energy forced by the convection as well as the increased low-level inflow from the convection generates the low-level jet. Once this low-level jet forms, it can intensify by coupling with the boundary layer through a wind-induced moisture feedback process such as WISHE (Nong and Emanuel, 2003) once it reaches a critical threshold. In the WISHE model, the increased winds increase the amount of latent and sensible heat fluxes from the ocean surface, which makes the low-level air more convectively favorable. This air begins to form additional strong convective updrafts near or within the azimuthal mean jet, creating a positive feedback loop. This amplifying ring of convection becomes the secondary eyewall.

The positive feedback of the WISHE requires the jet to form in the low-levels of the hurricane. This implies that the β-skirt needs to exist at the low-levels in our hypothesis also. While the β-skirt can potentially extend up above the boundary layer, the feedback can only occur if the jet forms in the boundary layer.

A useful aspect of this hypothesis is that it can be tested and used operationally with current hurricane observational methods. Accurate azimuthal mean wind profiles can be computed from dropsonde and aircraft measurements. Radial wind profiles can be examined for the existence of a sufficient low-level β-skirt region with large filamentation timescales. Dropsondes can also be used to compute the convective potential in that region, ensuring that convective inhibition is low enough to allow for frequent convection.

Secondary Eyewall Formation Hypotheses

Authors	Hypothesis Summary	Model Comments	Type
Willoughby et al. (1982) expanding the squall line work of Zipser (1977)	Downdrafts from the primary eyewall or an attendant rainband force a ring of convective updrafts	Few downdraft-forced updrafts during this time in the simulations	O
Willoughby (1979)	Internal resonance - inertia period and asymmetric friction due to storm motion	No systematic storm motion in the simulated storms	A
Hawkins (1983)	Topographic effects	No topographic forcing in the simulations	O
Willoughby et al. (1984)	Ice microphysics	No-ice model produces secondary eyewall	A
Molinari, Skubis (1985); Molinari, Vallaro (1989)	Synoptic-scale forcings (e.g. low-level wind surges, upper-level momentum fluxes)	No synoptic-scale forcings in the simulations	O
Montgomery, Kallenbach (1997); Camp, Montgomery (2001); Terwey, Montgomery (2003)	Internal dynamics: axisymmetrization via sheared vortex Rossby wave processes; wave energy collection near stagnation & critical radii	Possible explanation	N
Nong, Emanuel (2003)	Sustained eddy momentum fluxes; WISHE feedback	Partial explanation?	A
Kuo et al. (2004, 2007)	Axisymmetrization of positive vorticity perturbations around strong, tight core of vorticity	Possible explanation	N

Table 4.1: List of secondary eyewall formation hypotheses with summary of relevance to our modeled hurricanes. The type column refers to the type of model or observations that were the basis of the hypothesis. O stands for observationally-based; A stands for axisymmetric model; N stands for non-axisymmetric model.

Chapter 5

SECONDARY EYEWALL FORMATION

5.1 Basic Analysis

To test our proposed hypothesis, we now present evidence from our control simulation. As stated previously, we will be focusing on the formation period, defined as Hours 8 to 18.

Figure 5.1 shows calculations of effective β and τ_{fil}, using temporally averaged azimuthal mean flow quantities over a four-hour period from Hour 8 to Hour 12. Temporal averaging is used to reduce the small-scale noise from phenomena like convective processes and show the representative mean waveguide in which the perturbations evolve. Rather than using a basic definition of β as the radial derivative of vorticity, we utilize a definition that better takes into account the unique dynamical constraints of the hurricane vortex. Effective β is defined from the asymmetric balance theories of Shapiro and Montgomery (1993) and Montgomery and Kallenbach (1997) for a one-layer barotropic fluid as $\beta = -(\partial\bar{q}/\partial r)(\bar{q}/\bar{\xi})$, where $q = \vec{\zeta_a} \cdot \nabla\theta/\rho$ is Ertel's potential vorticity, $\xi = f_0 + 2v_t/r$ is the modified Coriolis parameter, v_t is the tangential velocity, and $\bar{F}$ indicates a temporal and azimuthal average of the quantity F. The negative sign on effective β is used such that the increase in potential vorticity with decreasing radius is associated with positive β. This convention allows standard β-plane and spherical thinking to be applied in regions with radially decreasing potential vorticity. For τ_{fil}, we use the azimuthal averaged version from R06, defined as $\tau_{fil} = (\sqrt{-(\bar{v_t}/r)(\partial\bar{v_t}/\partial r)})^{-1}$.

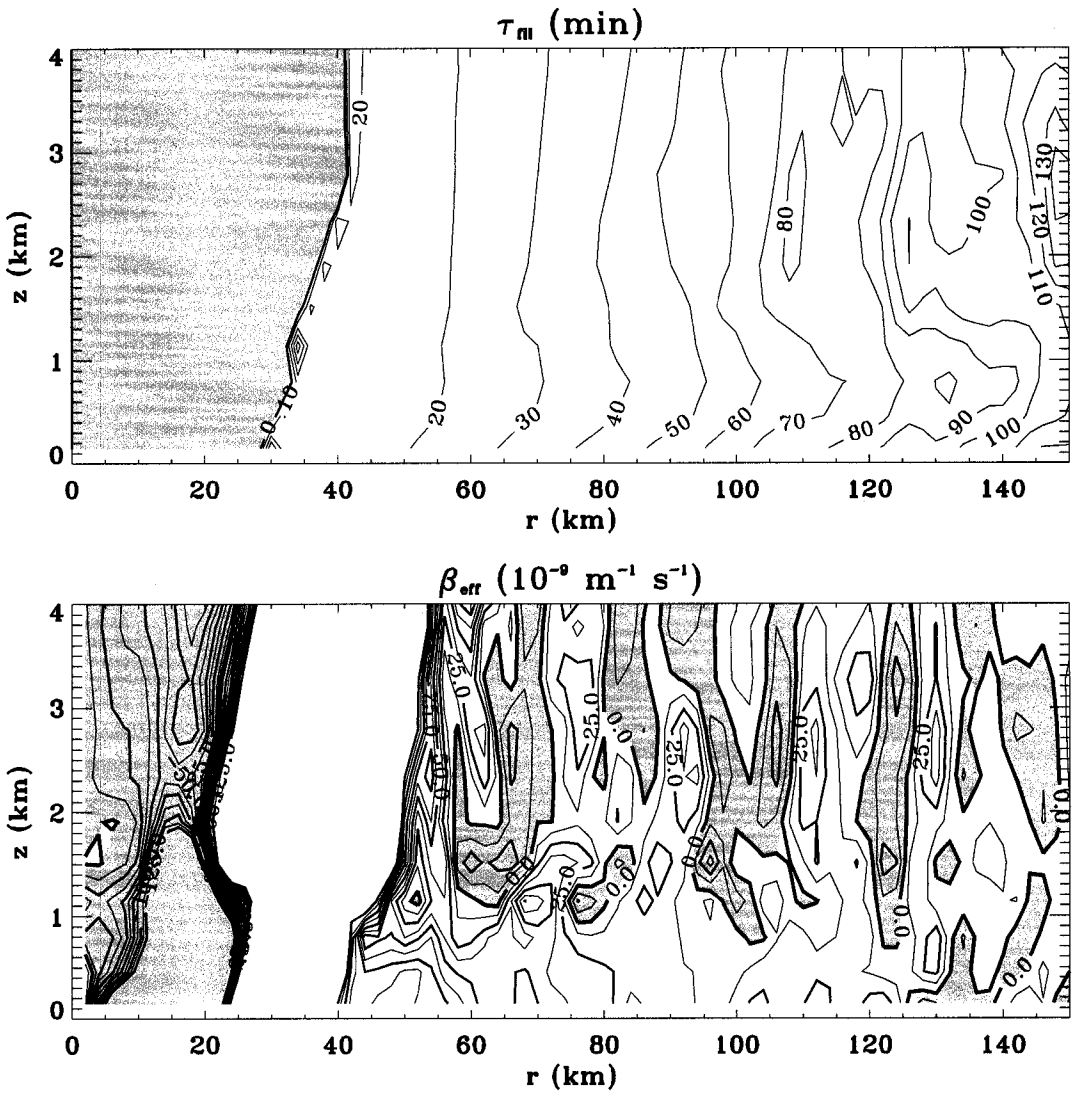

Figure 5.1: Calculations of τ_{fil} and effective β in the control simulation. This calculation uses temporally averaged azimuthal mean quantities from Hours 8 to 12. Contour intervals are 10 minutes for τ_{fil} and 12.5×10^{-9} m^{-1} s^{-1} for β. Vorticity-dominated (for τ_{fil}) and negative β regions are shaded. Only the first ten contours of each sign for β are drawn.

From Figure 5.1 we see the existence of a low-level β-skirt during these four hours. The value of β in the skirt is strictly positive below 1 km out to a radius of 125 km. Prior to Hour 0, there was little evidence of a persistent β-skirt in the lowest levels.

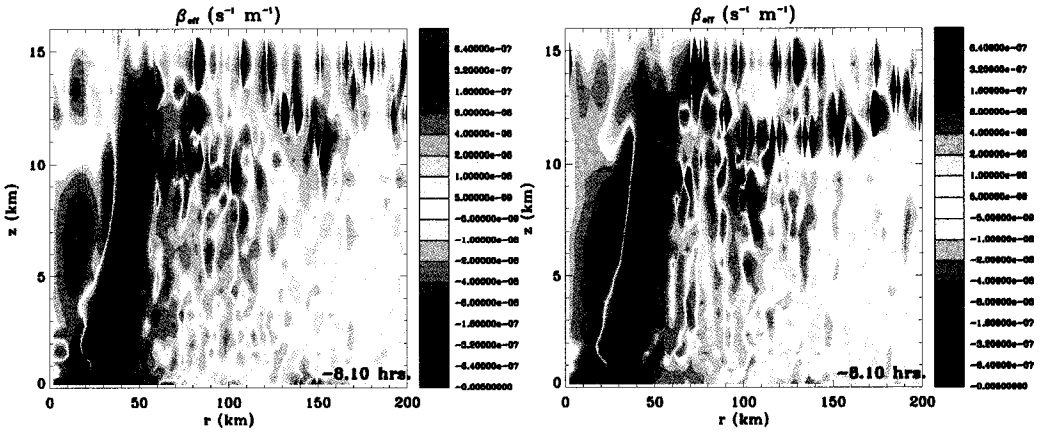

Figure 5.2: Calculation of effective β in the control simulation prior to Hour 0. This calculation uses four-hour temporally averaged azimuthal mean quantities. The calculation from Hours -24 to -20.1 is plotted in the left panel, while the right panel displays the calculated quantity from Hours -12 to -8.1.

This can be seen in Figure 5.2, which shows four-hour calculations of β for two time periods prior to Hour 0. The existence of an extensive low-level β-skirt is hard to argue until at least Hours -12 to -8, at which point it is just beginning to extend outside the region of convectively unfavorable horizontal shear. Since there was no evidence of a secondary eyewall cycle at these times, this underscores the probable role of the β-skirt in the formation of the secondary eyewall later. The processes involved in the formation of this low-level β-skirt are as of yet unknown and may provide additional insight into the dynamics of mature hurricane vortices.

Borrowing from basic β-plane turbulence theories (e.g. Vallis and Maltrud, 1993), the effective beta scale-length suggests that this skirt will tend to force jets with radial scales larger than, but with the similar magnitude as, $\sqrt{u_{rms}/\beta}$, where u_{rms} is the root-mean-squared horizontal eddy velocity perturbation. Within our β-skirt, this effective

beta scale comes out to 12 to 24 km, given that the root-mean-squared velocity perturbations are diagnosed to be 4 to 7 m s^{-1} and β is diagnosed to be 12.5 to 25×10^{-9} m^2 s^{-2} in this region. The beta time scale for this process, $1/\sqrt{\beta u_{rms}}$, is on the order of 40 to 75 minutes. If we assume that the eddy length scale is approximately 20 km, the vortex beta Rossby number, $u_{rms}/(L^2\beta)$, is estimated to be on the order of 0.36 to 1.44, suggesting that the perturbations of these scales generated in the β-skirt should be approximately governed by quasi-linear dynamics and, hence, axisymmetrized in time.

From Figure 5.1, we see that, as expected, the mean filamentation timescale increases with radius. R06 suggested that τ_{fil} greater than 30 minutes would be sufficient to allow convection to grow before the straining process disrupts the updraft. The region with τ_{fil} greater than 30 minutes stretches from 70 km radius outward. Therefore, we expect that any convection that forms during and after this period outside of 70 km radius may be potentially deep and long-lived according to the filamentation dynamics.

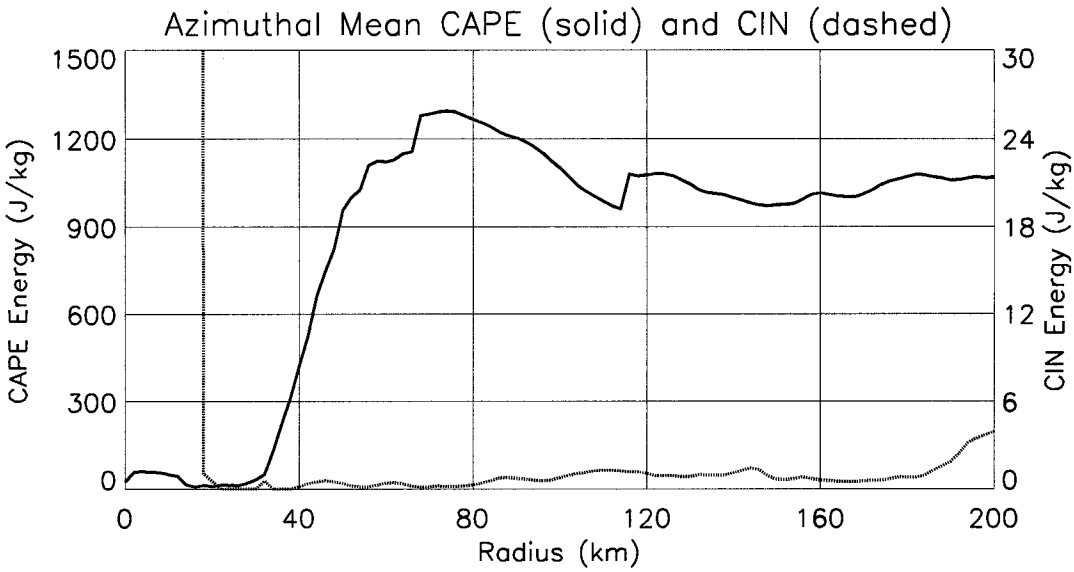

Figure 5.3: Surface-based CAPE and CIN calculations using azimuthal mean thermodynamic quantities at Hour 10.

Examining the azimuthal mean soundings for thermodynamic considerations (Figure 5.3), we also note that the mean surface-based CAPE in the region from 60 km to

200 km is 900 to 1300 J kg^{-1} with very low convective inhibition (CIN) of 0 to 2 J kg^{-1}. These values change very little during the formation period, having settled into these equilibrium values during the rapid intensification period prior to Hour 0. Within such a convectively favorable environment, we expect convective activity to be robust in the region outside of 60 km. Our model suggests that, if a secondary eyewall were to form by the processes outlined in our hypothesis, it should occur where the β-skirt overlaps with a convectively favorable region. In the control simulation, we have identified this overlap region to be between 70 and 125 km in radius.

In our hypothesis, the convection acts as a source of small-scale eddy kinetic energy in the β-skirt. To examine the kinetic energy cascade, we separate the kinetic energy into its mean flow and perturbation components and then calculate the Fourier power of the perturbation energy in azimuthal wavenumber space. Integrating the kinetic energy power in the region of the model between 60 and 150 km radius and 0 to 4 km height and weighting the integral by the mean density, we are able to approximately determine the spatial scales of the kinetic energy perturbations. This is summarized as follows, where the hatted quantities are the azimuthal Fourier components of the perturbation winds for each wavenumber n:

$$TKE(n) = \int_{0km}^{4km} \int_{60km}^{150km} \left[\bar{\rho}\left(|\hat{u}_n^2 + \hat{v}_n^2 + \hat{w}_n^2\right) drdz\right] / \int_{0km}^{4km} \int_{60km}^{150km} [\bar{\rho} drdz] \qquad (5.1)$$

In our calculation, we interpolate the data onto a cylindrical grid with 210 azimuthal points and a radial grid spacing of 2 km. Figure 5.4 shows the results of this calculation at three times during the secondary eyewall formation period. Between Hours 8 and 16, there is a gradual increase in kinetic energy power throughout the majority of the spectrum. The Hour 16 energy spectrum is approximately 30-60% greater than the Hour 8 spectrum at each azimuthal wavenumber. This increase supports the hypothesis that, in the candidate secondary eyewall formation region, there is a source of perturbation kinetic energy. We suggest that this source is increased convective activity in this region.

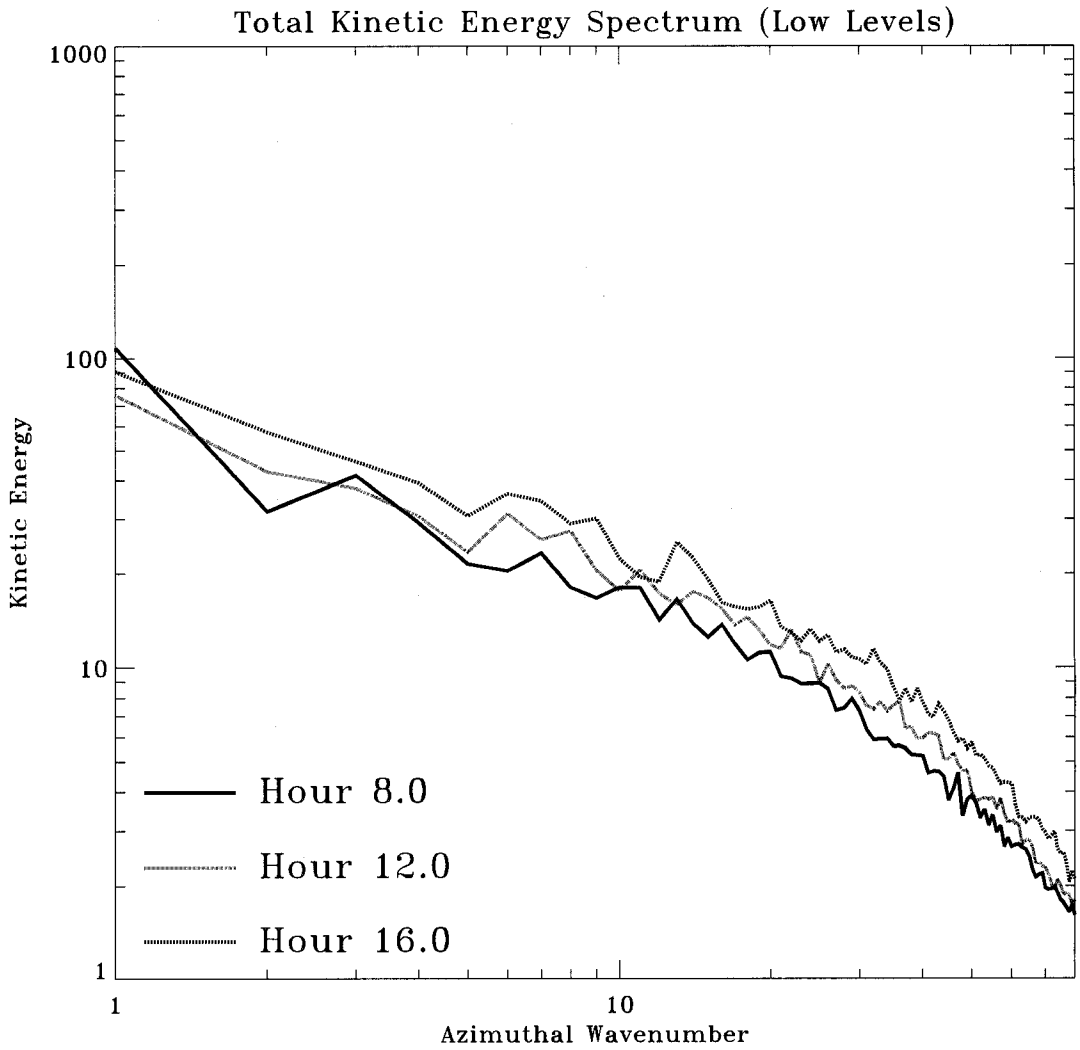

Figure 5.4: Mass-weighted low-level perturbation kinetic energy spectrum for three different times during the secondary eyewall formation period for the control experiment. Units for kinetic energy are $m^2\ s^{-2}$. The integration is for the annulus surrounding the formation region: 60 to 150 km radius and 0 to 4 km height.

To show the increase in convective activity as well as the formation of a low-level jet structure, we examine the co-location of mean diabatic heating with changes in the mean tangential wind during the formation period. Since it is easier to see small changes to a large mean field like tangential winds by examining the field as a difference from a reference field, we define $\Delta\bar{v}(r,z)$ as the change in the mean tangential winds from Hour 0.

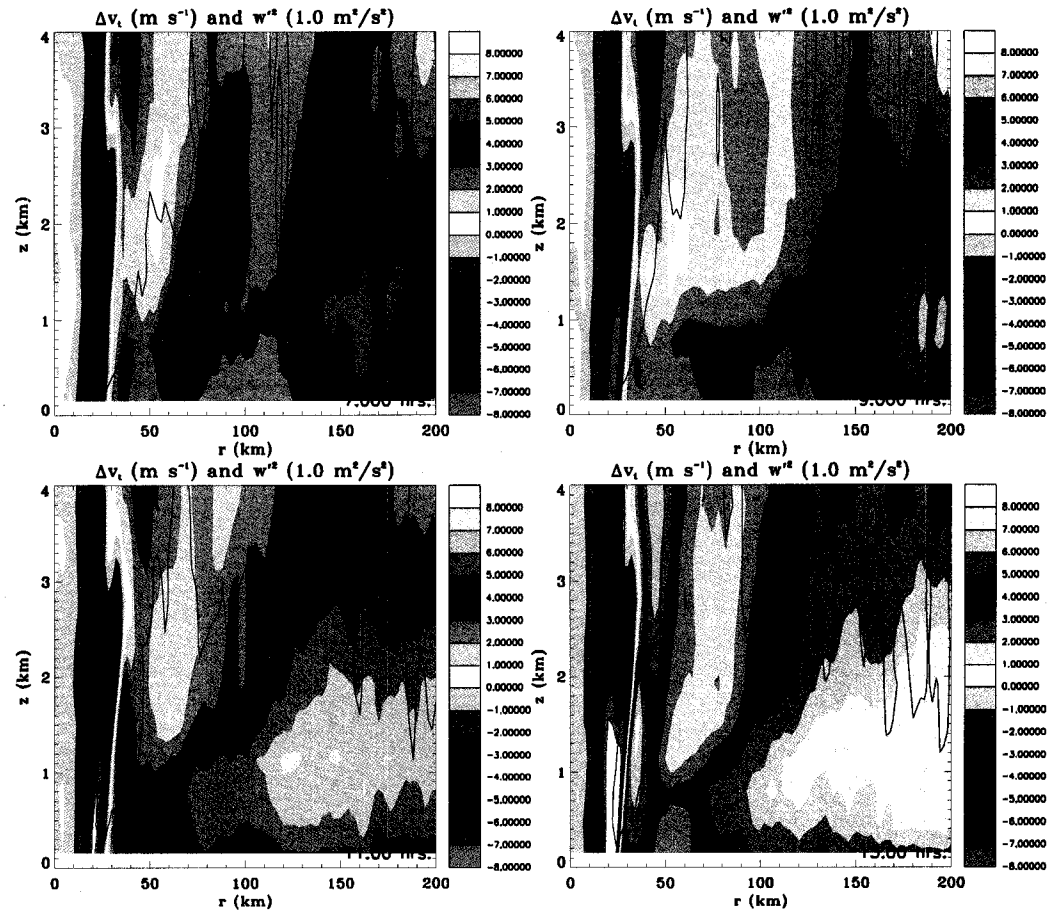

Figure 5.5: Change in the mean tangential wind (shaded, m s^{-1}) from Hour 0, along with the instantaneous mean w'^2 contour of 1 m^2 s^{-2} in thick black from the control experiment. Calculations for Hour 7 (top left), Hour 9 (top right), Hour 11 (bottom left) and Hour 13 (bottom right) show the intensification of a low-level jet.

Figure 5.5 shows the $\Delta\bar{v}$ and $\overline{w'^2}$ calculations between 0 and 200 km radius and 0 and 4 km height for four times during the secondary eyewall formation period: Hours 7, 9, 11, and 13. From Hours 7 to 9, we see little change in the mean structure of the hurricane. There is a small increase of approximately 1 m s^{-1} outside of 150 km radius around 1 km height during this time. However, during the next two hours, we see an increase of mean tangential winds by 3 to 5 m s^{-1} from 70 km to 150 km through the lowest layers of the model. The spatial scale of this cyclonic jet is approximately 40 to 60 km, which is quantitatively larger than the estimated beta length scale of 12 to 24 km. Additionally, the jet formed mainly within the overlap region we identified earlier.

The formation of the localized jet is coupled with significant convective activity, as evidenced by the solid contour in Figure 5.5, which denotes the 1 m^2 s^{-2} contour of the azimuthally averaged variance of the perturbation vertical velocity. Strong hurricane convection has been shown to have local vertical velocities ranging between 4 to 15 m s^{-1} (e.g. M06), an azimuthal mean contour of 1 m^2 s^{-2} indicates that there is a substantial amount of strong convection occurring in that annular region. From Figure 5.5, we note the continual increase in the spatial coverage of the 1 m^2 s^{-2} contour, in particular, directly above where the jet forms (in Hour 9) and just above the inner nose of the jet (in Hour 13). The former shows that convective activity was increasing prior to the strengthening of the jet. The latter is consistent with the potential feedback mechanism of WISHE in forcing convection in response to the formation of a low-level jet.

Additionally, we see an increase in low-level inflow during this time period. Figure 5.6 shows the mean radial winds at Hours 8 and 10. Here, we see that there is an increase of approximately 3 m s^{-1} in the mean inflow outside of 100 km radius and 3 km height through much of this region. This increase in inflow into this region will aid in the formation of the jet that we saw in Figure 5.5.

Assembling the evidence thus far, we see that the simulated secondary eyewall formation is consistent with the proposed hypothesis. During the time period where there

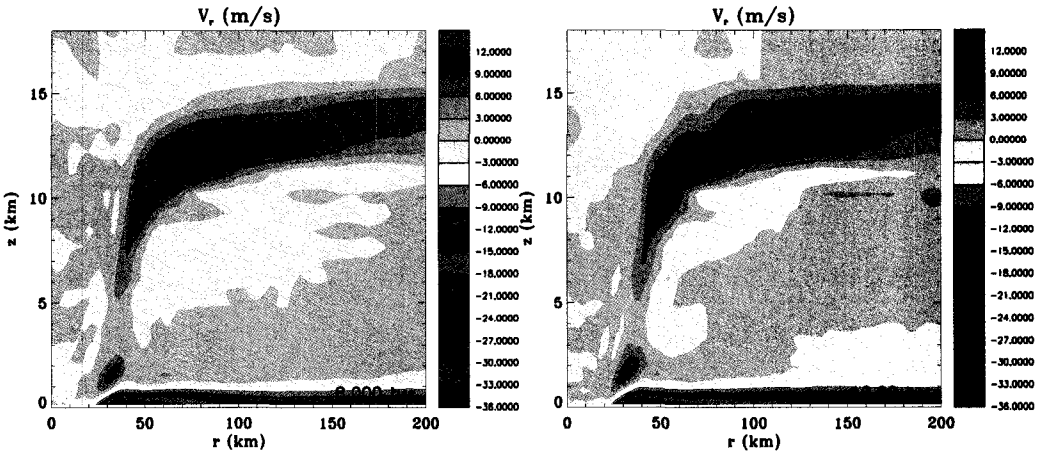

Figure 5.6: Mean radial velocity ($\bar{u}$) at Hour 8 (left) and Hour 10 (right) showing the gradual increase in the inflow in the lowest levels outside 120 km radius.

is an overlap of a sufficiently strong low-level β-skirt and favorable convective profiles, we observe an increase in perturbation kinetic energy at almost all azimuthal wavenumbers. The kinetic energy increase at high azimuthal wavenumbers and the increase in mean heating rate suggests that deep convective activity is increasing on relatively small (hot tower) scales. During the time when the eddy kinetic energy is increasing, we observe a low-level jet form and strengthen. Given the increased convective activity and the fact that the nonlinear axisymmetrization mechanism in the β-skirt would tend to force a jet with a characteristic radial scale of tens of kilometers, commensurate with the beta scale, we suggest here that the β-skirt hypothesis is a very plausible explanation. The additional help that the increased inflow forced by the convection gives in the formation of the jet was also shown and may be vital. The observation that the jet forms on the time scale of a few hours (e.g. Figure 5.5) gives additional support to the proposed hypothesis since the associated time scale for perturbations to be influenced by the β-skirt is approximately 40 to 75 minutes.

5.2 Isentropic Momentum Budget

To better isolate the specific processes that may form the secondary eyewall and its attendant secondary tangential wind maximum, we employ a momentum budget calculation. Since convection is a strongly diabatic process and secondary eyewalls are defined in terms of convection, it makes sense to look at a momentum budget on isentropic surfaces. Using an isentropic analysis allows us to more acutely gauge the role of convective heating in the momentum budget changes by separating out the diabatic portions of the change from the adiabatic portions. With these criteria in mind, we will use the budget outlined in Molinari et al (1995), hereafter refered to as M95.

In the Appendix of M95, the authors derive a tangential momentum budget in polar-isentropic coordinates. Using both the relative angular momentum equation and the mass continuity equation in polar-isentropic coordinates, they azimuthally average the combination to come up with the equation that will be the basis for our further studies.

$$(r\overline{\sigma v})_t + r^{-1}\left(r^2\left(\overline{\sigma u}\right)\overline{v}\right)_r + \left(r\left(\overline{\sigma\dot{\theta}}\right)\overline{v}\right)_\theta + r\left(\overline{\sigma u}\right)f = \nabla\cdot\vec{F} - \left(r\overline{\left(\sigma\dot{\theta}\right)'v'}\right)_\theta - \left(r\overline{\sigma' v'}\right)_t + r\overline{\sigma F^\lambda} \tag{5.2}$$

where the Eliassen-Palm(E-P) flux vector $\vec{F}$ is defined as

$$\vec{F} \equiv [-r\overline{(\sigma u)'v'}, \overline{p'\Psi'_\lambda}].$$

In Equation (5.2), u and v represent the radial and tangential winds, respectively. $\sigma \equiv -\partial p/\partial\theta$ is the pseudo-density. $\dot{\theta}$ stands for the parcel motion across θ surfaces, i.e. $D\theta/Dt$. f is the Coriolis parameter, while F_λ represents the azimuthal component of the friction tensor. The Montgomery streamfunction is denoted $\Psi \equiv gz + c_pT$. Overbars denote azimuthal averages, while primed quantities are deviations from the azimuthal mean. Local derivatives are denoted with subscripts. (One term from the original equation (A4) of M95 has been neglected here: $r\overline{(\sigma u)'f'}$. Since our simulation was performed on an f-plane, $f' = 0$.)

To better gauge the aggregate effects different processes have at various times during the evolution of the vortex, we integrate Equation (5.2) in time. Rearranging and taking the time integral from $t = 0$ to $t = T$, we get

$$\begin{aligned}\left[r\overline{\sigma}\overline{v}\right]_{t=0}^{T} &= -\int_0^T \left(r^{-1}\left(r^2\left(\overline{\sigma u}\right)\overline{v}\right)_r + r\left(\overline{\sigma u}\right)f\right)dt - \int_0^T \left(r\left(\overline{\sigma\dot{\theta}}\right)\overline{v}\right)_\theta dt \\ &\quad + \int_0^T \nabla\cdot\vec{F}dt - \int_0^T \left(r\overline{\left(\sigma\dot{\theta}\right)'v'}\right)_\theta dt - \left[r\overline{\sigma'v'}\right]_{t=0}^{T} + \int_0^T r\overline{\sigma F^\lambda}dt. \quad (5.3)\end{aligned}$$

We are most interested in $\Delta\overline{v}(T) = \overline{v}(t=T) - \overline{v}(t=0)$. To get this, expand the left-hand side:

$$\begin{aligned}r\overline{\sigma}(T)\overline{v}(T) &= r\overline{\sigma}(0)\overline{v}(0) - \int_0^T \left(r^{-1}\left(r^2\left(\overline{\sigma u}\right)\overline{v}\right)_r + r\left(\overline{\sigma u}\right)f\right)dt - \int_0^T \left(r\left(\overline{\sigma\dot{\theta}}\right)\overline{v}\right)_\theta dt \\ &\quad + \int_0^T \nabla\cdot\vec{F}dt - \int_0^T \left(r\overline{\left(\sigma\dot{\theta}\right)'v'}\right)_\theta dt - \left[r\overline{\sigma'v'}\right]_{t=0}^{T} + \int_0^T r\overline{\sigma F^\lambda}dt. \quad (5.4)\end{aligned}$$

Dividing Equation (5.4) by $r\overline{\sigma}(T)$ and subtracting $\overline{v}(0)$ from both sides gets us the desired result:

$$\begin{aligned}\Delta\overline{v}(T) &= \left(\frac{\overline{\sigma}(0)}{\overline{\sigma}(T)} - 1\right)\overline{v}(0) - \frac{1}{\overline{\sigma}(T)}\int_0^T \left(r^{-2}\left(r^2\left(\overline{\sigma u}\right)\overline{v}\right)_r + \left(\overline{\sigma u}\right)f\right)dt \\ &\quad - \frac{1}{\overline{\sigma}(T)}\int_0^T \left(\left(\overline{\sigma\dot{\theta}}\right)\overline{v}\right)_\theta dt + \frac{1}{r\overline{\sigma}(T)}\int_0^T \nabla\cdot\vec{F}dt \\ &\quad - \frac{1}{\overline{\sigma}(T)}\int_0^T \left(\overline{\left(\sigma\dot{\theta}\right)'v'}\right)_\theta dt - \frac{1}{\overline{\sigma}(T)}\left[\overline{\sigma'v'}\right]_{t=0}^{T} + \frac{1}{\overline{\sigma}(T)}\int_0^T \overline{\sigma F^\lambda}dt \quad (5.5)\end{aligned}$$

Equation (5.5) is the form of the tangential budget that we will use with our model data. Model variables are interpolated from the staggered Arakawa C-grid with 2 km spacing in the horizontal onto a cylindrical-isentropic grid with 210 azimuthal points, 2 km radial grid spacing, and 2 K isentropic grid spacing. Massless layers are used where needed. Terms involving $\dot{\theta}$ are then calculated using current and previous timestep data in a mid-point temporal averaging scheme while the other terms, excluding the friction term, are calculated at each particular timestep.

Each term on the right-hand side of Equation (5.5) represents a fundamentally different process in the tangential momentum budget change. To make referencing each term easier, we assign acronyms to each.

We call the first term, $\left(\frac{\overline{\sigma}(0)}{\overline{\sigma}(T)} - 1\right)\overline{v}(0)$, the mean pseudo-density change (MPD). This term describes the change in the tangential momentum due to changes in the mean amount of mass between isentropic surfaces. This is analogous to PV thinking, where potential vorticity can be locally changed by changing the mass between isentropic surfaces. If the amount of mass between two isentropes increases (i.e. $\bar{\sigma}(T) > \bar{\sigma}(0)$) then, by momentum conservation, there must be a loss of velocity (i.e. $\Delta\bar{v}(T) < 0$). This term encapsulates that process and, in hurricane thinking, explains the change in the wind structure of the vortex due to changes in its mean mass structure.

The second term, $-\frac{1}{\overline{\sigma}(T)}\int_0^T \left(r^{-2}\left(r^2\left(\overline{\sigma u}\right)\overline{v}\right)_r + \left(\overline{\sigma u}\right) f\right) dt$, is refered to as the mean kinematic change (MKM). MKM represents the convergence of vorticity by the mean radial winds.

We call the third term, $-\frac{1}{\overline{\sigma}(T)}\int_0^T \left(\left(\overline{\sigma\dot{\theta}}\right)\overline{v}\right)_\theta dt$, the mean thermodynamic change (MTH). This term represents the vertical transport of mean momentum across isentropes by mean diabatic heating.

We denote the fourth term, $\frac{1}{r\overline{\sigma}(T)}\int_0^T \nabla\cdot\vec{F}dt$, as the Eliassen-Palm (E-P) flux divergence term (FEP). FEP is part of the cylindrical-isentropic analogue of the pseudo E-P flux divergence derived by Tung (1986). This term represents the adiabatic effects the waves and perturbations in the vortex have on the mean tangential momentum. These are most analogous to the dynamical changes forced by adiabatic interactions between asymmetries (e.g. Melander, 1987; Montgomery and Kallenbach, 1997).

The term, $-\frac{1}{\overline{\sigma}(T)}\int_0^T \left(\overline{\left(\sigma\dot{\theta}\right)'v'}\right)_\theta dt$, represents the thermal momentum flux (FTH). Individual convective elements transport momentum across isentropic surfaces which can result in a flux of mean tangential momentum. This term embodies this process.

The sixth term, $-\frac{1}{\overline{\sigma}(T)}\left[\overline{\sigma'v'}\right]_{t=0}^{T}$, is the pseudo-density momentum flux (FPD). This term along with FEP and FTH represent the complete analogue of the E-P flux divergence (M95).

The frictional term, $\frac{1}{\overline{\sigma(T)}} \int_0^T \overline{\sigma F^{\lambda}} dt$, cannot be directly measured from the model data. This term is implicitly included in the residual calculations that follow.

Ideally, the mean terms (MPD, MKM, MTH) and the friction term balance in a way described by the Eliassen balanced vortex model (Eliassen, 1951).

By using our six-minute temporal resolution data, we can integrate each of these terms to find which terms dominate in the creation of the secondary wind maximum that we observe in our model. We focus on the period during which the low level jet we saw form in Figure 5.5: Hours 7 to 13.

Figure 5.7 is an example of one of these integrated budgets. The top-left plot is the actual $\Delta\bar{v}$ derived directly from the model data. Each of the six terms are plotted in the bottom six plots. The top-right plot is the residual needed to make the six terms add up to the actual $\Delta\bar{v}$.

From Figure 5.7, it is obvious that the residual term is quite large. Given errors in the calculation of $\dot{\theta}$, particularly in convective regions, and the errors associated with interpolation onto a isentropic-cylinrdical grid from a staggered Arakawa C-grid in Cartesian space, the magnitude of this residual may be unavoidably large. Thus, we assume that qualitative quantities are most relevant in examining the changes in the momentum profile of the control hurricane.

In the $\Delta\bar{v}$ panel, we see the intensification of the low-level jet from 90 to 140 km radius and between 305 and 315 K by 1 to 3 m s^{-1} over these two hours. This is the region that we will focus on in the following discussion.

This region is between 1 and 4 km in height, as can be seen in Figure 5.8, which shows the azimuthal mean potential temperature, i.e. $\bar{\theta}$, at Hour 9. The mean 305 K level intersects the ground at approximately 25 km radius, then rises up to just under 2 km height at 200 km radius. The 315 K level is found nearly 1.5 km above ground level in the eye of the hurricane, quickly rises up to 3 km just outside the eyewall and

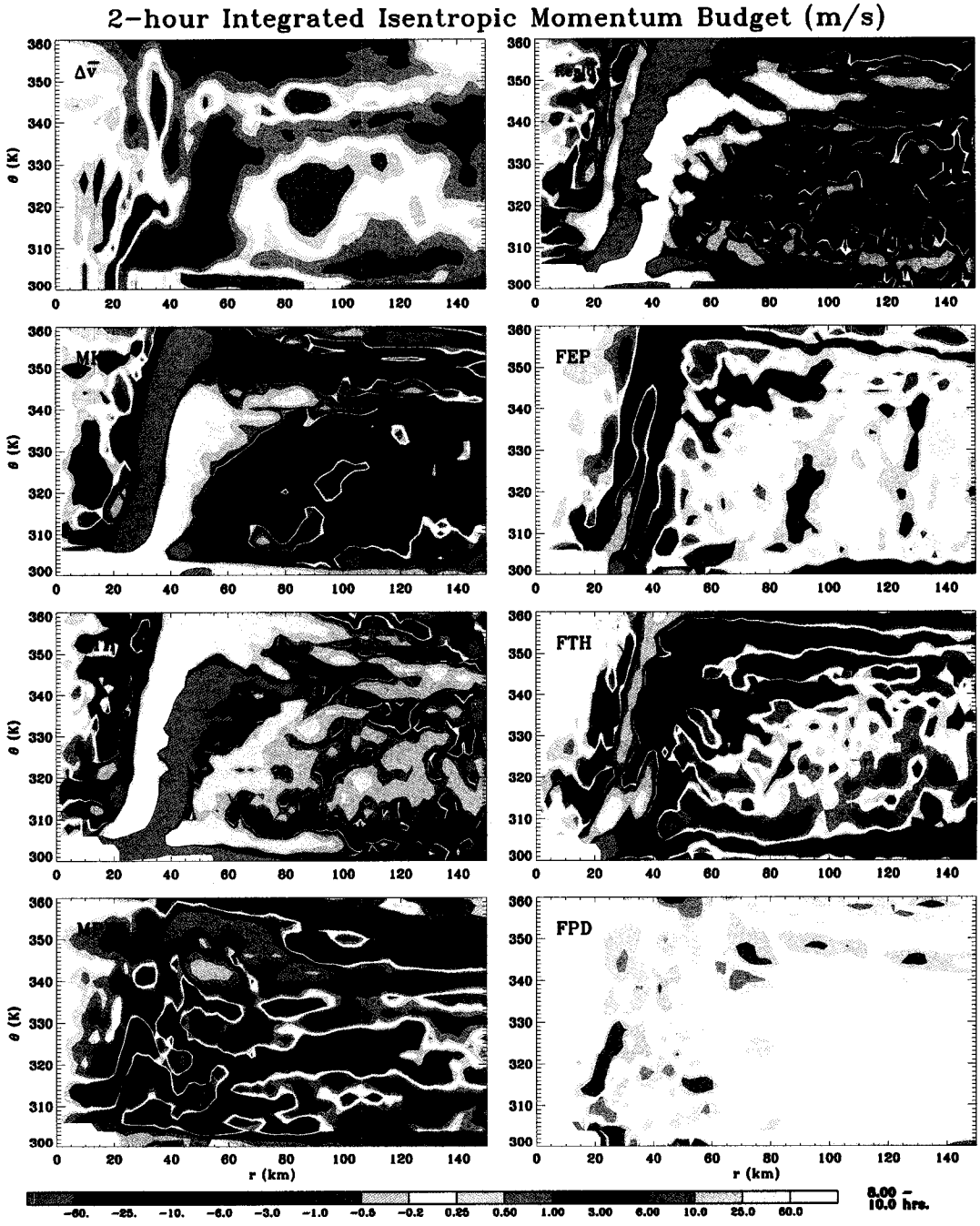

Figure 5.7: 2-hour integrated tangential momentum budget from model data. Integration takes place over the two-hour interval from Hours 8 to 10.

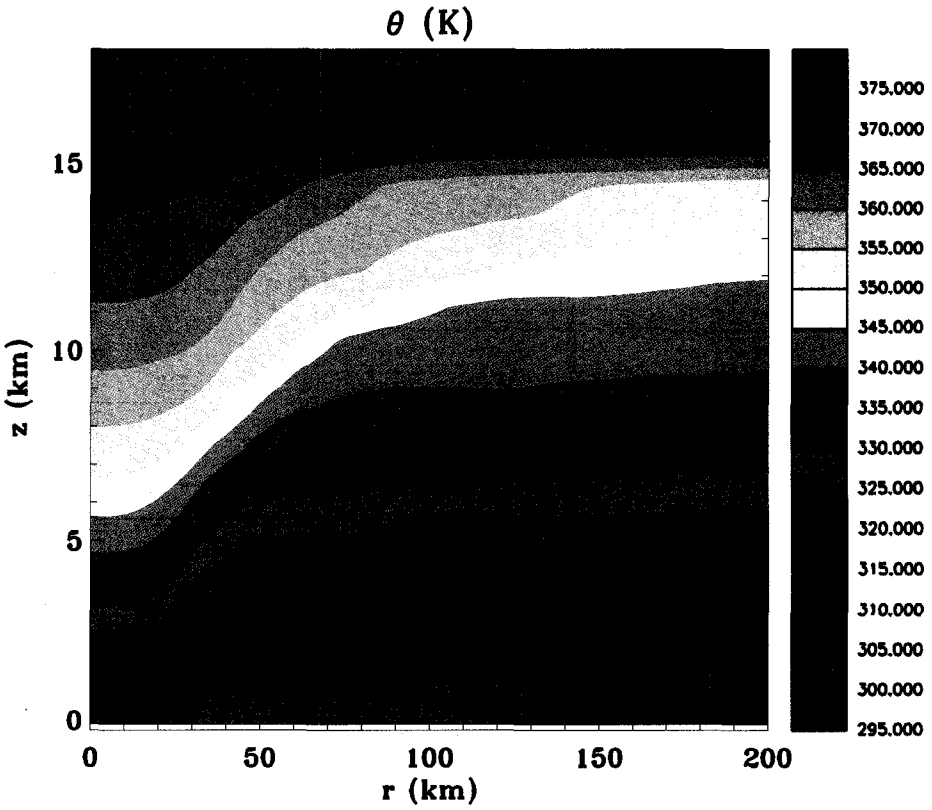

Figure 5.8: Azimuthal mean potential temperature ($\bar{\theta}$) at Hour 9.

gradually rises to 4 km height at 200 km radius. This agrees well with the region in which we had previously seen the formation of the low-level jet (i.e. Figure 5.5).

Looking specifically at the flux terms in Figure 5.7, we see that, in our region of focus, the FPD (potential density flux) term is negligable. This implies that the imbalance between the FEP and FTH terms dictate how the waves influence the mean vortex in the region of focus. Generally, we see there is a convergence of E-P flux since the FEP acceleration term is generally negative or neutral in the outer band region. Diabatic transport of momentum (FTH) is generally leading to a spin-up of 1 to 4 m/s over this two-hour period. Below 305 K, though, both terms are strongly negative.

The FEP term includes two separate adiabatic processes as seen in the expansion of the term

$$\nabla \cdot \vec{F} = -\frac{\partial\left(r^2\overline{(\sigma u)' v'}\right)}{r\partial r} + \frac{\partial\left(\overline{p'\Psi'_\lambda}\right)}{\partial\theta}. \tag{5.6}$$

The first term in the expansion of (5.6) represents the adiabatic momentum flux divergence. The second term is the adiabatic thermal flux divergence. The partitioning of the E-P flux divergence between these two terms tells us much about the mean flow changes due to the adiabatic portion of the wavelike motions.

We see in Figure 5.9 that, in the region of interest, the adiabatic thermal flux contributes very little to the calculated E-P flux momentum change, though the sign of that change is generally positive. The majority of the E-P flux momentum change comes from the momentum term. Generally, though, the momentum flux in the region of interest is negative, which explains the negative total FEP term.

In our hypothesis, we might expect that, given the turbulent nature of the axisymmetrization process, the momentum budget contribution due to the FEP term's momentum flux divergence should lead to a spinup of the vortex. However, the reality is that, locally, this term has a difficult to predict effect above the boundary layer. While the turbulent motions should deposit energy into the mean flow, this assumes that additional perturbations are not being generated or that current perturbations are not

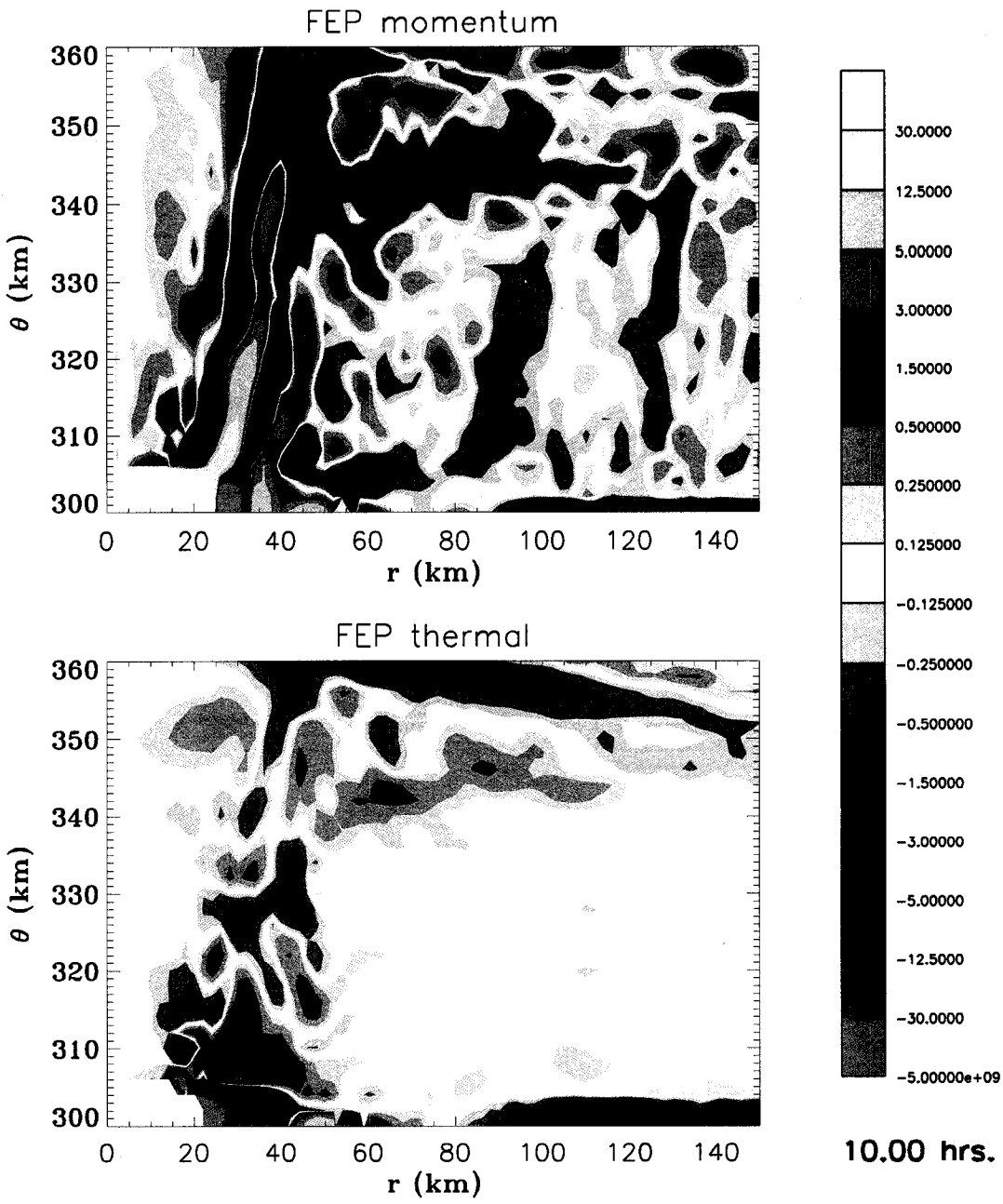

Figure 5.9: Partition of the FEP term into momentum and thermal flux mean tangential velocity changes. Contours are 1/2 of the contours in Figure 5.7.

growing. We have seen that, during this period in this region, the perturbation kinetic energy is increasing (Figure 5.4). These perturbations may be extracting momentum and energy from the mean flow as they intensify. Thus, the overall change to the mean flow due to the adiabatic momentum flux of the perturbations has a local sign which is difficult to predict.

During this time period, we note that the terms producing a positive mean momentum change in the region of interest are MKM, MPD, and FTH. The positive trend in MPD indicates a stabilization of the atmosphere in that region as the mass between the isentropes is evacuated, potentially due to increased convective activity.

The trend in MKM is due mainly to the increase in low-level inflow (radial) velocity in this region (see Figure 5.6). This trend may be attributed to increased convective activity in this region, which would tend to draw air in towards the region at low levels. This increased inflow would generate a positive change in the mean momentum as it converges momentum (Equation(5.5)).

The FTH trend indicates the positive transport of momentum through the isentropes by the convective processes. As can be seen in Figure 5.10, we would first expect to see condensational warming by an uplifted parcel at the level of free convection which is at approximately 27°C or 300K in this sounding. Thus, with an increasing $\dot{\theta}$ with increasing θ, we would anticipate that, if the perturbation velocity is also increasing with θ, the FTH term should integrate to a positive tendency just above this level.

Each of these terms can be tied nontrivially to the increased convection in this region. This observation serves to highlight the vital role of convective processes in the secondary eyewall formation process. We see that the sporadic convection not only forces a change in the azimuthal mean profile strictly by itself (e.g. Chapter 2 and Figures 2.4, 2.5, and 2.6), but also forces perturbations which change the azimuthal mean momentum profile of the outer core of the hurricane in significant ways.

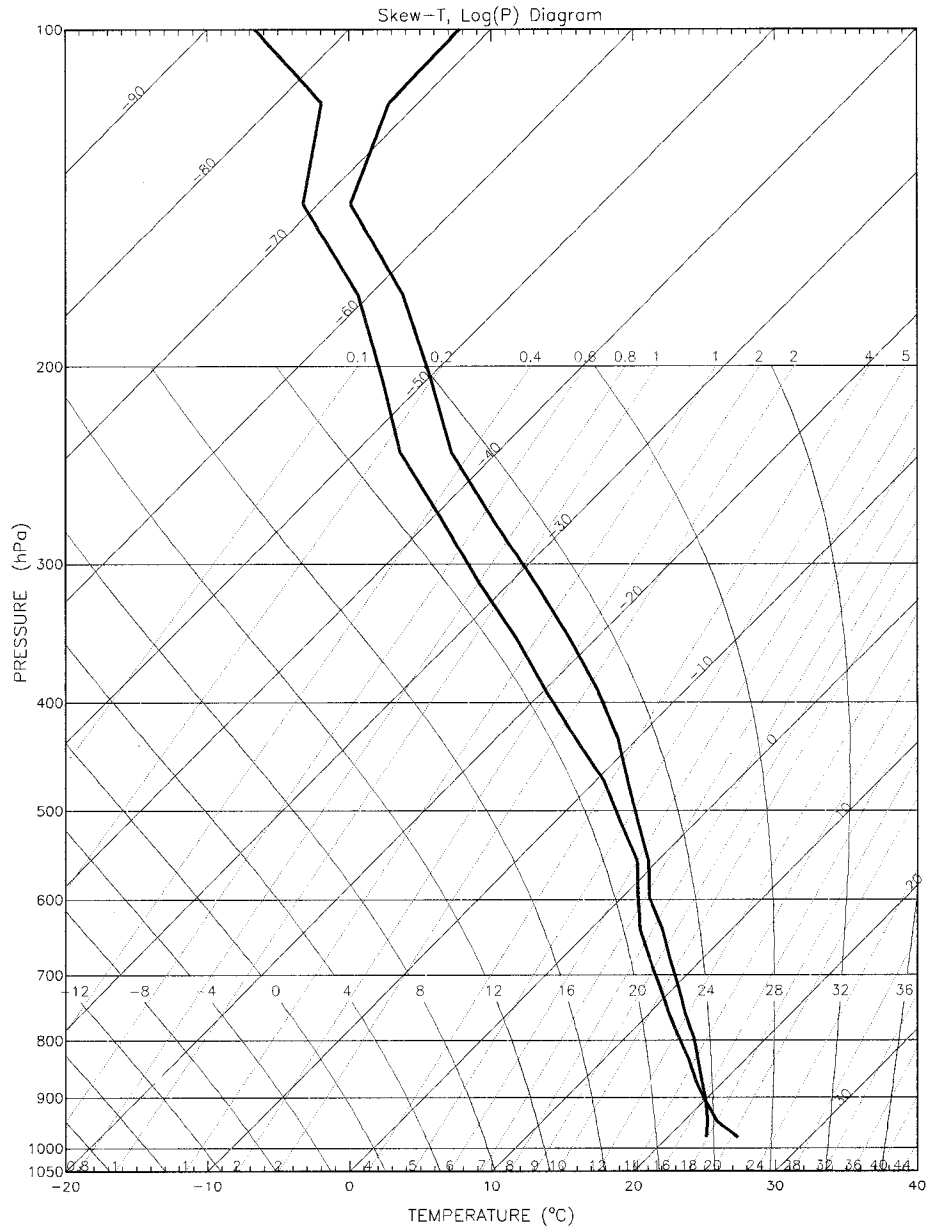

Figure 5.10: Azimuthal mean sounding at 110 km radius at Hour 11.

A note on the interpretation of the budget needs to be made. There are some issues with separating a budget into mean and eddy terms when the anomalies have non-trivial projections into the mean. As we have seen in Chapter 2 and other previous figures, the strong convection in our regions of interest has substantial effects on the mean, as well as producing strong perturbations to that mean (cf. M06). Care must be taken, therefore, in interpreting the eddy flux terms as the only terms in the budget where sporadic convection will have an effect. Some of the mean terms will be forced by the convective processes, as we have argued with the MKM term in particular.

We note that, although the budget interpretation does not provide concrete evidence, our formation hypothesis is supported by the momentum budget. We note that the budget does reinforce some of the hypothesized processes involved in secondary eyewall formation, such as the role of the more frequent convection in providing additional kinetic energy that the storm uses to force the secondary wind maximum vital for the formation of the secondary eyewall as well as highlighting the role of the increased inflow into the formation region in helping form the low-level jet.

Chapter 6

NO-ICE SENSITIVITY SIMULATION RESULTS

6.1 Basics

The no-ice simulation uses the exact same RAMS model setup as the control simulation, except that only two microphysical species are utilized: cloud droplets and rain. All ice microphysical species are nonexistent in the no-ice simulation.

This experiment is performed for three main reasons. First, it allows us to test the Willoughby (1984) ice microphysics hypothesis summarized in Table 4.1. Second, if it also forms a secondary eyewall, it is another simulation that we can examine the validity of our hypothesis in. Lastly, close comparisons between the two simulations can show the sensitivities the RAMS has with long-time hurricane simulations and their microphysical parameterizations.

The no-ice simulation is run out to 204 hours with three-hour output resolution. Like the control simulation, we will examine a smaller timeframe around any secondary eyewall formation period with higher temporal resolution. In the no-ice simulation, we will more closely examine the 24-hour period after 168 hours. We denote a new time coordinate, Hour 0, to be coincident with the time 168 hours into this simulation.

Figure 6.1 summarizes the three commonly-used hurricane metrics for the no-ice simulation. Here, we see a model storm that is not unlike the control simulation's storm.

The no-ice storm takes approximately 48 hours to begin consolidating into a small hurricane, after which it rapidly intensifies. Seventy-two hours into the simulation, the

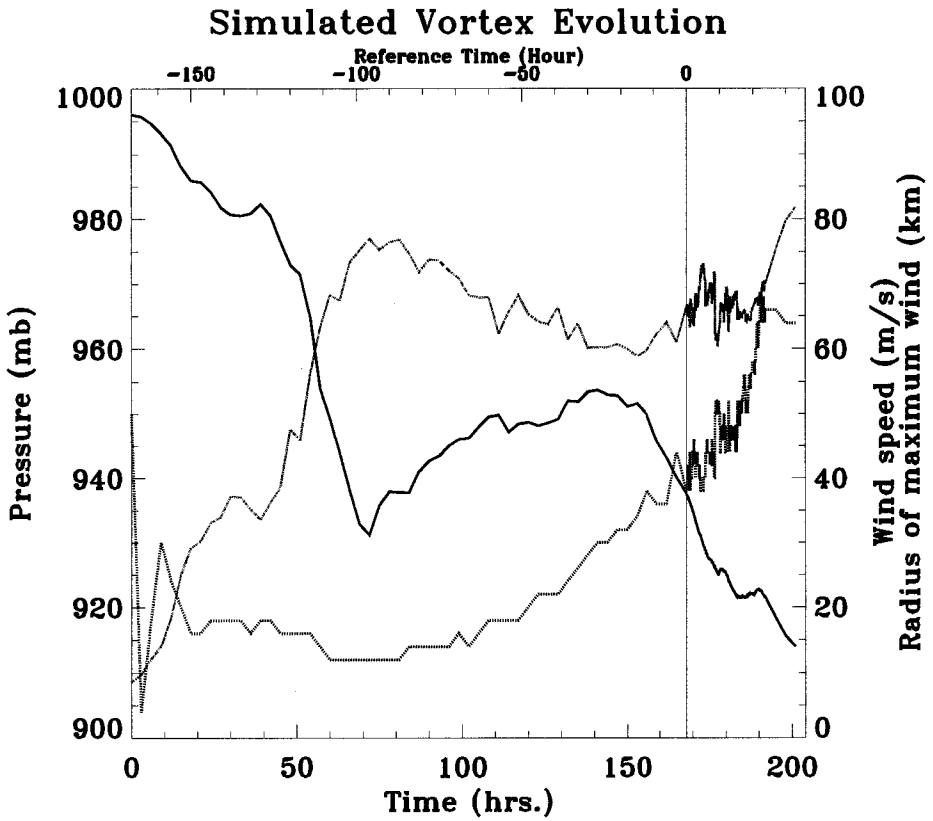

Figure 6.1: Evolution of the no-ice simulation. The solid line is lowest pressure observed at the lowest model layer (approximately 150 m). The dotted line is the maximum azimuthal mean tangential velocity in the lowest model layer. The dashed line is the radius of that maximum tangential velocity in kilometers.

no-ice storm has become a tight, strong hurricane, with maximum mean tangential winds of 75 m s^{-1} and a RMW between 10 and 15 km.

Unlike the control simulation, however, after reaching this intensity, the storm begins a period of gentle weakening. The pressure rises slowly (approximately 1 mb every 5 hours) while the maximum mean winds decrease (approximately 1 m s^{-1} every 4 hours). During this period, the RMW also begins increasing, from approximately 15 km at 100 hours into the simulation to 40 km at 168 hours.

Approximately 150 hours into the simulation, the no-ice storm begins a second period of intensification. This period is qualitatively similar to the one observed in the control simulation (cf. Figure 3.2). The minimum central pressure drops at a rate of nearly 1 mb per hour just prior and during the period surrounding Hour 0. However, unlike the control simulation, the maximum mean winds do not increase appreciably. Instead, the winds fluctuate between 65 and 70 m s^{-1}. The reasons for this change in behavior from the control simulation are still under investigation.

The secondary eyewall replacement is not as obvious in the no-ice simulation as it is in the control simulation when comparing Figures 3.2 and 6.1. This is mainly due to the fact that the inner eyewall's convection remains robust until the secondary eyewall has contracted to within 20 km of the inner eyewall. This can be seen in the time-radius plot of the azimuthal mean vertical velocity in the middle levels (Figure 6.2).

In Figure 6.2, we note that the secondary eyewall forms at approximately Hour 18 around 100 km radius. Just prior to this time, the primary eyewall is diffuse in the mean profile, with a radial extent of 20 to 30 km. This weak mean projection is due partially to the primary eyewall undergoing slight polygonal and elliptical phases (Figure 6.3).

Figure 6.3 shows the evolution of the vertical velocity field during the secondary eyewall formation in the no-ice simulation. While this eyewall pair is not as obvious and distinct as that in the control simulation, there is little doubt from both Figures 6.2 and 6.3 that the no-ice simulation undergoes a full secondary eyewall cycle.

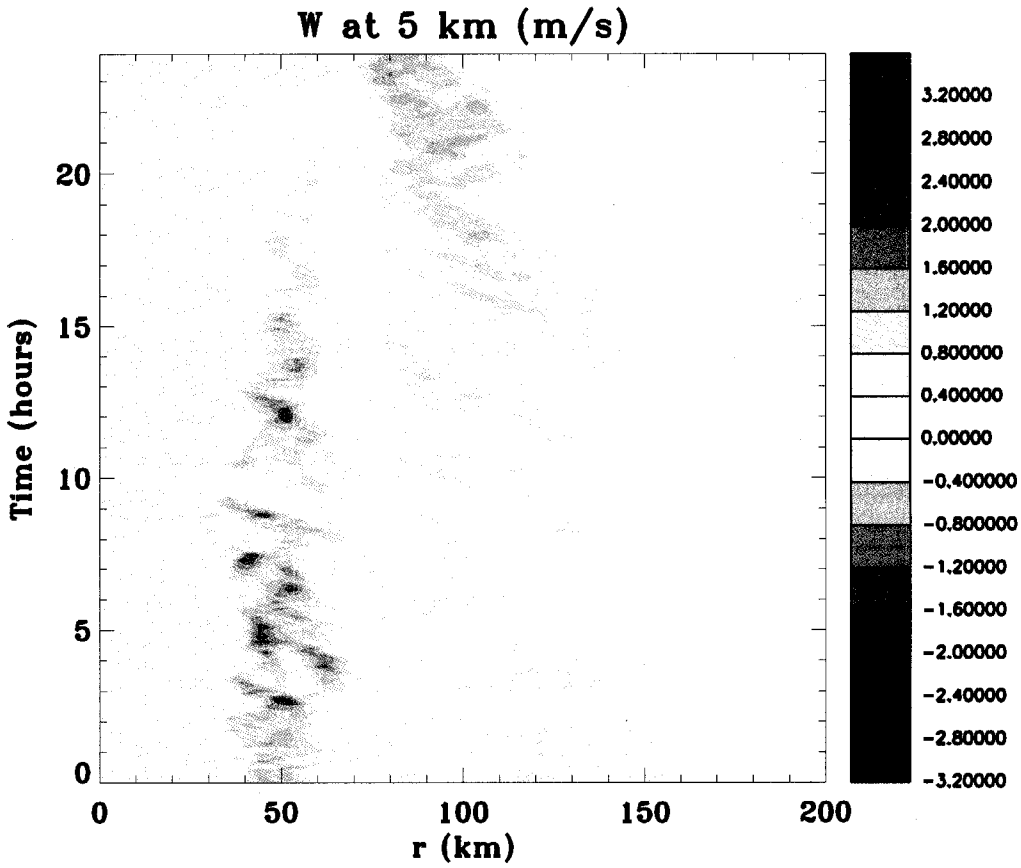

Figure 6.2: Time-radius plot of the azimuthal mean vertical velocity at 5 km height.

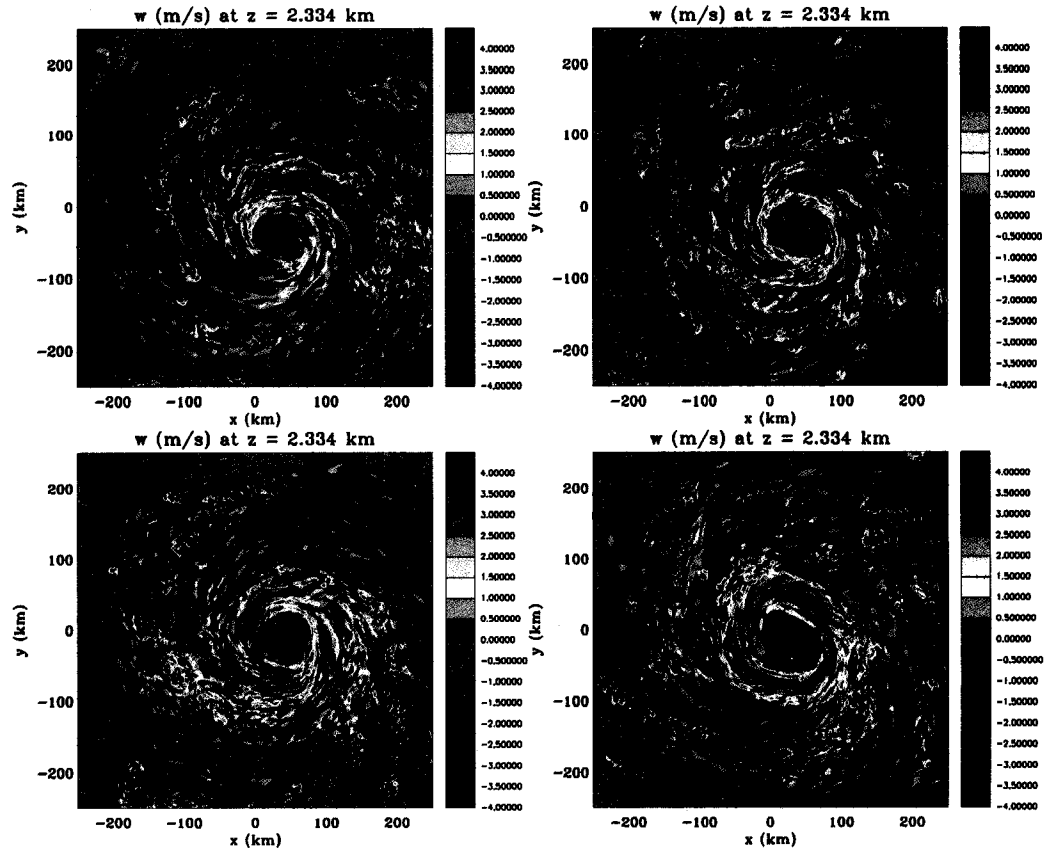

Figure 6.3: Vertical velocity at 2.2 km height in the no-ice simulation. Times shown are Hours 7.5 (top left), 10.5 (top right), 13.5 (bottom left), and 16.5 (bottom right). During this time, the secondary eyewall forms. Both eyewalls are readily visible at Hour 16.5.

6.2 Results

We begin the examination of this experiment's secondary eyewall formation by looking for the presence of a β-skirt. Figure 6.4 shows the four-hour averaged effective β and τ_{fil} calculations for Hours 5 to 9. The existence of a positive β-skirt out to 110 km radius is clearly evident. Additionally, τ_{fil} is greater than 30 minutes outside of a radius of 75 km. By our hypothesis, then, we would expect that, if there were a secondary eyewall formation, it would occur between 75 and 110 km radius, assuming that the thermodynamics are also favorable in this region.

Mean soundings (Figure 6.5) show a surface-based CAPE of 1100 to 1500 J kg^{-1} outside of 70 km, with generally small (0-2 J kg^{-1}) values of CIN. Looking back at Figure 6.2, we see that the first significant convection that eventually forms into the secondary eyewall occurs around Hours 12 to 13 and at radius 80 to 110 km.

As with the control simulation, we also see the formation of a low-level jet a few hours before the secondary eyewall is fully formed. Figure 6.6 shows the change in the mean tangential velocity from Hour 0 for four times during the formation period in the no-ice experiment. We see a similar evolution as in Figure 8, where a jet forms rather quickly. The change in the mean swirling flow between Hours 6 and 10 is approximately 4 to 6 m s^{-1}. Additionally, there appears to be more significant convective activity during this period as the coverage of the 1 m^2 s^{-2} mean vertical velocity variance contour increases.

Similar to what was seen in the mean radial winds in the control simulation, we see that the mean low-level inflow increases during the formation of the low-level jet (Figure 6.7). This suggests that the increased convection during this time induces additional radial inflow, which converges momentum into the low-level jet and strengthens it.

Comparing the control and no-ice simulations, we see many similarities in the formation of the secondary eyewalls, although the two simulated secondary eyewalls have

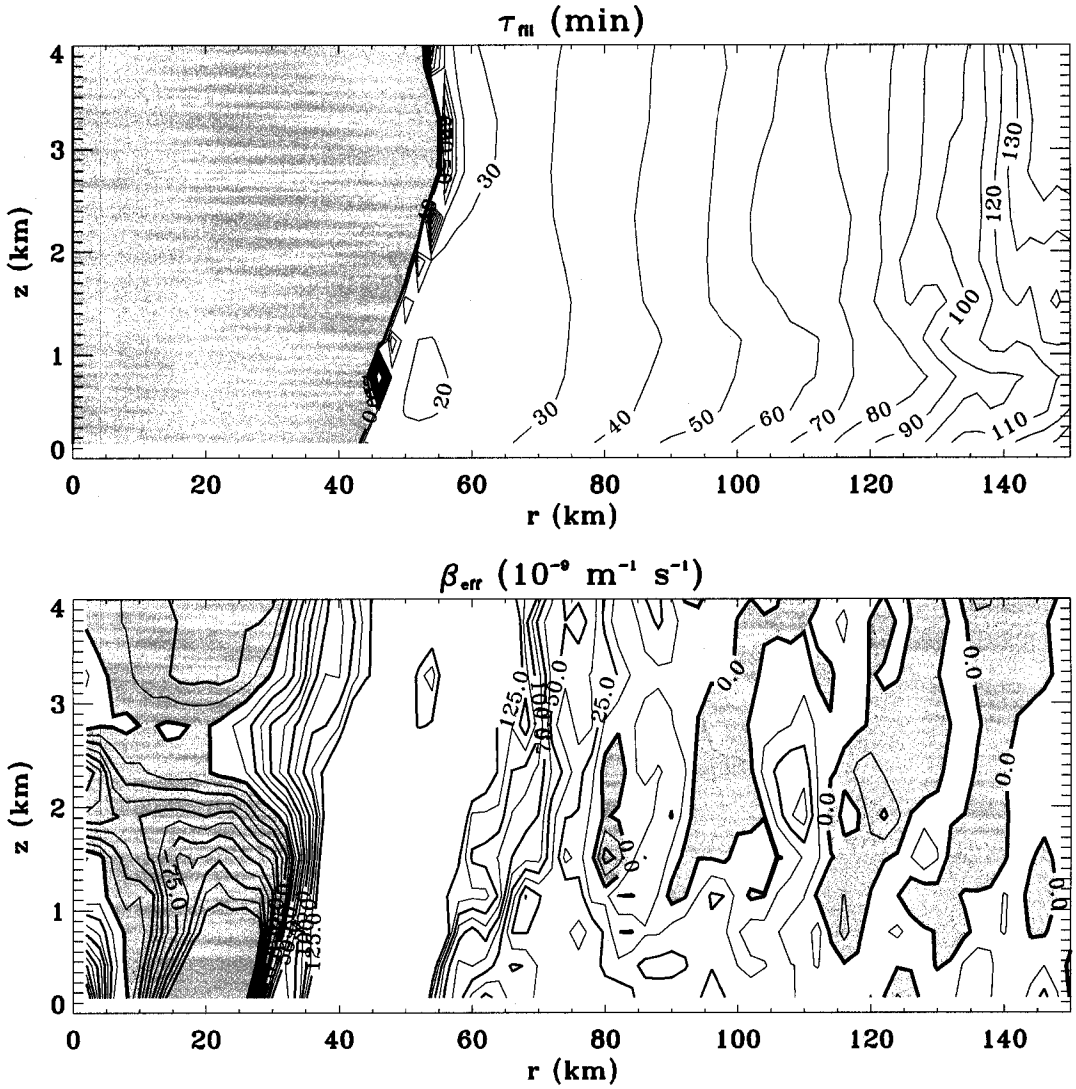

Figure 6.4: Calculations of τ_{fil} and β for the no-ice simulation. This calculation uses temporally averaged azimuthal mean quantities from Hours 5 to 9. Contours as in Figure 5.1.

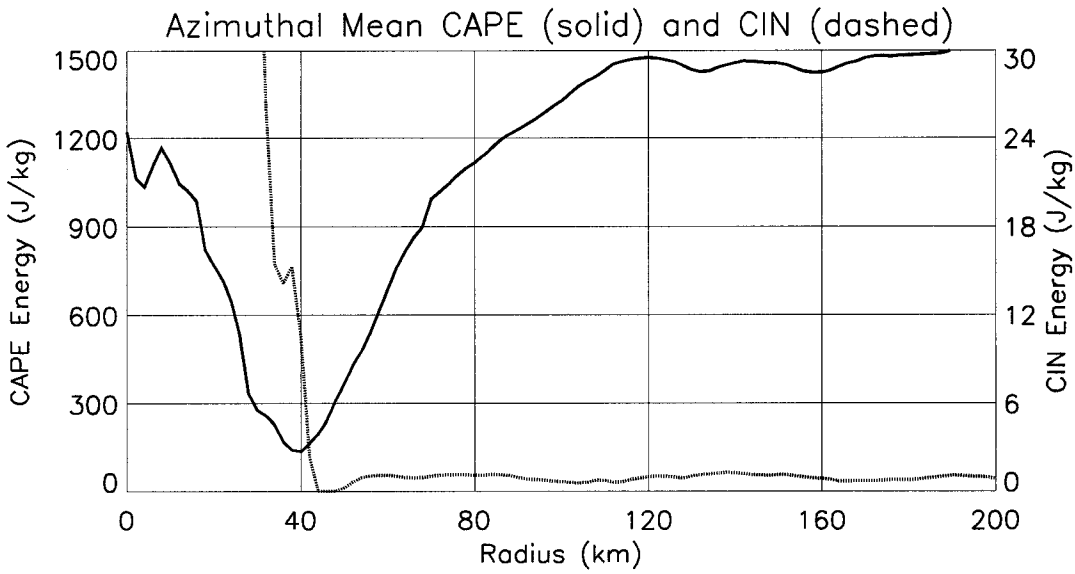

Figure 6.5: Surface-based CAPE and CIN calculations using azimuthal mean quantities at Hour 6.

different eventual evolutions. We note that there is the formation of a low-level jet prior to the completion of the convective ring, along with an increased amount of sporadic convection. This convection is also occuring in the overlap region between the β-skirt and region of convectively-favorable dynamics and thermodynamics, as alluded to in our hypothesis. This simulation, therefore, gives additional credence to our hypothesized secondary eyewall formation paradigm.

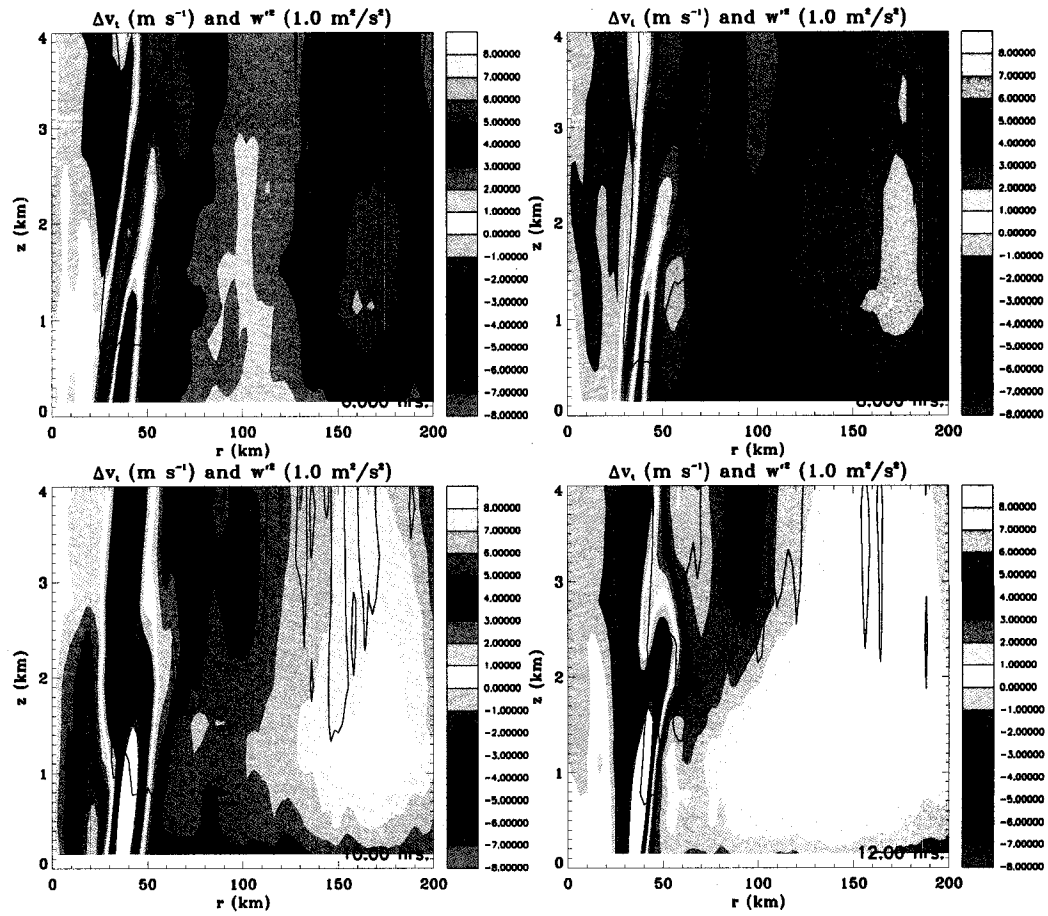

Figure 6.6: Change in the mean tangential wind (shaded, m s^{-1}) from Hour 0, along with the instantaneous mean w'^2 contour of 1 m^2 s^{-2} in thick black from the no-ice experiment. Calculations for Hour 6 (top left), Hour 8 (top right), Hour 10 (bottom left) and Hour 12 (bottom right) show the intensification of a low-level jet.

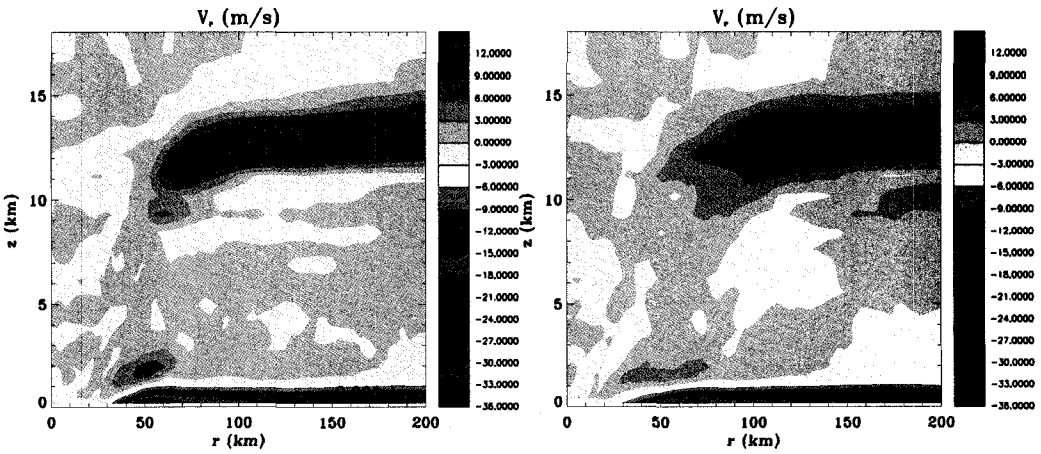

Figure 6.7: Mean radial velocity ($\bar{u}$) at Hour 8 (left) and Hour 10 (right) showing the gradual increase in the inflow in the lowest levels outside 120 km radius in the no-ice simulation.

Chapter 7

DISCUSSION AND CONCLUSIONS

The formation of a secondary eyewall is one of the most important current problems in the forecasting of mature hurricane intensity. While we have an understanding of the processes by which the secondary eyewall becomes the dominant eyewall in the tropical cyclone, how the secondary eyewall forms in the first place has been little more than a guess.

A number of hypotheses and ideas have been offered to explain this feature, although most of these were shown to be unnecessary in the formation of our simulated secondary eyewalls. Unsatisfied by the lack of a comprehensive hypothesis and supporting theoretical basis for secondary eyewall formation, we have used idealized full-physics hurricane simulations to offer a new hypothesis on the formation process.

The idea begins with a new view of a mature tropical cyclone, one with a low-level β-skirt as seen in composite observations (Mallen et al., 2005). If there is a substantial overlap between this β-skirt and an area of strong convective potential (i.e. large filamentation timescales, sufficient CAPE, and low CIN), we envision that convection will readily form in this region. Convective activity acts as a source of eddy kinetic energy that, in the presence of a sufficiently well developed β-skirt, will tend to generate one or more localized cyclonic jet maxima whose radial scale will be on the order of the local beta scale. In the hurricane problem, an equivalent barotropic mean radial potential vorticity gradient is substituted for the meridional gradient of planetary vorticity proposed originally for large-scale oceanic and atmospheric flows by Rhines (1975). In addition to

the symmetrization of these convective eddies, we envision that the radial inflow induced by this convection helps concentrate momentum into the low levels, aiding in the formation of the nascent low-level jet. Upon coupling with the boundary layer via sensible and latent heat exchanges from the ocean surface, this jet can then amplify and force additional cumulus convection.

Using our high-resolution, long-time hurricane simulations, we show supporting evidence that this process may be occurring in the model atmosphere. Hours before the secondary eyewall forms, we observe the presence of a well-defined β-skirt, as well as an overlap region where convection is not significantly hindered by weak thermodynamics or strong straining dynamics from the primary swirling flow. In this overlap region, we see an increase in perturbation kinetic energy and an increase in dynamical signals of convection, along with the rapid formation of a low-level jet that within a few short hours amplifies into a secondary eyewall.

Since we have shown that similar results are found without ice microphysical processes, we conclude that the physics of secondary eyewall formation are not essentially dependent on ice microphysics.

The hypothesis is intrinsic to the major tropical cyclone, requiring no specific outside influences to trigger it. However, our hypothesis does not specifically include the possibility that environmental influences like shear, interaction with synoptic potential vorticity anomalies, interaction with landmasses, or other synoptic interactions may produce a secondary eyewall. We suspect that the effects of these influences may fit naturally into the formation framework we have introduced here. Further research on the role of these different environmental influences in the formation of the secondary eyewall needs to be completed.

Our secondary eyewall formation hypothesis also assumes that the two-dimensional β-plane and spherical turbulence theories are extensible to the low-levels of the major hurricane vortex. The fluid dynamics of this process, though, are not currently well

understood. Simple modeling and theoretical studies of this potential phenomenon need to be completed.

Additional future work includes posteriori analysis of observational hurricane datasets where secondary eyewalls have been observed to form to gauge the operational usefulness of this hypothesis. One such dataset is the RAINEX experiment dataset for Hurricane Rita (2005) (Houze et al. 2007). Careful examination of this dataset has just begun and should provide additional insights in the potential validity and usefulness of our hypothesis from forecasting and observational standpoints.

Chapter 8

REFERENCES

Barnes, G. M., E. J. Zipser, D. Jorgensen, and F. Marks, 1983: Mesoscale and convective structure of a hurricane rainband. *J. Atmos. Sci.*, **40**, 2125-2137.

Bell, M. M., and M. T. Montgomery, 2007: Observed structure, evolution and potential intensity of category five Hurricane Isabel (2003) from 12-14 September. *Mon. Wea. Rev., in press.*

Black, M. L., and H. E. Willoughby, 1992: The concentric eyewall cycle of Hurricane Gilbert. *Mon. Wea. Rev.*, **120**, 947-957.

Braun, S. A., M. T. Montgomery, and Z. Pu, 2006: High-resolution simulation of Hurricane Bonnie (1998). Part I: The organization of eyewall vertical motion. *J. Atmos. Sci.*, **63**, 19-42.

Brunet, G., 1994: Empirical normal-mode analysis of atmospheric data. *J. Atmos. Sci.*, **51**, 932-952.

Brunet, G., and M. T. Montgomery, 2002: Vortex Rossby waves on smooth circular vortices. Part I: Theory. *Dyn. Atmos. Ocean.*, **35**, 153-177.

Camp, J. P., and M. T. Montgomery, 2001: Hurricane maximum intensity: Past and present. *Mon. Wea. Rev.*, **129**, 1704-1717.

Charney, J. G., 1971: Geostrophic turbulence. *J. Atmos. Sci.*, **28**, 1087-1095.

Chen, Y., G. Brunet, M. K. Yau, 2003: Spiral bands in a simulated hurricane. Part II: Wave activity diagnostics. *J. Atmos. Sci.*, **60**, 1239-1256.

Chen, Y., and M. K. Yau, 2001: Spiral bands in a simulated hurricane. Part I: Vortex Rossby wave verification. *J. Atmos. Sci.*, **58**, 2128-2145.

Clark, T. L., and R. D. Farley, 1984: Severe downslope windstorm calculations in two and three spatial dimensions using anelastic grid nesting: A possible mechanism for gustiness. *J. Atmos. Sci.*, **41**, 329-350.

Cotton, W. R., and Coauthors, 2003: RAMS 2001: Current status and future directions. *Meteor. Atmos. Phys.*, **82**, 5-29.

Dodge, P., R. W. Burpee, and F. D. Marks Jr., 1999: The kinematic structure of a hurricane with sea level pressure less than 900 mb. *Mon. Wea. Rev.*, **124**, 987-1004.

Dritschel, D. G., and D. W. Waugh, 1992: Quantification of the inelastic interaction of unequal vortices in two-dimensional vortex dynamics. *Phys. Fluids*, **A4**, 1737-1744.

Dvorak, V., 1995: Tropical clouds and cloud systems observed in satellite imagery: Tropical cyclones. Workbook volume 2. Available from NOAA/NESDIS, 5200 Auth Rd., Washington, DC, 20233.

Eliassen, A., 1951: Slow thermall or frictionall controlled meridional circulation in a circular vortex. *Astrophys. Norv.*, **5**, 19-60.

Emanuel, K. A., 1989: The finite-amplitude nature of tropical cyclogenesis. *J. Atmos. Sci.*, **46**, 3431-3456.

Emanuel, K. A., 1994: Atmospheric convection. Oxford University Press. 580 pp.

Emanuel, K. A., 1995: The behavior of a simple hurricane model using a convective scheme based on subcloud-layer entropy equilibrium. *J. Atmos. Sci.*, **52**, 3960-3968.

Enagonio, J. E., and M. T. Montgomery, 2001: Tropical cyclogenesis via convectively forced vortex Rossby waves in a shallow water primitive equation model. *J. Atmos. Sci.*, **58**, 685-706.

Frank, W. M., 1977: The structure and energetics of the tropical cyclone. I: Storm structure. *Mon. Wea. Rev.*, **105**, 1119-1135.

Franklin, C. N., G. J. Holland, and P. T. May, 2006: Mechanisms for the generation of mesoscale vorticity features in tropical cyclone rainbands. *Mon. Wea. Rev.*, **134**, 2649-2669.

Frisch, U., 1996: Turbulence: The legacy of A. N. Kolmogorov. Cambridge Univ. Press, 310 pp.

Gray, W. M., and D. J. Shea, 1973: The hurricane's inner core region. II. Thermal stability and dynamic characteristics. *J. Atmos Sci.*, **30**, 1565-1576.

Haltiner, G. J., and R. T. Williams, 1980: Numerical prediction and dynamic meteorology. John Wiley and Sons, 496 pp.

Harrington, J. Y., 1997: The effects of radiative and microphysical processes on simulated warm and transitional season arctic stratus. Ph.D. thesis, Colorado State University, 289 pp.

Hawkins, H. F., 1983: Hurricane Allen and island obstacles. *J. Atmos. Sci.*, **40**, 1360-1361.

Hawkins, J. D., and M. Helveston, 2004: Tropical cyclone multiple eyewall characteristics. 26th Conf. on Hurr. and Trop. Met., Preprints, AMS, 276-277.

Haynes, P. H., and M. E. McIntyre, 1987: On the evolution of vorticity and potential vorticity in the presence of diabatic heating and frictional or other forces. *J. Atmos. Sci.*, **44**, 828-841.

Hill, G. E., 1974: Factors controlling the size and spacing of cumulus clouds as revealed by numerical experiments. *J. Atmos. Sci.*, **31**, 646-673.

Houze, R. A., S. Chen, W.-C. Lee, R. Rogers, J. Moore, G. Stossmeister, M. Bell, J. Cetrone, W. Zhao, and S. Brodzik, 2006: The Hurricane Rainband and Intensity

Change Experiment: Observations and modeling of hurricanes Katrina, Ophelia, and Rita. *Bull. Amer. Meteor. Soc.*, **87**, 1503-1521.

Houze, R. A., S. S. Chen, B. F. Smull, W.-C. Lee, and M. M. Bell, 2007: Hurricane intensity and eyewall replacement. *Science*, **315**, 1235-1239.

Huang, H.-P., and W. A. Robinson, 1998: Two-dimensional turbulence and persistent zonal jets in a global barotropic model. *J. Atmos. Sci.*, **55**, 611-632.

Jordan, C. L., 1958: Mean soundings for the West Indies area. *J. Meteor.*, **15**, 91-97.

Klemp, J. B, 1987: Dynamics of tornadic thunderstorms. *Annu. Rev. Fluid Mech.*, **19**, 369-402.

Kossin, J. P., W. H. Schubert, and M. T. Montgomery, 2000: Unstable interactions between a hurricanes primary eyewall and a secondary ring of enhanced vorticity. *J. Atmos. Sci.*, **57**, 3893-3917.

Kraichnan, R. H., 1967: Inertial ranges in two-dimensional turbulence. *Phys. Fluid*, **10**, 1417-1423.

Kuo, H.-C., L.-Y. Lin, C.-P. Chang, and R. T. Williams, 2004: The formation of concentric vorticity structures in typhoons. *J. Atmos. Sci.*, **61**, 2722-2734.

Kuo, H.-C., W. H. Schubert, C.-L. Tsai, and Y.-F. Kuo, 2007: Vortex interactions and the barotropic aspects of concentric eyewall formation. *J. Atmos. Sci.*, submitted.

Lilly, D. K., 1962: On the numerical simulation of buoyant convection. *Tellus*, **14**, 148-172.

Louis, J. F., 1979: A parametric model of vertical eddy fluxes in the atmosphere. *Bound.-Layer Meteor.*, **17**, 187-202.

Maclay, K.S., M. DeMaria, and T.H. Vonder Haar, 2007: Tropical cyclone size evolution. *Mon. Wea. Rev., submitted.*

Mallen, K. J., M. T. Montgomery, and B. Wang, 2005: Reexamining the near-core radial structure of the tropical cyclone primary circulation: Implications for vortex resiliency. *J. Atmos. Sci.*, **62**, 408-425.

McWilliams, J. C., 1984: The emergence of isolated coherent vortices in turbulent flow. *J. Fluid Mech.*, **146**, 21-43.

McWilliams, J. C., 2006: Fundamentals of geophysical fluid dynamics. Cambridge Univ. Press, 266 pp.

McWilliams, J. C., and G. R. Flierl, 1979: On the evolution of isolated, nonlinear vortices. *J. Phys. Ocean.*, **9**, 1155-1182.

Molinari, J., and S. Skubis, 1985: Evolution of the surface wind field in an intensifying tropical cyclone. *J. Atmos. Sci.*, **42**, 2856-2879.

Molinari, J., S. Skubis, and D. Vallaro, 1995: External influences on hurricane intensity. Part III: Potential vorticity structure. *J. Atmos. Sci.*, **52**, 3593-3606.

Molinari, J., and D. Vallaro, 1989: External influences on hurricane intensity. Part I: Outflow layer eddy angular momentum fluxes. *J. Atmos. Sci.*, **46**, 1093-1105.

Möller, J. D., and M. T. Montgomery, 2000: Tropical cyclone evolution via potential vorticity anomalies in a three-dimensional balance model. *J. Atmos. Sci.*, **57**, 3366-3387.

Montgomery, M. T., and G. Brunet, 2002: Vortex Rossby waves on smooth circular vortices. Part II: Idealized numerical experiments for tropical cyclone and polar vortex interiors. *Dyn. Atmos. Ocean.*, **35**, 179-204.

Montgomery, M. T., and R. J. Kallenbach, 1997: A theory for vortex Rossby waves and its application to spiral bands and intensity changes in hurricanes. *Quart. J. Roy. Meteor. Soc.*, **123**, 435-465.

Montgomery, M. T., M. E. Nicholls, T. A. Cram, and A. B. Saunders, 2006: A vortical hot tower route to tropical cyclogenesis. *J. Atmos. Soc.*, **63**, 355-386.

Montgomery, M. T., and L. J. Shapiro, 1995: Generalized Charney-Stern and Fjortoft theorems for rapidly rotating vortices. *J. Atmos. Sci.*, **52**, 1829-1833.

Nong, S., and K. Emanuel, 2003: A numerical study of the genesis of concentric eyewalls in hurricanes. *Quart. J. Royal Meteor. Soc.*, **129**, 3323-3338.

Pielke, R. A., and Coauthors, 1992: A comprehensive meteorological modeling system - RAMS. *Meteor. Atmos. Phys.*, **49**, 69-91.

Raymond, D. L., C. Lopez-Carillo, L. Lopez Cavazos, 1998: Case-studies of developing east Pacific easterly waves. *Quart. J. Royal Meteor. Soc.*, **124**, 2005-2034.

Reasor, P. D., M. T. Montgomery, and L. F. Bosart, 2005: Mesoscale observations of the genesis of Hurricane Dolly (1996). *J. Atmos. Sci.*, **62**, 3151-3171.

Rhines, P. B., 1975: Waves and turbulence on a beta-plane. *J. Fluid Mech.*, **69**, 417-443.

Rotunno, R., and K. A. Emanuel, 1987: An air-sea interaction theory for tropical cyclones. Part II: Evolutionary study using a nonhydrostatic axisymmetric numerical model. *J. Atmos. Sci.*, **44**, 542-561.

Rozoff, C. M., W. H. Schubert, B. D. McNoldy, and J. P. Kossin, 2006: Rapid filamentation zones in intense tropical cyclones. *J. Atmos. Sci.*, **65**, 325-340.

Schecter, D. A., and M. T. Montgomery, 2007: Waves in a cloudy vortex. *J. Atmos. Sci.*, **64**, 314-337.

Shapiro, L. J., 1992: Hurricane vortex motion and evolution in a three-layer model. *J. Atmos. Sci.*, **49**, 140-154.

Shapiro, L. J., and M. T. Montgomery, 1993: A three-dimensional balance theory for rapidly rotating vortices. *J. Atmos. Sci.*, **50**, 3322-3335.

Shapiro, L. J., and H. E. Willoughby, 1982: The response of balanced hurricanes to local sources of heat and momentum. *J. Atmos. Sci.*, **39**, 378-394.

Smagorinsky, J. S., 1963: General circulation experiments with the primitive equations. I: The basic experiment. *Mon. Wea. Rev.*, **91**, 99-164.

Terwey, W. D. and M. T. Montgomery, 2003: Vortex waves and evolution in sharp vorticity gradient vortices. Colorado State University Bluebook #734. 97 pp.

Tripoli, G. J., and W. R. Cotton, 1981: The use of ice-liquid water potential temperature as a thermodynamic variable in deep atmospheric models. *Mon. Wea. Rev.*, **109**, 1094-1102.

Tripoli, G. J., and W. R. Cotton, 1982: The Colorado State University three-dimensional cloud/mesoscale model - 1982. Part I: General theoretical framework and sensitivity experiments. *J. Rech. Atmos.*, **16**, 185-220.

Tung, K. K., 1986: Nongeostrophic theory of zonally averaged circulation. Part I: Formulation. *J. Atmos. Sci.*, **43**, 2600-2618.

Vallis, G. K., and M. E. Maltrud, 1993: Generation of mean flows and jets on a beta plane and over topography. *J. Phys. Ocean.*, **23**, 1346-1362.

Walko, R. L., W. R. Cotton, J. L. Harrington, and M. P. Myers, 1995: New RAMS cloud microphysics parameterization. Part I: The single moment scheme. *Atmos. Res.*, **38**, 29-62.

Wilhelmson, R. B., and L. J. Wicker, 2001: Numerical modeling of severe local storms. *Severe Convective Storms, Meteor. Monogr.*, No. 50, Amer. Meteor. Soc., 123-166.

Williams, G. P., 1978: Planetary circulations: 1. Barotropic representation of Jovian and terrestial turbulence. *J. Atmos. Sci.*, **35**, 1399-1426.

Willoughby, H. E., 1979: Forced secondary circulations in hurricanes. *J. Geophys. Res.*, **84**, 3173-3183.

Willoughby, H. E., 1990: Temporal changes of the primary circulation in tropical cyclones. *J. Atmos. Sci.*, **47**, 242-264.

Willoughby, H. E., and P. G. Black, 1996: Hurricane Andrew in Florida: Dynamics of a disaster. *B. Amer. Met. Soc.*, **77**, 543-549.

Willoughby, H. E., J. A. Clos, and M. G. Shoreibah, 1982: Concentric eye walls, secondary wind maxima, and the evolution of the hurricane vortex. *J. Atmos. Sci.*, **39**, 395-411.

Willoughby, H. E., H.-L. Jin, S. J. Lord, and J. M. Piotrowicz, 1984: Hurricane structure and evolution as simulated by an axisymmetric, nonhydrostatic numerical model. *J. Atmos. Sci.*, **41**, 1169-1186.

Willoughby, H. E., D. P. Jorgensen, R. A. Black, and S. L. Rosenthal, 1985: Project STORMFURY: A scientific chronicle 1962-1983. *B. Amer. Met. Soc.*, **66**, 505-514.

Yano, J.-I., and K. A. Emanuel, 1991: An improved model of the equatorial troposphere and its coupling with the stratosphere. *J. Atmos. Sci.*, **48**, 377-389.

Zipser, E. J., 1977: Mesoscale and convective-scale downdrafts as distinct components of squall-line structure. *Mon. Wea. Rev.*, **105**, 1568-1589.

Appendix A

THE RAMS

For this work, we employ the Regional Atmospheric Modeling System (RAMS) (Pielke et al., 1992; Cotton et al., 2003). The RAMS is a three-dimensional, non-hydrostatic numerical modeling system with equations for the time-dependent changes of velocity, non-dimensional pressure perturbation, ice-liquid water potential temperature (Tripoli and Cotton, 1981), and cloud microphysics including seven moist particulate species. Diagnostic equations include those for potential temperature and vapor mixing ratio (Tripoli and Cotton, 1982).

The equations used in the RAMS are given later. The RAMS utilizes an Arakawa C-grid representation of the atmosphere, which staggers the thermodynamic variables within the center of a cube on whose facess reside the kinematic variables. This grid staggering requires a smaller timestep for stability, but allows for more accurate gravity wave propogation than other grids (Haltiner and Williams, 1980).

The microphysical scheme includes seven species: cloud droplets, rain, pristine ice, snow, aggregates, graupel, and hail. The microphysical scheme can be run in one or two-moment modes and was developed by Walko et al (1995). In our hurricane simulations, we exclusively utilize the simpler one-moment schemes with the exception of pristine ice (Appendix A, Montgomery et al. 2006). We have run two hurricane simulations (as well as sixteen thunderstorm simulations) for this work. The first hurricane simulation uses all seven microphysical species. The second only includes the cloud droplet and rain species. We call this latter sensitivity simulation the "no-ice" simulation while the

former is called the "control" simulation. All thunderstorm simulations use the full microphysical scheme.

The following parameterizations were used in the modeling studies in this work. Surface flux parameterizations for latent heat, sensible heat and momentum are based on the Louis (1979) scheme. The radiation scheme for both long wave and short wave radiation developed by Harrington (1997) is used, which includes cloud microphysical interactions. The sub-grid scale turbulence scheme used is based on Smagorinsky (1963) with modifications from Lilly (1962) and Hill (1974). These modifications enhance diffusion in unstable conditions while reducing diffusion in stable conditions.

Multiple nested grids are used in the hurricane simulations, developed from the work of Clark and Farley (1984). The grids are two-way interactive, allowing for increased spatial resolution in areas where one desires explicit representation of cloud scale features.

A list of symbols can be found in Table A.1. Subscript 0 denotes basic-state thermodynamic quantities. Primed quantities are deviations from the basic state.

The equations of motion are

$$\frac{\partial u}{\partial t} = -u\frac{\partial u}{\partial x} - v\frac{\partial u}{\partial y} - w\frac{\partial u}{\partial z} - \theta_0\frac{\partial \pi'}{\partial x} + fv + \frac{\partial}{\partial x}\left(K_m\frac{\partial u}{\partial x}\right) + \frac{\partial}{\partial y}\left(K_m\frac{\partial u}{\partial y}\right) + \frac{\partial}{\partial z}\left(K_m\frac{\partial u}{\partial z}\right), \tag{A.1}$$

$$\frac{\partial v}{\partial t} = -u\frac{\partial v}{\partial x} - v\frac{\partial v}{\partial y} - w\frac{\partial v}{\partial z} - \theta_0\frac{\partial \pi'}{\partial y} - fu + \frac{\partial}{\partial x}\left(K_m\frac{\partial v}{\partial x}\right) + \frac{\partial}{\partial y}\left(K_m\frac{\partial v}{\partial y}\right) + \frac{\partial}{\partial z}\left(K_m\frac{\partial v}{\partial z}\right), \tag{A.2}$$

and

$$\frac{\partial w}{\partial t} = -u\frac{\partial w}{\partial x} - v\frac{\partial w}{\partial y} - w\frac{\partial w}{\partial z} - \theta_0\frac{\partial \pi'}{\partial z} - \frac{g\theta_v'}{\theta_0} + \frac{\partial}{\partial x}\left(K_m\frac{\partial w}{\partial x}\right) + \frac{\partial}{\partial y}\left(K_m\frac{\partial w}{\partial y}\right) + \frac{\partial}{\partial z}\left(K_m\frac{\partial w}{\partial z}\right). \tag{A.3}$$

The thermodynamic equation is

$$\frac{\partial \theta_{il}}{\partial t} = -u\frac{\partial \theta_{il}}{\partial x} - v\frac{\partial \theta_{il}}{\partial y} - w\frac{\partial \theta_{il}}{\partial z} + \frac{\partial}{\partial x}\left(K_h\frac{\partial \theta_{il}}{\partial x}\right) + \frac{\partial}{\partial y}\left(K_h\frac{\partial \theta_{il}}{\partial y}\right) + \frac{\partial}{\partial z}\left(K_h\frac{\partial \theta_{il}}{\partial z}\right) + \left(\frac{\partial \theta_{il}}{\partial t}\right)_{rad}. \tag{A.4}$$

List of symbols used in the RAMS governing equations

c_p	Specific heat of dry air with constant pressure
f	Coriolis parameter
g	Acceleration due to gravity
K_h	Eddy viscosity coefficent for heat and moisture
K_m	Eddy viscosity coefficent for momentum
L_{lv}	Latent heat of the liquid to vapor phase transition
L_{iv}	Latent heat of the ice to vapor phase transition
p	Pressure
R	Gas constant
r_a	Mixing ratio for aggregates
r_c	Mixing ratio for cloud droplets
r_g	Mixing ratio for graupel
r_h	Mixing ratio for hail
r_p	Mixing ratio for pristine ice crystals
r_r	Mixing ratio for rain
r_s	Mixing ratio for snow
r_T	Mixing ratio for total water
T	Temperature
u	Zonal wind (x-direction)
v	Meridional wind (y-direction)
w	Vertical wind (z-direction)
π	Exner function
ρ	Density
θ	Potential temperature
θ_{il}	Ice-liquid potential temperature
θ_v	Virtual potential temperature

Table A.1: List of symbols used in the RAMS governing equations.

Water species are advected and diffused by

$$\frac{\partial r_n}{\partial t} = -u\frac{\partial r_n}{\partial x} - v\frac{\partial r_n}{\partial y} - w\frac{\partial r_n}{\partial z} + \frac{\partial}{\partial x}\left(K_h\frac{\partial r_n}{\partial x}\right) + \frac{\partial}{\partial y}\left(K_h\frac{\partial r_n}{\partial y}\right) + \frac{\partial}{\partial z}\left(K_h\frac{\partial r_n}{\partial z}\right) + \left(\frac{\partial r_n}{\partial t}\right)_{rad}, \tag{A.5}$$

where r_n stands for any of the seven basic microphysical species mixing ratios.

Mass continuity is governed by

$$\frac{\partial \pi'}{\partial t} = -\frac{R\pi_0}{c_v\rho_0\theta_0}\left(\frac{\partial \rho_0\theta_0 u}{\partial x} + \frac{\partial \rho_0\theta_0 v}{\partial y} + \frac{\partial \rho_0\theta_0 w}{\partial z}\right). \tag{A.6}$$

The Exner function π is defined

$$\pi = c_p\left(\frac{p}{p_r}\right)^{\frac{R}{c_p}}, \tag{A.7}$$

where p_r is a reference pressure (10^5 Pa).

Hydrostatics are given by

$$\frac{\partial \pi}{\partial z} = -\frac{g}{\theta_v} + g\left(r_T - r_v\right), \tag{A.8}$$

and

$$\frac{\partial \rho u}{\partial x} + \frac{\partial \rho v}{\partial y} + \frac{\partial \rho w}{\partial z} = 0. \tag{A.9}$$

Ice-liquid potential temperature is a temperature quantity that is conservative under vapor to liquid, vapor to ice, and liquid to ice phase changes and is defined by

$$\theta_{il} = \theta\left(1 - \frac{L_{lv}r_l}{c_pT} - \frac{L_{iv}r_i}{c_pT}\right). \tag{A.10}$$